An investigation of low energy quasiparticle excitations via thermal conductivity measurements

by

William Henry Toews

A thesis
presented to the University of Waterloo
in fulfillment of the
thesis requirement for the degree of
Master of Science
in
Physics

Waterloo, Ontario, Canada, 2012

© William Henry Toews 2012

I hereby declare that I am the sole author of this thesis. This is a true copy of the thesis, including any required final revisions, as accepted by my examiners.

I understand that my thesis may be made electronically available to the public.

Abstract

Thermal conductivity measurements are made on a variety of systems in order to probe low energy quasiparticle excitations. In particular, thermal conductivity measurements were made on the iron based superconducting material LaFePO at temperatures from 60 mK to 1 K and in fields from 0 T to 5 T in order to shed light on the symmetry of the superconducting order parameter. A substantial non-zero electronic contribution to the thermal conductivity is observed and interpreted as sub-gap electronic quasiparticles which is clear evidence for a nodal gap symmetry. A high scattering rate and non-T^3 temperature dependence of the conductivity is evidence against the d-wave scenario. However, the field dependence does seem to suggest that the anisotropic $s\pm$ picture is a likely candidate for the order parameter, although more theoretical work is required to confirm this.

Thermal conductivity measurements were also made on the spin-ice system $Ho_2Ti_2O_7$ between 50 mK and 1.4 K in applied magnetic fields from 0 T to 8 T in an attempt to observe the much debated magnetic monopole-like quasiparticles. An applied magnetic field of 8 T was applied along to [111] direction as to fully polarize the magnetic moments in order to extract the phonon contribution of the thermal conductivity. The low field thermal conductivity reveals evidence for an additional heat transfer mechanism that also scatters phonons which is magnetic in nature. This is taken to be evidence for the existence of monopole-like excitations out of the spin-ice ground state and is described by existing Debye-Hückel theory.

Thermal transport was used in conjunction with charge conductivity to study the unconventional quantum critical point (QCP) in the heavy-Fermion superconductor β-$YbAlB_4$ at temperatures down to 60 mK and in fields up to 2 T. The results show that the Wiedemann-Franz law (WFL) is obeyed down to the lowest measured temperatures indicating that the Landau quasiparticles remain intact near the QCP. A small suppression of the Wiedemann-Franz ratio ($L/L_0 = \kappa/\sigma T L_0$) is seen at finite temperatures ($T < 1$ K) with minimal dependence on magnetic field. Comparing with other similar quantum critical systems, it becomes apparent that inelastic scattering events have little effect on the transport and are mainly field independent in β-$YbAlB_4$.

An overview of the design for a new thermal conductivity mount is also presented. The design hinges around the idea of building the experiment mount into a small copper box rather than on an open frame. Not only does this provide mechanical stability for safe transportation, it also reduces the noise caused by electromagnetic interference (EMI) in the sample thermometers by more than a factor of ten over the old wire frame design.

Contributions

The LaFePO sample was grown in Ian Fisher's lab at Stanford University. Many of the thermal conductivity measurements of LaFePO were conducted by Mike Sutherland and John Dunn. Mike also prepared the contacts on the sample and affixed gold wires to them. I measured the electrical resistivity of the sample in applied magnetic fields. I also performed all of the data analysis presented here and in our publication [1].

The $Ho_2Ti_2O_7$ sample was grown in Bruce Gaulin's lab at McMaster University. I then prepared the sample to the correct size and affixed the silver wire contacts used to measure the thermal conductivity. I conducted all of the thermal transport measurements of this sample and performed the data analysis which are presented here.

The β-$YbAlB_4$ samples were prepared by Eoin O'Farrell. Eoin also measured the thermal conductivity of one of the samples presented here. I measured the thermal transport of the other sample as well as the electrical resistivity of both samples in a variety of magnetic fields. I also executed the data analysis seen in the appendix.

Acknowledgements

First and foremost, I must thank my supervisor, Rob Hill. His guidance and patience have provided the perfect environment for me to grow as a student and an experimentalist. Whether it is answering late night phone calls when the fridge is misbehaving or the in depth discussions on the latest results or even just chatting about football scores, Rob has instilled the confidence and knowledge imperative in the completion of this graduate work. Working with Rob has been a real joy and I am truly grateful for the opportunity.

Next I would like to thank my advisory committee members, Dr. David Hawthorn and Dr. Elisabeth Nicol. Their input and suggestions really helped focus my research and keep me on track. I would also like to thank Adrian Lupascu for serving on my defence committee. Although not on my committee, Jan Kycia has always been available as a seemingly limitless supply of experimental knowledge and he has certainly been a valuable part of my education. The members of the Kycia group were persistent in keeping a constant supply of liquid helium available at our beck and call - essential for cryogenics.

I also need to thank my collaborators and crystal growers, Mike Sutherland from the University of Cambridge and Eoin O'Farrell from the University of Tokyo, who both worked on the LaFePO and β-$YbAlB_4$ projects. In particular, Mike conducted most of the thermal conductivity measurements on LaFePO and Eoin measured the thermal conductivity in one on the β-$YbAlB_4$ samples. James Analytis and Ian Fisher from Stanford University grew the LaFePO crystal. Kate Ross, Hannah Dabkowska and Bruce Gaulin from McMaster University grew the $Ho_2Ti_2O_7$ crystals.

Hiruy Haile, Andrew Dube and Harmen Vander Heide of the STS shop deserve recognition for teaching me how to machine various items needed for my experiments as well as constructing the main components of the redesigned thermal conductivity mount.

I would be daft if I said I could have done all this without the help and support from my friends, lab mates and colleagues as they have been a source of motivation, encouragement and laughter. The list of of notable accomplices includes John Dunn, Luke Yaraskavitch, David Pomaranski and Halle Revell, Kier Vonkonigslow and Steffanie Freeman, however this is by no means exhaustive. John Dunn also aided in many of the thermal conductivity measurements of LaFePO. My lab partner, Kevin Liu, deserves my gratitude for all the help with running the fridge, the late nights in the lab, and for the much needed comradery and noodle soups.

Finally, I would like to thank my family. My parents and sisters have supported me throughout my entire educational career. Most of all, I need to thank my wife, Jennifer, for putting up with me through this whole process. I could not have done it alone.

Dedication

To my wife, Jennifer. ♡

Table of Contents

List of Tables

List of Figures

Chapter 1

Introduction

As temperature approaches absolute zero, a variety of exotic states of matter can arise. Such emergent states include superconductivity, which has zero electrical resistance, degenerate spin-ice states with a residual zero-point entropy, and quantum critical systems that undergo phase changes at $T = 0$ K. To fully understand the essence of these phases it is essential to measure the excitations out of the ground state. Thermal conductivity has been proven to be an invaluable tool for measuring delocalized quasiparticle excitations. Pairing thermal and charge transport measurements can reveal the nature of these excitations via the Wiedemann-Franz law (WFL) which is satisfied in the electronic Landau quasiparticle framework.

Superconductivity is supported in a wide variety of materials which can be divided up into two main classes, conventional and unconventional superconductors. Conventional superconductors have a phonon mediated electron pairing mechanism which is fairly well understood and described by Eliashberg theory (an extension of Bardeen-Cooper-Schrieffer (BCS) theory). However, their maximum attainable critical temperature (T_c) is predicted (and measured) to be a measly 23 K [2] where thermal fluctuations will be large enough to break Cooper pairs. Unconventional superconductors, on the other hand, do not follow BCS theory and can have critical temperatures above 90 K, with optimally doped $YBa_2Cu_3O_{7-\delta}$ (a member of the high-T_c cuprate family) as an example with $T_c \sim 91$ K under ambient pressure [3]. The pairing mechanism in the cuprates is generally accepted to be magnetic in nature although not fully understood. Most recently, however, a new family of iron based superconductors have emerged which also appear to have a magnetic pairing mechanism due to a weak electron-phonon interaction [4]. The symmetry of the order parameter remains unknown. Thermal transport measurements of superconducting materials at temperatures approaching absolute zero uncovers valuable information about

the form of the order parameter. Hence, thermal conductivity measurements have been made on the iron-based superconductor LaFePO.

The rare-earth titanates, $Ho_2Ti_2O_7$ and $Dy_2Ti_2O_7$, provide an excellent reference for studying frustrated magnetism in three dimensions. The rare-earth ions (Ho^{3+}, Dy^{3+}) are located on a pyrochlore structure (corner sharing tetrahedra) of cubic symmetry. Their magnetic moments are nearly perfect Ising spins quantized along the local [111] direction (into or out-of each tetrahedra) with a net nearest neighbour ferromagnetic exchange interaction. A 6-fold degenerate ground state emerges such that two spins point into each tetrahedra and two spins point out of each tetrahedra. This arrangement is analogous to the locations of hydrogen ions with respect to the oxygen atoms in water ice, therefore the "spin-ice" nomenclature is used. Excitations out of this ground state have been proposed to behave like magnetic monopole like quasiparticles, with a coulomb interaction. This arises from a single ice-rule breaking spin flip, which creates a monopole anti-monopole pair. Subsequent spin flips do not further break the ice rules, and thus the monopoles are free to move about the crystal. The existence of these monopoles remains a topic of debate. Therefore, thermal conductivity measurements were made on $Ho_2Ti_2O_7$ in an attempt to directly, or indirectly observe the delocalized monopole excitations.

A quantum critical point (QCP) ensues when a phase transition occurs at $T = 0$ K. These transitions are driven by quantum fluctuations rather than thermal fluctuations as in conventional phase transitions away from absolute zero. These curious states of matter may not follow Fermi-liquid behavior as in a normal metal. There is a debate as to whether multiple types of QCPs exist which are distinguishable by their macroscopic properties. Heavy-fermion metals provide an appropriate system for studying antiferromagnetic quantum criticallity. Consequently, thermal and electrical transport measurements were made on the heavy-fermion metal, $\beta YbAlB_4$ at temperatures approaching absolute zero. The results are compared to a collection of other similar quantum critical systems.

1.1 Outline

The goal of this thesis is to utilize the versatility of thermal conductivity measurements as a tool for measuring fundamental properties of materials by applying it to a variety of systems. This thesis is organized into three parts:

Part I - Theoretical Review

Part I focuses on the theoretical concepts used throughout this thesis. The theory behind thermal conductivity in both metals and insulating materials is discussed. Superconductivity is introduced, including an overview of convention s-wave and unconventional d-wave superconductors. The effect of an applied magnetic field is also considered. Frustrated magnetic systems are examined beginning with a 2 dimensional toy model followed by a real world 3 dimensional analogue. It is shown how excitations out of the spin ice ground state can be thought of as magnetic monopoles.

Part II - Experimental Details

Part II discusses how the measurement is made in practice. The concepts behind how a helium-3/helium-4 dilution fridge works and the many components involved are introduced. A new compact and RF shielded thermal conductivity mount is also presented showing the improvements over the old, wire-framed mount.

Part III - Experimental Results

Part III is where the results of my labor are presented. A detailed examination of the thermal and electrical conductivity of the iron based superconductor, LaFePO, is presented. Thermal conductivity measurements on the spin ice material $Ho_2Ti_2O_7$ are presented in the search for magnetic monopoles.

Thermal conductivity measurements of $\beta YbAlB_4$ are located in the appendix. Technical drawings for the thermal conductivity box and the printed circuit board can also be found in the appendices. A labeled diagram of the LabView program used to acquire the data is also included in this section.

Part I

Theoretical Review

Chapter 2

Thermal Conductivity Theory

The propagation of heat through a material is characterized by the thermal conductivity κ which is defined as the ratio of the heat flux density $\vec{Q}$ to the local temperature gradient $\vec{\nabla}T$ via Fourier's Law of Heat Conduction [5]:

$$\vec{Q} = -\kappa\vec{\nabla}T \tag{2.1}$$

Thermal conductivity is in general a two dimensional tensor due to directional anisotropies in materials. However, in crystalline materials with a uniform heat current in one dimension, the thermal conductivity can be represented as a scalar. Under these circumstances, we can re-write Fourier's Law as

$$\dot{Q} = -\kappa\frac{dT}{dx} = -\kappa\Delta T\frac{A}{l} \tag{2.2}$$

where $\dot{Q}$ is the amount of heat transferred per unit time, A is the cross-sectional area of the sample and l is the length.

The heat transfer is mediated by electronic excitations, lattice vibrations, magnetic excitations etc. so that the total thermal conductivity is the sum of these components acting in parallel:

$$\kappa_{Total} = \kappa_e + \kappa_{ph} + \kappa_{mag} + ... \tag{2.3}$$

Thermal transport is a valuable tool in measuring delocalized, low energy, quasi-particle excitations that are capable of carrying entropy. It can also be used in conjunction with the electrical conductivity in determining the state of a system, for example, determining whether a Fermi liquid state is established by verifying the Wiedemann-Franz law (WFL).

In order to take advantage of the experimental power transport measurements can provide, an understanding of some of the more basic concepts of electronic charge and thermal transport and phonon thermal transport is essential. They will now be discussed under the framework set up by Drude, Sommerfeld and Debye.

2.1 Electronic Conduction in Metals

In 1900, Paul Drude proposed a model describing electrical and thermal conduction by applying the kinetic theory of gases to a gas of electrons. In order to do this, several assumptions had to be made about this cloud of electrons that, barring large electron-electron or electron-ion interactions, results in a satisfactory description of normal metals. These assumptions are as follows: in the absence of an external electromagnetic field, the conduction electrons travel in straight lines between collisions. This neglect of the electron-electron and electron-ion interactions between collisions are known as the *independent electron approximation* and the *free electron approximation* respectively [5]. Furthermore, only collisions between electrons and ions will be considered and they will be treated as instantaneous events as in the kinetic theory of gases. These collisions will occur with a probability per unit time of $1/\tau$ where τ is the relaxation time. Finally, Dude assumed that the system will attain thermal equilibrium only through these collisions. These assumptions can now be used to calculate the electrical resistivity.

We will define the electrical conductivity σ as the ratio of the electronic current density $\vec{j}$ to the electric field $\vec{E}$ at any given point in the metal such that

$$\vec{j} = \sigma \vec{E} \tag{2.4}$$

Similar to the thermal conductivity, the electrical conductivity is also in general a second order tensor, but when the electric field is simplified to one-dimension σ reduces to a scalar quantity. The electrical resistivity ρ is then defined as reciprocal of the conductivity so that $\rho = 1/\sigma$. Suppose a current $\vec{I}$ is flowing through a wire of length L and cross-sectional area A. This current can be described as n electrons with charge $-e$ flowing through the area A with velocity $\vec{v}$ parallel to $\vec{I}$ over a short time dt and can be written as $\vec{I} = -ne\vec{v}Adt$. Therefore, the resulting current density is given by

$$\vec{j} = -ne\vec{v} \tag{2.5}$$

In the absence of an electric field the net current density and consequently the average electron velocity equates to zero. This is due to the fact that the velocity of an electron

immediately after a collision is completely random and thus averages to zero. So a non-zero mean velocity is a direct result of an applied electric field. Hence, the mean velocity of the electrons can be thought of as the effect of the electric field on a stationary electron over a time t and is thus equal to $-e\vec{E}t/m$. However, the average time between collisions is equal to the relaxation time τ. The average electron velocity can thus be written as

$$\vec{v}_{avg} = -\frac{e\vec{E}\tau}{m} \tag{2.6}$$

Combining equations (2.4), (2.5) and (2.6) we arrive at the electrical conductivity as per the Drude model.

$$\vec{j} = \left(\frac{ne^2\tau}{m}\right)\vec{E}; \quad \sigma = \frac{ne^2\tau}{m} \tag{2.7}$$

We are able to use the Drude model to find this explicit form of the electrical conductivity because it does not depend on the energy distribution. Therefore, even though the Drude model is strictly classical and would thus use the Maxwell-Boltzmann distribution the conductivity is still valid. We can modify the Drude model by using Fermi-Dirac statistics as in the Sommerfeld Theory of metals to derive the specific heat and thermal conductivity of semi-classical metals.

To determine the electronic thermal conductivity κ_e we will calculate the electronic contribution to the specific heat from Fermi-Dirac statistics and take advantage of the following equation from kinetic theory which states:

$$\kappa_e = \frac{1}{3}c_v v_F^2 \tau \tag{2.8}$$

where c_v is the electronic specific heat, v_F is the Fermi velocity and τ is the electron mean free path. Since we are using Fermi-Dirac statistics, we will use the Fermi function to describe the electronic distribution which is defined as

$$f(\epsilon) = \frac{1}{e^{(\epsilon-\mu)/k_B T} + 1} \tag{2.9}$$

The Fermi function, $f(\epsilon)$, and the density of states, $g(\epsilon)$, can then be used to calculate the

electronic specific heat by finding the total internal energy and recalling that $c_v = \left(\frac{\partial u}{\partial T}\right)_n$.

$$\begin{aligned} c_v &= \frac{\partial}{\partial T} \int_{-\infty}^{\infty} d\epsilon \; g(\epsilon)\epsilon f(\epsilon) \\ &= \frac{3}{2}\left(\frac{k_B T}{\epsilon_F}\right) n k_B \int_{-\epsilon_F/k_B T}^{\infty} \frac{x^2 e^x}{(e^x+1)^2} dx \\ &= \frac{\pi^2}{2}\left(\frac{k_B T}{\epsilon_F}\right) n k_B \qquad (\text{as } T \to 0) \end{aligned} \tag{2.10}$$

Here, $x \equiv (\epsilon - \epsilon_F)/k_B T$, and as $x \to \epsilon_F/k_B T$, $e^x \approx 0$ thus the lower limit on the integral can be replaced by $-\infty$ so that the integral can be easily evaluated to be $\pi^2/3$. Noting that the Fermi velocity $v_F = \left(\frac{\hbar}{m}\right) k_F$ and the Fermi energy $\epsilon_F = \frac{\hbar^2 k_F^2}{2m}$, we can now combine equations (2.8) and (2.10) to determine the electronic contribution to the thermal conductivity κ_e.

$$\kappa_e = \frac{\pi^2}{3} \frac{k_B^2 n \tau}{m} T \tag{2.11}$$

2.1.1 Wiedemann-Franz Law

The ratio of the thermal conductivity (equation 2.11) and the electrical conductivity (equation 2.7) thus give a constant value regardless of the material [6].

$$\frac{\kappa_e}{\sigma T} = \frac{\pi^2}{3}\left(\frac{k_B}{e}\right)^2 = 2.44 \cdot 10^{-8} \; W\Omega/K^2 \tag{2.12}$$

This can be verified by measuring a well behaved metal to low enough temperatures where the thermal conductivity is dominated by the electronic term and scattering is independent of temperature. Thermal and electrical conductivity was measured in a silver wire to demonstrate the Wiedemann-Franz law. The results are seen in figure 2.1.

2.2 Phonon Thermal Conduction

We shall calculate the phonon thermal conductivity in a similar manner to the electronic thermal conductivity. However, since phonons are bosons, Bose-Einstein statistics will be

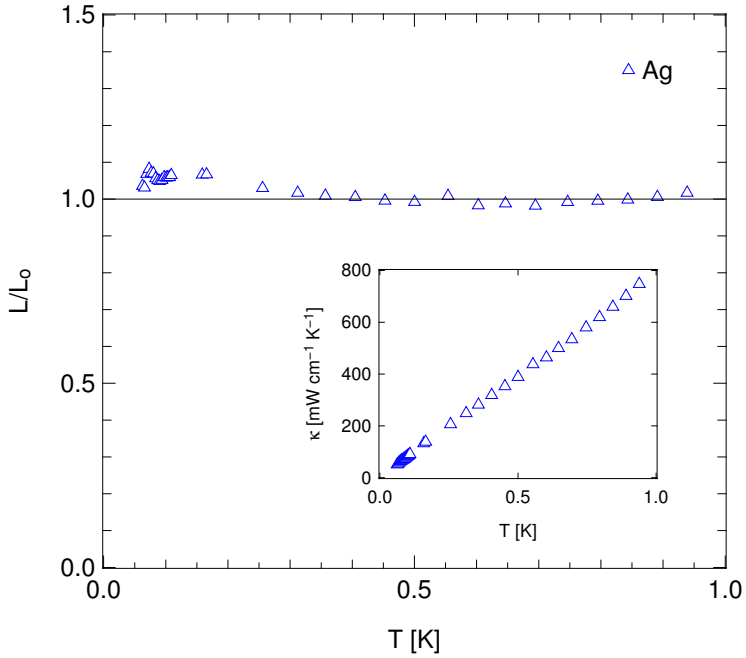

Figure 2.1: A plot of L/L_0 vs T for a silver wire where $L = \kappa/\sigma T$. It is evident that the Wiedemann-Franz law in satisfied to within 8% from 50 mK to 1 K. The slight deviation at low temperature is due to poor thermometry. *Inset:* A plot of κ vs T of the silver wire demonstrating that the conductivity is linear in temperature as expected for the electronic contribution to thermal conductivity.

used in place of Fermi-Dirac statistics. Thus the distribution function of interest is:

$$f(\epsilon) = \frac{1}{e^{(\epsilon-\mu)/k_B T} - 1} \tag{2.13}$$

We shall follow the Debye model of lattice vibrations (phonons) at low temperatures, ie. when $\Theta_D/T \gg 1$ where Θ_D is the Debye temperature. The main assumption made in the Debye model is that there is an upper limit to the linear phonon dispersion $\omega = v_s k$. That is, no modes are allowed above the Debye wave vector, k_D. Now, using the Bose-Einstein function and the phonon dispersion, we are able to calculate the phonon energy:

$$u = 9Nk_B T \left(\frac{T}{\Theta_D}\right)^3 \int_0^{x_D} \frac{x^3}{e^x - 1} dx \tag{2.14}$$

where $x \equiv \hbar\omega/k_B T$, $x_D \equiv \Theta_D/T$ and N is the number of atoms in the the crystal. Since we are concerned with the low temperature regime, then $x_D \to \infty$ and the integral can be evaluated to be $\pi^4/15$. The phonon specific heat can now be easily obtained by taking the derivative with respect to temperature so that

$$c_{ph} = \frac{12}{5}\pi^4 N k_B \left(\frac{T}{\Theta_D}\right)^3 \tag{2.15}$$

This is the famous T^3 law for the low temperature phonon specific heat. Once again, using kinetic theory we can find the phonon thermal conductivity.

$$\kappa_{ph} = \frac{1}{3} c_{ph} v_s l \propto T^3 \tag{2.16}$$

This is a specific case of the phonon thermal conductivity where the phonon mean free path, l, is temperature independent, for example in the boundary scattering limit. However, if we write the specific heat in a more general way by taking the derivative of equation (2.14) without evaluating the integral we are get

$$c(x)dx = \frac{3k_B}{2\pi^2 v^3}\left(\frac{k_B}{\hbar}\right)^3 T^3 \frac{x^4 e^x}{(e^x-1)^2} dx \tag{2.17}$$

and thus the thermal conductivity is

$$\kappa = \frac{1}{3} v \int l(x) c(x) dx \tag{2.18}$$

which allows the mean free path, $l(x)$, to have a frequency dependence.

2.2.1 Phonon Scattering Mechanisms

Now that we have a general form of the phonon thermal conductivity allowing the mean free path to have a frequency dependence, we can examine a variety of phonon scattering mechanisms which lead to a range of temperature dependencies in the thermal conductivity.

1. *Boundaries.* As the temperature approaches absolute zero, the mean free path of the phonons becomes large, and is eventually limited by the sample boundaries. Thus the mean free path is frequency independent and is equal to a geometric average of the sample width determined by $l = \sqrt{4A/\pi}$ where A is the cross-sectional area of

the sample. In light of this, equation (2.8) dictates that the thermal conductivity due to sample boundary scattering will be given by

$$\kappa_b = \frac{1}{3}\gamma v_s \sqrt{\frac{4A}{\pi}} T^3 \tag{2.19}$$

where the phonon specific heat is $c_{ph} = \gamma T^3$. A T^3 behaviour is seen in the conductivity for other frequency independent mean free path scattering modes, for example, scattering off of grain boundaries.

The validity of the assumption that scattering off the sample boundaries affects all phonons regardless of their frequency is in question when one considers the difference between diffuse and specular scattering. In fact, due to specular scattering of phonons off of the sample boundaries, the temperature dependence of the thermal conductivity is sub T^3. This phenomena has been examined in depth in other insulating materials [7, 8, 9].

2. *Phonons: normal and Umklapp-processes.* Consider the interaction of two phonons with wave vectors $\vec{q}_1$ and $\vec{q}_2$ and frequencies ω_1 and ω_2 respectively such that they combine to result in a third phonon with wave vector $\vec{q}_3$ and frequency ω_3. Note that in these kind of three-phonon processes, energy must be conserved ($\hbar\omega_1 + \hbar\omega_2 = \hbar\omega_3$) and wave vector must also be conserved ($\vec{q}_1 + \vec{q}_2 = \vec{q}_3 + \vec{q}_o$) where $\vec{q}_o$ is a reciprocal lattice vector. Now, if $\vec{q}_o = \vec{0}$ then $\vec{q}_3$ lies in the first Brillouin zone and the phonon momentum is conserved. This is known as a normal process (or N-process) and does hinder the heat transport. If $\vec{q}_3$ falls outside of the first Brillouin zone then $\vec{q}_o \neq \vec{0}$ and thus changing the net direction of energy flow. This is known as Umklapp scattering (or U-processes) and does give rise to thermal resistance. For a U-process to occur, at least one of the phonons must have a frequency greater than half of the maximum allowed frequency, ie. $\omega_1 \geq \frac{1}{2}\omega_D = \frac{1}{2}k_B\Theta_D/\hbar$ which occurs with a probability of approximately $e^{-\Theta_D/2T}$ at low temperatures ($T \ll \Theta_D$). Similarly, the probability that the second phonon has a large enough wave vector to make $\vec{q}_3$ fall outside of the first Brillouin zone is usually assumed to proportional T^{-n}. Thus the thermal conductivity will have the following temperature dependence:

$$\kappa_u \propto T^n e^{\Theta_D/gT} \tag{2.20}$$

where $n \approx 3$ and $g \approx 2$. We also find that the mean free path is proportional to the frequency ω.

3. *Conduction electrons.* When phonons interact with conduction electrons in metals at low temperatures, the electrons will absorb or emit energy on the order of $k_B T$ as a

result of small angle scattering. This is enough energy to promote/demote an electron just above/below the Fermi-surface. That is, only electrons that lie within $k_B T$ of the Fermi surface will be able to interact with the phonons. Hence, the number of electrons available fore scattering at a given temperature will be proportional to T and therefore the phonon mean free path, l, will be proportional to T^{-1}. We have also seen that the phonon specific heat c_{ph} is proportional to T^3 (see equation (2.15)) thus using kinetic theory (equation (2.8)) we find that the conductivity is given by:

$$k_{e-ph} \propto T^2 \tag{2.21}$$

and the mean free path is proportional to ω.

4. *Point defects and isotopes.* Defect in crystals that are on the atomic scale such as isotopes with different masses, impurities or a vacant lattice site will all appear as point defects in the crystal to the long wavelength phonons at low temperature. These defects will scatter phonons similar to Rayleigh scattering of photons such that they have a scattering probability proportional to q^4. The difference is that the phonon mean free path is ultimately limited by the sample dimensions. The scattering rate is thus proportional to T^4 which results in the thermal conductivity being proportional to T^{-1} since the phonon specific heat goes as T^3. We also find that the mean free path is proportional to ω^{-4}.

5. *Dislocations.* A dislocation is a defect in a crystal that extends in one direction. For example, when an atom does not lie directly on a lattice site, but is skewed from that location. This leads to two main imperfections, the first is that the atom is not quite at the lattice site, and the second is that it causes a strain field in the surrounding crystal. The latter has a larger impact on the phonon scattering as the former is on a much smaller length scale, on the order of a few atoms. This is analogous to Rayleigh scattering off of a cylinder. The thermal conductivity can therefore be found to be proportional to T^2 and the mean free path is proportional to ω^{-1}.

It is worth noting that Umklapp processes only have a noticeable contribution on the phonon scattering at higher temperatures ($T \approx \Theta_D$) as the scattering rate decays exponentially. This being said, as the temperature is decreased, the phonon mean free path increases until comparable with the sample dimensions and therefore boundary scattering dominates as $T \to 0$ K. A brief reference table summarizing the various phonon scattering mechanisms along with the frequency dependence of the mean free path and the conductivity temperature dependence is given in table 2.1. A more detailed discussion of phonon scattering mechanisms in both metals and non-metals, see "Low Temperature Solid State Physics" by H. M. Rosenberg [10].

Scattering Mechanism	$l(\omega) \propto$	$\kappa(T) \propto$
Sample boundaries	const.	T^3
Grain boundaries	const.	T^3
Umklapp processes	ω	$T^3 e^{\Theta_D/2T}$
Conduction electrons	ω	T^2
Point defects	ω^{-4}	T^{-1}
Dislocations	ω^{-1}	T^2

Table 2.1: Frequency dependence of the phonon mean free path and temperature dependence of the thermal conductivity for various phonon scattering mechanisms.

2.2.2 Matthiessen's Rule

It is often advantageous to use the language of thermal resistance, $W \equiv 1/\kappa$, rather than thermal conductivity when considering scattering from multiple sources. The thermal resistances resulting from the various phonon scattering mechanisms can then be added analogous to electrical resistors in series. Thus, $W_{Total} = W_b + W_u + W_{pd} + \ldots$. Writing this in terms of thermal conductivity, using equation (2.8) we get Matthiessen's rule:

$$\frac{1}{\kappa_{Total}} = \sum_i \frac{1}{\kappa_i} = \frac{3}{c_{ph} v_s} \sum_i \frac{1}{l_i} \tag{2.22}$$

where l_i are the phonon mean free paths associated with boundary scattering, Umklapp processes etc. as discussed in section 2.2.1.

Chapter 3

Superconductivity

A superconductor is a material that when cooled below some critical temperature, T_c, undergoes a transition to a state which has zero resistivity and expels all magnetic fields (the Meissner effect). There are many classes of superconducting materials, both conventional and unconventional. One way to classify them is into two types, type I and type II. A type I superconductor is a perfect diamagnet with a linear magnetization up to some critical field, H_c and then reverts back to the normal, non-superconducting state. A type II superconductor is a perfect diamagnet up to a lower critical field, H_{c1} at which point the magnetization decays as the superconductor allows flux vortices to form inside the superconductor until superconductivity is killed at the upper critical field, H_{c2}.

The realization of room temperature superconductivity is the ultimate goal, it's essentially the holy grail. The discovery of a room temperature superconductor would have implications with transportation (levitating superconducting trains), power storage and transmission (zero resistance wires) and technology (smaller and more efficient electronics). Upon attempting to increase the critical temperature, it is essential to understand the origin of superconductivity in current materials through a collaboration of experimental and theoretical studies. When looking to the future of superconductivity it is also important to know the history, thus a quick summary of some of the major discoveries in superconductivity are discussed in the next section.

3.1 A Brief History of Superconductivity

The ability to measure materials at temperatures approaching absolute zero is of utmost importance in fully understanding the behavior of electrons and other novel phenomena

which would otherwise be clouded due to higher temperature lattice vibrations and other thermal fluctuations. When Kamerlingh Onnes discovered how to liquefy helium at 4.2 K in 1908 [11], a whole new realm of physics became accessible. Upon measuring the electrical resistivities of a variety of elements at these temperatures in 1911, he discovered that there was a sudden drop to zero resistance in mercury at 4.19 K which won him the Nobel prize two years later [12]. This behavior is now known as superconductivity. Over the next 75 years, superconductivity was found to exist in many other elements (lead [13], niobium [14]) and in the so called A15 compounds (V_3Si, Nb_3Sn) [15] with the maximum transition temperature (T_c) occurring in Nb_3Ge at 23.2 K [2]. This was the highest known transition temperature until 1986, at which point Bednorz and Müller found superconductivity in a copper based material, $La_{2-x}Ba_xCuO_4$, with $T_c = 36$ K [16]. This won them the Nobel prize in 1987, the same year that Paul Chu found $YBa_2Cu_3O_{7-\delta}$ to have a transition temperature of 93 K (well above liquid nitrogen temperatures) [3]. The cuprates remain the highest T_c materials to date, however in 2008 a new class of iron based superconducting materials were discovered [17]. This discovery sparked a flurry of interest due to its unconventional nature being that it is metallic in the normal state and also that it is magnetic, a property originally thought to suppress superconductivity. Before we dive into these unconventional superconductors, we will first look at the best theoretical model describing some of the more conventional superconductors.

3.2 Introduction to BCS Theory

The phenomena of superconductivity has stumped theoretical physicists since its discovery in the early 1900's. It wasn't until the 1950's when Bardeen, Cooper and Schrieffer formalized the first microscopic theory describing superconductivity (BCS theory) [18]. Cooper proposed that a weak attractive interaction between electrons would result in pairs of electrons forming bound states called Cooper pairs. These overlapping Cooper pairs then condense into the superconducting ground state which is at a lower energy than the normal state Fermi sea. Thus, below some critical temperature, T_c, all the electrons form Cooper pairs and bind together into a many body condensate ground state. The attractive potential between electrons can be mediated via a phonon interaction as in the case of conventional superconductors or a magnetic fluctuation interaction as in some of the unconventional superconductors. The idea of an attractive potential between electrons may seem hard to comprehend from an intuitive stand point, however due to the retarded phonon-electron (or magnon-electron) interaction the correlation length is in fact on the order of 1000 $\mathring{A}$, and thus does not violate the repulsive Coulomb interaction as one might

expect. A brief overview of BCS theory will now be discussed.

BCS theory is based on the idea that a weak attractive interaction between electrons will cause the formation of bound pairs of electrons known as Cooper pairs. Cooper pairs are comprised of a pair of electrons of opposite spin and momentum ($\mathbf{k}\uparrow$, $-\mathbf{k}\downarrow$) and form a spin singlet state which is verified by NMR Knight shift measurements [19, 20]. Since the paired electrons have opposite momentum, their net momentum is zero. The superconducting ground state wave function is described by:

$$|\Psi\rangle = \prod_{\mathbf{k}} (u_{\mathbf{k}} + v_{\mathbf{k}} c^{\dagger}_{\mathbf{k}\uparrow} c^{\dagger}_{-\mathbf{k}\downarrow})|0\rangle \tag{3.1}$$

where $|v_{\mathbf{k}}|^2$ is the probability of the state ($\mathbf{k}\uparrow$, $-\mathbf{k}\downarrow$) being occupied and $|u_{\mathbf{k}}|^2$ is the probability unoccupation such that $|u_{\mathbf{k}}|^2 + |v_{\mathbf{k}}|^2 = 1$. The energy gap from the normal state to the superconducting state is expressed via the superconducting gap equation.

$$\Delta_{\mathbf{k}} = \frac{1}{\Omega} \sum_{\mathbf{k}'} V_{\mathbf{k}\mathbf{k}'} u_{\mathbf{k}'} v_{\mathbf{k}'} = \frac{1}{\Omega} \sum_{\mathbf{k}'} V_{\mathbf{k}\mathbf{k}'} \frac{\Delta_{\mathbf{k}'}}{2\sqrt{\tilde{\epsilon}^2_{\mathbf{k}'} + \Delta^2_{\mathbf{k}'}}} \tag{3.2}$$

Here Ω is the volume, $V_{\mathbf{k}\mathbf{k}'}$ is the attractive interaction between electrons in states $\mathbf{k}$ and $\mathbf{k}'$ and $\tilde{\epsilon}_{\mathbf{k}'}$ is the kinetic energy above the Fermi energy (ie. $\tilde{\epsilon}_{\mathbf{k}'} = \epsilon_{\mathbf{k}'} - \epsilon_F$).

3.2.1 Symmetry of the superconducting gap

The superconducting gap function, $\Delta_{\mathbf{k}}$, can take on many forms with a variety of symmetries (see figure 3.1). In general, the s-wave symmetry has an isotropic gap, that is, $\Delta_{\mathbf{k}}$ is a constant function of the momentum, $\mathbf{k}$, so it does not change sign or magnitude, thus exhibiting a four-fold rotational symmetry. However, anisotropic s-wave symmetries can exist either with deep minima or even accidental nodes, in which case the value of the gap can change sign. This is allowed as long as $\Delta_{\mathbf{k}}$ maintains the four-fold rotational symmetry. Another possible symmetry is the d-wave scenario. The sign of the order parameter changes four times around the Fermi surface in the d-wave case which imposes mandatory nodes. The four-fold rotational symmetry is violated in this case, differentiating itself from the nodal s-wave scenario.

Discerning between the various gap symmetries can often be a formidable task, especially in some of the more exotic multiband materials materials such as the iron-based superconductors which will be discussed later in this chapter (see section 3.6). A variety of experiments can be used to probe the structure of the gap by measuring either the phase,

or the amplitude of the gap. The phase can be determined using the Josephson effect (ie. using a corner junction to detect a change in phase in the d-wave case). The amplitude can be measured via NMR, ARPES, penetration depth and thermal conductivity measurements (as reported in this thesis). Thermal conductivity is also adept at detecting the presence of nodes in the gap.

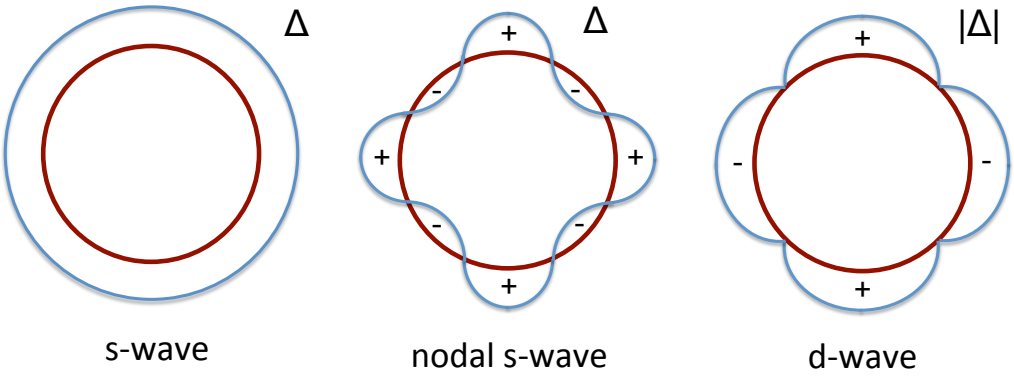

Figure 3.1: Possible order parameters projected onto the $(\mathbf{k}_x, \mathbf{k}_y)$ plane. The superconducting gap (blue line) is superimposed on top of a circular Fermi surface (red line). The s-wave scenario has a finite, isotropic gap which does not change sign (left). However, the gap can become anisotropic with the appearance of deep minima or even accidental nodes while maintaining the four-fold rotation symmetry (center). The sign changes sign four times around the Fermi-surface in the d-wave case, which imposes mandatory nodes in the gap (right). This breaks the four-fold rotational symmetry of the lattice.

3.3 Conventional Superconductors

For a conventional s-wave superconductor BCS theory assumes that the interaction is constant in a narrow band above the Fermi surface and zero everywhere else such that

$$V_{\mathbf{k}\mathbf{k}'} = \begin{cases} V & \text{if } |\tilde{\epsilon}_{\mathbf{k}}| \text{ and } |\tilde{\epsilon}_{\mathbf{k}'}| \leq \hbar\omega_D \\ 0 & \text{otherwise} \end{cases} \tag{3.3}$$

Upon converting the sum in equation 3.2 to an integral over energy and solving, it becomes apparent that Δ has no $\mathbf{k}$ dependence and can be written as $\Delta = \Phi e^{i\phi}$. This is known as

an "s-wave" superconductor. In fact, the isotropic energy gap depends on the density of states at the Fermi surface and the magnitude of the attractive interaction and is on the order of a few meV. In the weak-coupling limit where $N_0V \ll 1$, the gap can be written as $\Delta = 2\hbar\omega_D e^{-1/N_0V}$ and the transition temperature is $T_c = 1.13\hbar\omega_D e^{-1/N_0V}$. Thus the value of the gap at $T = 0$ is

$$\Delta_0 = 1.764 k_B T_c. \tag{3.4}$$

This is a universal relation between the energy gap and T_c for all conventional superconductors in the weak-coupling limit. This finite gap over the entire Fermi surface leads to an absence of any electronic states for energies less than this gap.

$$N(E) = \begin{cases} N_0 \frac{E}{\sqrt{E^2-\Delta^2}} & (E > \Delta) \\ 0 & (E < \Delta) \end{cases} \tag{3.5}$$

Conventional superconductors are often metallic and thus above $T = T_c$, the specific heat $C_v(T) = \gamma T$ as expected in a normal metal. At $T = T_c$ there is a jump in the specific heat, $\Delta C = |C_N - C_{SC}|$, followed by a thermally activated behavior proportional to $e^{-\Delta/(k_B T)}$, that is, it decays exponentially as the temperature is further lowered below T_c. This behavior is illustrated in figure 3.2.

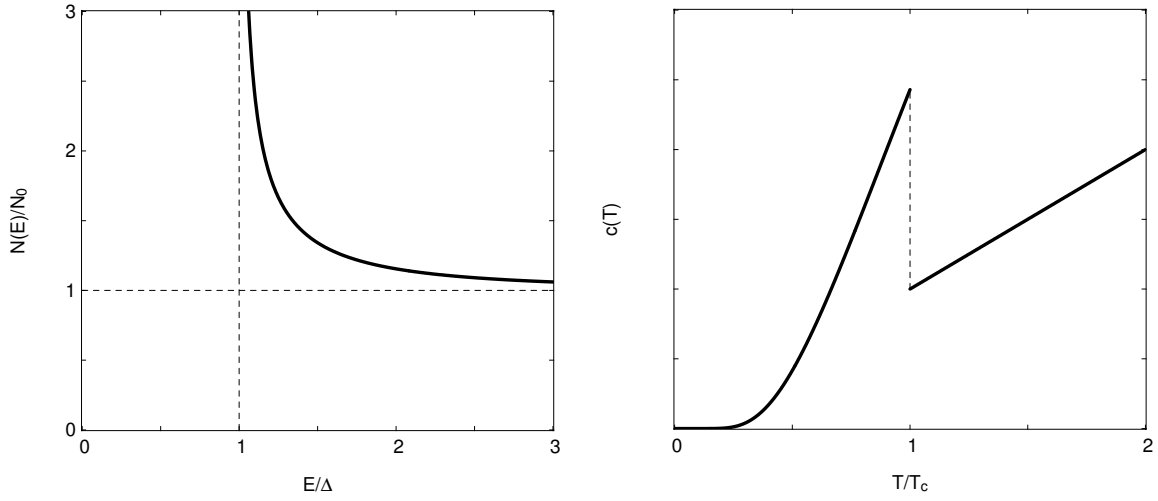

Figure 3.2: Density for state (left) and specific heat (right) of a conventional superconductor.

BCS theory states that for a conventional superconductor in the weak-coupling limit the jump in specific heat normalized by the normal state specific heat at T_c is a universal

ratio given by:

$$\frac{\Delta C}{\gamma T_c} = \frac{|C_N - C_{SC}|}{C_N}\bigg|_{T=T_c} = 1.43 \tag{3.6}$$

A similar universal ratio exists for the critical field such that

$$\frac{\gamma T_c^2}{H_c^2(0)} = 1.68 \tag{3.7}$$

The thermal conductivity will also decay exponentially because $\kappa \sim \int dE N(E)\tau(E)$. Although the relaxation time, τ diverges as the temperature goes to zero, since there are fewer states to scatter into, the density of states is zero and thus κ also tends to zero. Near $T = T_c$ the electronic contribution is dominant but as $T \to 0$ $\kappa_e \to 0$ because electrons are forming cooper pairs which do not carry any entropy and thus the conductivity is dominated by the phonon conductivity when $T \lesssim 0.3T_c$. The phonon conductivity will then be limited by the sample boundaries. In these s-wave superconductors, it has been shown that the conductivity is insensitive to non-magnetic impurities because they do not effect superconducting gap and also do not break cooper pairs. Aluminum is a good example of a BCS superconductor in the weak coupling limit. Low temperature thermal conductivity of aluminum can be seen in figure 3.3. Despite a large difference in impurities in the three samples, it has little effect on the conductivity since the presence of non-magnetic impurities has no effect on the gap and thus the conductivity is still dominated by phonons.

3.4 Unconventional Superconductors

Unconventional superconductors can be most generally defined as superconducting materials that do not conform to BCS, or Eliashberg, theory. Unconventional superconductivity often arises due to a non-phonon mediated pairing mechanism which may have a $\mathbf{k}$ dependence that can be written in a separable form. That is, $V_{\mathbf{k}\mathbf{k}'} = \eta_{\mathbf{k}} V \eta_{\mathbf{k}'}$ and $\Delta_{\mathbf{k}} = \Delta_0 \eta_{\mathbf{k}}$ where $\langle \eta_{\mathbf{k}'} \rangle = 0$ and $\langle \eta_{\mathbf{k}'}^2 \rangle = 1$. The energy gap is then found to be

$$\Delta_0 = 2\hbar\omega_D e^{-1/N_0 V} e^{-2\alpha_{2l}} \tag{3.8}$$

where $\alpha_{2l} \equiv \langle \eta_{\mathbf{k}'}^2 \ln|\eta_{\mathbf{k}'}| \rangle$. Many unconventional superconductors have a nodal, d-wave gap symmetry. In two dimensions, d-wave symmetry is achieved when $\eta_{\mathbf{k}} = \sqrt{2}\cos(2\theta)$ [22].

Nodes in the superconducting gap allow low energy electronic quasi-particles which carry momentum even when $E < \Delta$ which is forbidden in the s-wave case! These low energy quasi-particles impose many implications involving transport, specific heat and other

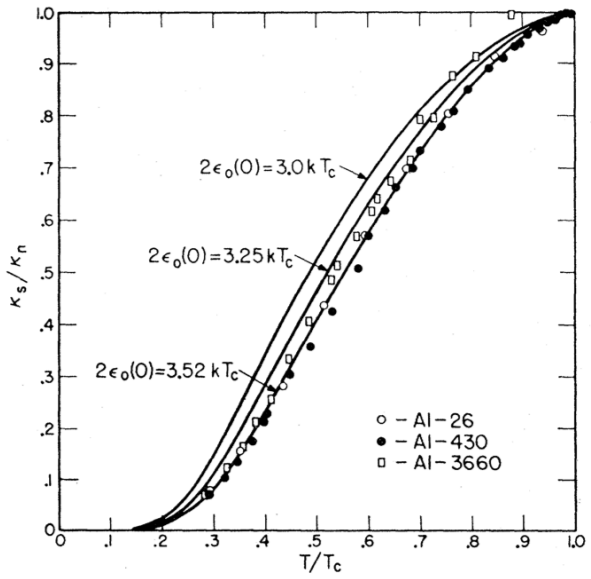

Figure 3.3: Thermal conductivity of aluminum normalized by the normal state conductivity. Although the residual resistivity ratio (RRR) ranges from 26 to 3660, they all lie very close to the curve predicted by BCS theory which predicts $\Delta = 1.76 k_B T_c$ [21].

physical properties as they dominate the low temperature electronic properties. These important consequences involve power law temperature dependence in charge and thermal transport, specific heat and penetration depth as opposed to the thermally activated behavior seen in the isotropic, s-wave gap symmetry. The exact behavior of these properties depend on the type of node exists in the order parameter. If a line node exits in the gap (as in the polar gap symmetry) then the density of states is linear in energy for $E < \Delta$. Point nodes can be linear in k (type I) and results in the density of states being quadratic in energy so that $N(E) \propto E^2$ or quadratic in k (type II) leading a linear energy dependence to the density of states such that $N(E) \propto E$.

Unlike in the isotropic gap scenario, impurities have an effect on the low energy density of states in a nodal superconducting gap since they alter the regime where $E < \Delta$. We will concern ourselves with a linear density of states as in the $d_{x^2-y^2}$ symmetry (d-wave) superconductors. We can define the impurity bandwidth, γ, as the point where the density of states deviates from the expected linear behavior in a pure d-wave and remains approximately constant for $T \to 0$. This non-vanishing density of states is due to impurities which break the Cooper pairs. These low energy quasi-particles behave like a normal Fermi-sea and thus produce a linear term in the thermal conductivity right down to $T = 0$ for the

range in T over which $N(\epsilon)$ is constant.

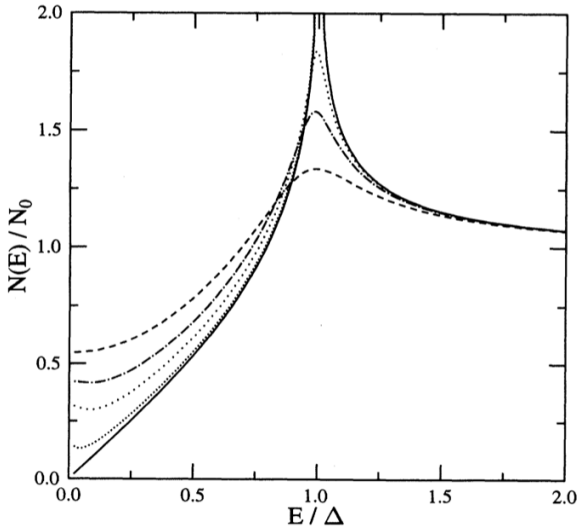

Figure 3.4: Density of states of an unconventional d-wave superconductor with $\Gamma/\Delta = 0$ (solid line), 0.01 (densly dotted line), 0.05 (dotted line), 0.1 (dash-dotted line), 0.2 (dashed line) [23].

Before we discuss the implications of strong (unitary) and weak (Born) scattering on the scattering rate, I will first make a quick note on the concept of "clean" and "dirty" systems. A convenient definition of the clean limit is when $\gamma < T \ll \Delta$ so that the density of states is linear energy and we can safely ignore the impurities. Similarly, the dirty limit is when $T < \gamma$ which occurs when the pair breaking impurities lead to a constant, non-zero density of states.

Now we can articulate the effect of Born and unitary scattering on the scattering rate in both the clean and dirty limits, while sticking with the d-wave symmetry. We can define τ as the quasi-particle relaxation time and δ is the scattering phase shift. In the weak scattering limit (Born) then $\delta = 0$ and it can be shown that:

$$\frac{1}{\tau} = \begin{cases} \Gamma\omega & \text{clean} \\ \gamma = 4\Delta_0 e^{-\pi\Delta_0/2\Gamma} & \text{dirty} \end{cases} \tag{3.9}$$

Here, the impurity bandwidth is very small in the dirty limit, indicating that the impurity scattering does not affect the density of states until very low temperatures ($T \lesssim \gamma$). If we look at the strong scattering limits (unitary) then $\delta = \pi/2$, which is the maximum phase

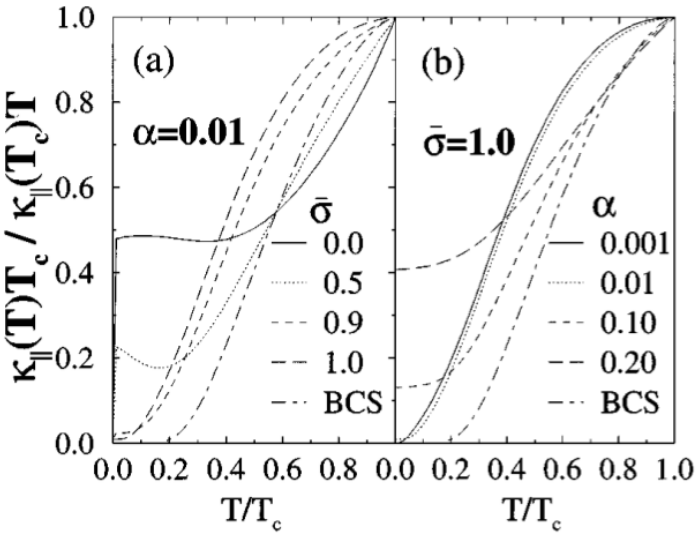

Figure 3.5: Thermal conductivity of an unconventional d-wave superconductor [24].

shift, and the inverse of the relaxation time is [25]:

$$\frac{1}{\tau} = \begin{cases} \Gamma/(\omega \ln^2 \omega) & \text{clean} \\ \gamma = 0.63\sqrt{\Delta_0 \Gamma} & \text{dirty} \end{cases} \tag{3.10}$$

In this case, the 'dirty limit' is realized over a larger temperature range. As stated earlier, the density of states is linear in energy ($N(E) \sim E$) in the clean limit. However, we are concerned with the low temperature regime, where impurity scattering dominates and the density of states is approximately constant. This finite density of states in the dirty limit leads to a universal electronic component to the thermal conductivity such that:

$$\frac{\kappa_e}{T}(T) = \left[\frac{\kappa_0}{T} + \frac{7\pi^2}{15}\left(\frac{a^2 T}{\gamma}\right)^2\right] \tag{3.11}$$

where a is a constant dependent on the scattering strength. The linear term is universal in the sense that it does not depend on the scattering rate and is given by [26]:

$$\frac{\kappa_0}{T} = \left(\frac{4}{\pi}\frac{\hbar\Gamma}{\Delta_0}\frac{1}{\mu}\right)\frac{\kappa_n}{T} \tag{3.12}$$

where μ is the slope of the gap at a node which is equal to 2 for a pure d-wave superconductor. Although there is a Γ in the expression for $\kappa_0(T)$ in equation 3.12, the normal

state conductivity, κ_n, is inversely proportional to the scattering rate, confirming the universality of the linear term in the electronic thermal conductivity. For a full derivation of the d-wave thermal conductivity see Graf et al. 1996 [24].

We have now seen that impurities in the presence of a nodal superconducting gap lead to a non-zero density of states at $T = 0$. This causes a finite residual linear electronic thermal conductivity for $T \to 0$. We have also seen that in the case of a d-wave superconductor the value of the linear term is universal but the T^3 temperature dependence is strongly dependent on scattering, in particular, the impurity bandwidth γ.

The high-T_c copper-oxide (cuprate) superconductors have been shown to have d-wave pairing symmetry. What is interesting about these unconventional superconductors is that the electron pairing is not mediated by an electron-phonon interaction as in the conventional superconductors but rather by magnetic fluctuations. Classically, magnetism was though to compete with superconductivity, which would have a detrimental effect on the critical temperature. However, a balance of superconductivity and magnetism seems to exist in the cuprates as can be seen in their temperature vs. doping phase diagram in figure 3.6.

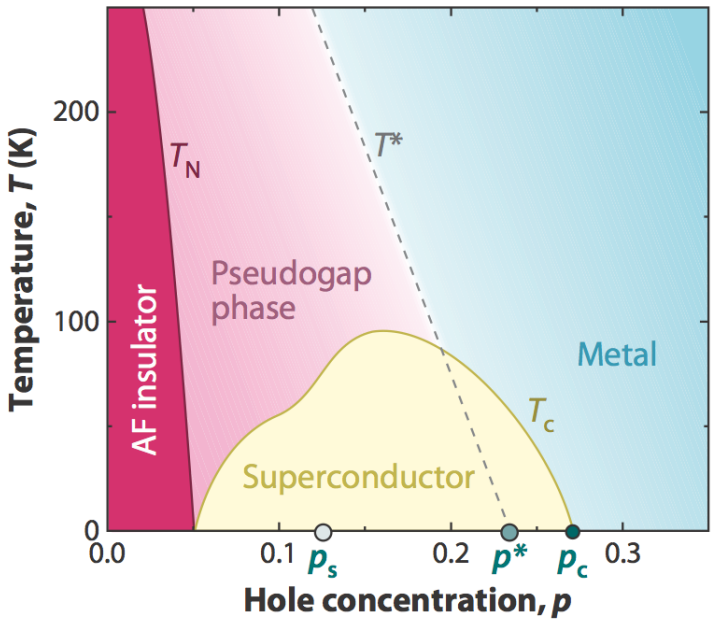

Figure 3.6: General phase diagram for the high T_c cuprate superconductors [27].

3.5 Superconductors in a magnetic field

As we have seen earlier, one of the defining properties of a superconductor is the Meissner effect, that is, in the superconducting state, the net magnetic field is zero ($B = 0$). Therefore, superconductors are perfect diamagnets which means that the magnetism, M, is a linear function of the applied field, H, such that $B = H + 4\pi M = 0$. The application of a magnetic field on superconducting materials will have varying effects depending on the type of superconductor. Type-I superconductors will behave perfectly diamagnetically until a critical magnetic field, H_c, at which point superconductivity is suppressed and the system becomes 'normal' with zero magnetization (figure 3.7). This behavior is often seen in conventional, s-wave superconductors. Type-II superconductors, however, have two critical

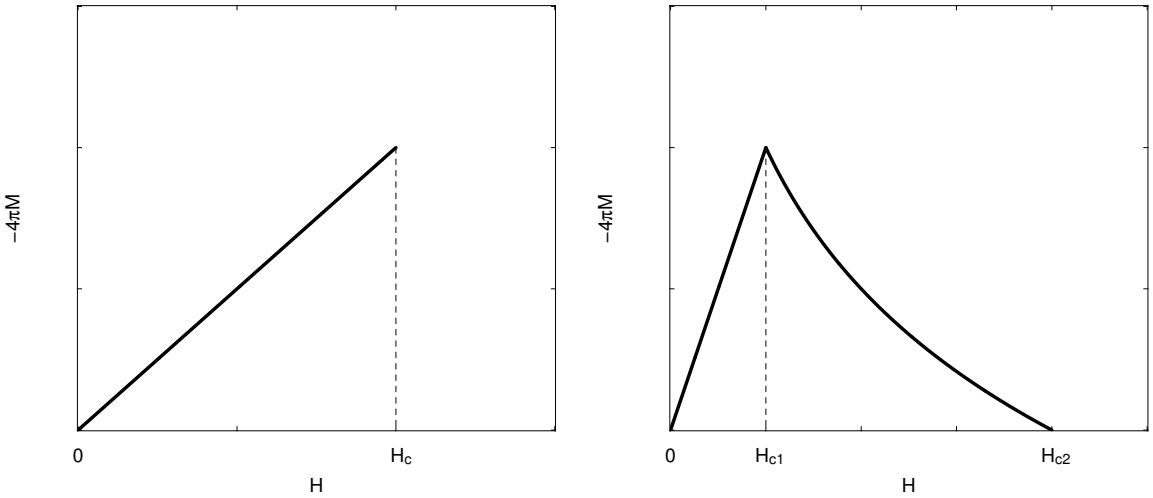

Figure 3.7: Magnetism vs applied field for type-I (left) and type-II (right) superconductors.

fields, a lower critical field, H_{c1}, and an upper critical field, H_{c2}. Below the lower critical field, H_{c1}, The system behaves as a perfect diamagnet with a linear magnetization. For $H_{c1} < H < H_{c2}$, the magnetization does not jump to zero due to the suppression of superconductivity as it does in a type-I superconductor, in fact the magnetization decays to zero exponentially with the full suppression of superconductivity occurring at the upper critical field H_{c2} (figure 3.7). In this state, tubes of magnetic flux, known as vortices, are allowed to penetrate the superconductor which are screened by loops of current maintaining zero magnetic field in the bulk of the superconductor.

The magnetic flux associated with each vortex is quantized to be $\Phi = hc/2e$. This flux quantization is taken as evidence for cooper pairs since the quantum mechanical magnetic

flux quanta is hc/q^* for a charge q^*, and in this case the charge is $2e$ because the flux comes from a bound pair of electrons which form the screening current around each vortex. The vortices arrange themselves into a triangular lattice known as the Abrikosov flux lattice (figure 3.8).

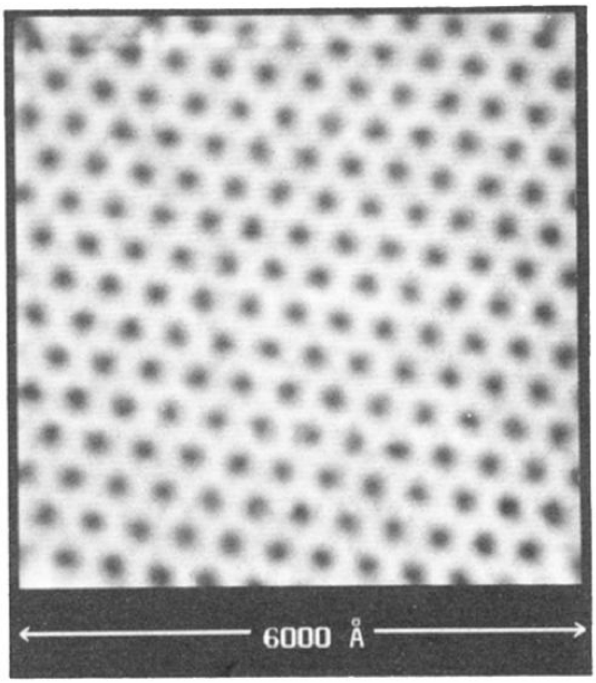

Figure 3.8: Scanning-Tunneling-Microscope (STM) image of the Abrikosov flux lattice in $NbSe_2$ at 1.8 K in a field of 1 T observed by Hess *et al.* in 1989 [28].

The electronic quasiparticle states outside of the vortices are Doppler shifted due to the superfluid flow around the vortices. This will lower the energy of some of the states, making them accessible by the quasiparticle excitations, thus increasing the density of states at the Fermi energy. It can be shown that the density of states at the Fermi energy is proportional to $\sqrt{H}$ [25]. Calculating the thermal conductivity is much more complicated as it also involves the scattering rate. In conventional type-II superconductors the quasiparticle mean free path is determined by the vortex density whereas impurity scattering dominates in d-wave superconductors. The thermal conductivity due to the electronic quasiparticles in conventional superconductors will initially decrease due to vortex scattering, then increase rapidly to the normal state value at H_{c2}. In d-wave superconductors at low temperature and field, the electronic contribution to the thermal conductivity increases with an applied

magnetic field with a field dependence qualitatively similar to $\sqrt{H}$ [29, 30].

3.6 Iron-based superconductors

Due to the detrimental effect magnetism has on superconductivity, magnetic materials have been avoided in the search for higher transition temperature superconductors. However, in 2008, Hosono *et al.* discovered superconductivity in the iron based material LaFeAsO with a critical temperature 26 K when doped with fluorine [31]. The discovery of this new class of iron-based superconductors sparked a flood of interest because of the magnetic nature of the parent compound with the discovery of more than 50 iron based, superconducting materials. These iron based materials share many similarities to other unconventional superconducting materials (high-T_c cuprates, heavy fermion superconductors and many organic superconductors) such as having a non-phonon mediated pairing mechanism and the importance of chemical substitution in enabling superconductivity as in the case of the cuprates. Unlike in the cuprates, chemical substitution in the active planes (the iron planes as we shall soon see) of the iron based superconductors can enhance the critical temperature. Examining the ground states of these systems is important to build an accurate picture of this unconventional superconductivity. We will begin by looking at the crystal structure of the iron-based superconductors.

3.6.1 Crystal Structure

To date, five distinct crystal structures have been observed to support superconductivity in the iron based superconductors. All of these structures share a common plane consisting of iron atoms arranged on a square lattice joined by a tetragonally situated pnictogen (P, As) or a chalcogen (S, Se, Te) alternating above and below the Fe plane. This plane is analogous to the copper-oxygen planes in the high T_c cuprate superconductors which is believed to be where superconductivity originates [32]. The structure of the iron based superconductors can be as simple as stacking these iron layers, as in FeSe. However there is often an additional layer stacked in between the iron layers which is known as a blocking layer since it imposes a somewhat two-dimensional quality to the crystal. The additional spacing layer is comprised of one of the following: alkali (Li), alkaline-earth (Ba), rare-earth oxide/fluoride (LaO or SrF) or a more complicated collection of atoms (such as the perovskite $Sr_3Sc_2O_5$). The five crystal structures that support superconductivity in iron based materials are seen in figure 3.9.

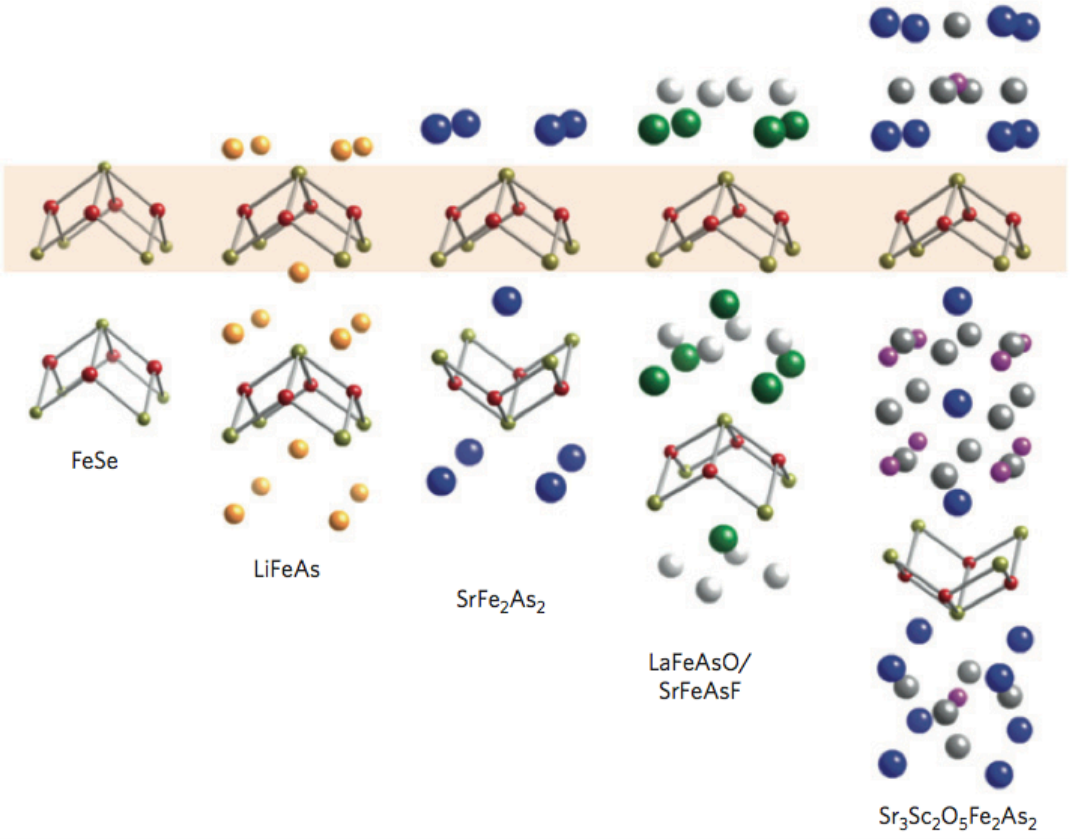

Figure 3.9: The five distinct tetragonal structures which support superconductivity in iron based materials [32].

3.6.2 Electronic band structure

The electronic band structure has been calculated using the local density approximation [33] which reveals several bands which cross the Fermi-energy (E_F) both electron-like and hole-like. The Fermi-surface consists of two quasi-cylindrical hole pockets at the center of the Brillouin zone where $\mathbf{k} = (0, 0)$ (the $\mathbf{\Gamma}$ point) and two electron pockets located at $\mathbf{k} = (0, \pm\pi)$ and $\mathbf{k} = (\pm\pi, 0)$ [34, 35]. Since the location of the two pnictogens/chalcogens are staggered above and below the Fe plane, the unit cell must contain two iron atoms, so the Brillouin zone gets folded onto itself, and thus the electron pockets are located at $\mathbf{k} = (\pm\pi, \pm\pi)$ (the $\mathbf{M}$ point). This is illustrated in figure 3.10 where the Fermi-surface of $BaFe_2As_2$ with a 10% Co substitution is shown.

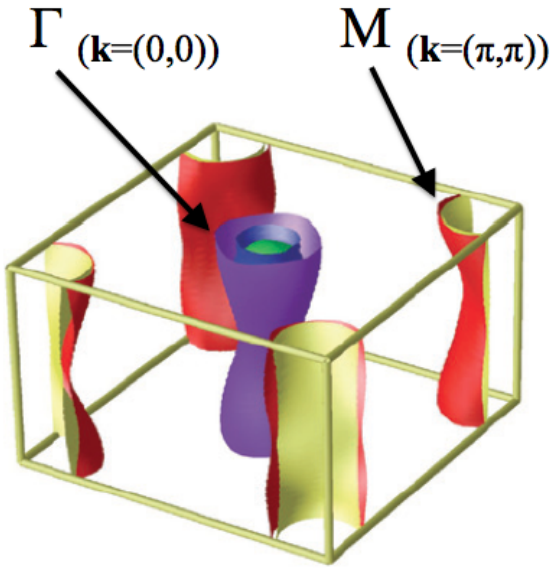

Figure 3.10: The Fermi-surface of $BaFe_2As_2$ doped with Co. Two hole pockets are located at $\mathbf{\Gamma}$ and two electron pockets are located at $\mathbf{M}$ [32].

This calculation qualitative agrees exceptional well with experiment. Angle-resolved photoemission spectroscopy (ARPES) measurements on LaFePO [36] and quantum oscillations measurements on $NdFeAsO_{0.9}F_{0.1}$ [37] and $Ba_{0.6}K_{0.4}Fe_2As_2$ [38] all show excellent agreement with this multiband Fermi-surface, with two hole pockets at the center of the Brillouin zone ($\mathbf{\Gamma}$) and two electron pockets at the corners of the Brillouin zone ($\mathbf{M}$).

3.6.3 Structure of the order parameter

The multiband nature of the Fermi-surface can lead to many possibilities for the symmetry of the superconducting order parameter which can be quite exotic. The simplest possibility is the isotropic $s\pm$ symmetry which is similar to the s-wave (as described earlier) such that the gap is constant for all momenta but with a sign change between the two bands. A modification of this order parameter is the nodal $s\pm$ or anisotropic $s\pm$ such that one band has a fairly isotropic gap and the other with either deep minima or accidental (not symmetry induced) nodes. The other possible order parameter is the d-wave symmetry which is nearly degenerate with the anisotropic $s\pm$ gap [39].

ARPES [38], penetration depth [40] and some thermal conductivity measurements [41] have revealed fully gaped superconductivity in many compounds. This being said, low temperature penetration depth measurements on LaFePO [42] and on $BaFe_2(As_{1-x}P_x)_2$ [43] show signs of low-energy quasi-particle excitations which are indicative of a line node in the gap. This inconsistency may be due to intraorbital interactions [44] and the exact details of the electron and hole nesting in the Fermi-surface [45] in determining different gap topologies. The picture becomes even more complex because in the case of the isotropic $s\pm$ gap, disorder can create subgap excitations which appear as a low-energy density of states giving the illusion of nodes in the gap. However, the residual linear contribution to thermal conductivity resulting from the disorder induced density of states is usually on the order of 1% of the normal state conductivity [46]. This is not the case since a substantial linear term is observed in the thermal conductivity of $BaFe_2(As_{0.67}P_{0.32})_2$ [43] indicating the presence of nodes. Thus, the fully gapped isotropic $s\pm$ scenario is generally ruled out due to experimental evidence. None the less, due to the fact that the energies of these gap symmetries are so close it is clear that extreme care must be taken to experimentally resolve whether the low-energy states are intrinsic (caused by nodes) or extrinsic (caused by disorder). NMR Knight shift measurements have also shown that the Cooper pairs are singlet in nature [47, 48, 49, 50].

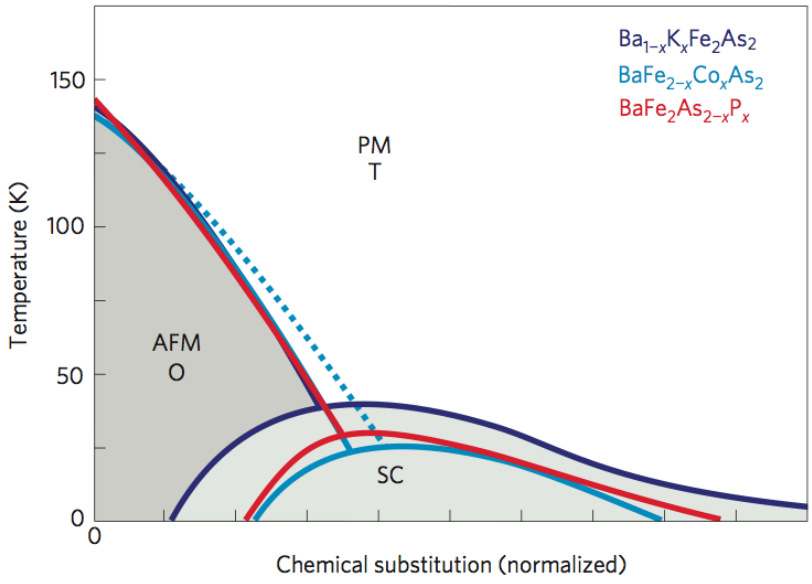

Figure 3.11: Temperature vs. chemical substitution for a variety of iron based superconductors [32].

The phase diagram of the iron based superconductors also shares many similarities with the cuprates as can be seen in figure 3.11. There is a delicate balance between magnetism and superconductivity. In fact, although the pairing mechanism remains unknown in the iron based superconductors, it is thought to be magnetic in nature rather than mediated by phonons due to a weak phonon-electron interaction. The iron based superconductors however are metallic in their normal state which differs from the cuprates that are magnetic insulators.

Chapter 4

Frustrated Magnetism

4.1 A Toy Model

To understand frustration in magnetic systems, it is advantageous to first look at a toy model. We will consider an Ising spin system with antiferromagnetic exchange on a two dimensional triangular lattice which was first investigated by Wannier and Houtappel [51, 52]. The Hamiltonian of such a system is

$$H = -J_{ex} \sum_{\langle ij \rangle} \mathbf{S}_i \cdot \mathbf{S}_j \tag{4.1}$$

where J_{ex} is the exchange energy which is negative in the case of antiferromagnetism and $\mathbf{S}_i$ is the spin at site i taking the value of ± 1 representing spin up or down. It is trivial to find the ground state in the case of a ferromagnetic interaction ($J_{ex} > 0$) since all the nearest neighbor exchange interactions are satisfied when all the spins pointing up or down. The situation becomes far more interesting when considering an antiferromagnetic exchange coupling ($J_{ex} < 0$) on a triangular lattice. Figure 4.1 shows how the antiferromagnetic interaction can be satisfied between any two spins, but attempting to satisfy the second exchange will force a violation of the third exchange. Minimizing the energy in the Hamiltonian thus results in a six-fold degenerate ground state with a residual entropy. It is worth noting that this degeneracy does not exist on a square lattice since all the antiferromagnetic interactions are able to be satisfied. This illustrates how the degeneracy is imposed by the geometry of the system, hence the name 'geometric frustration'.

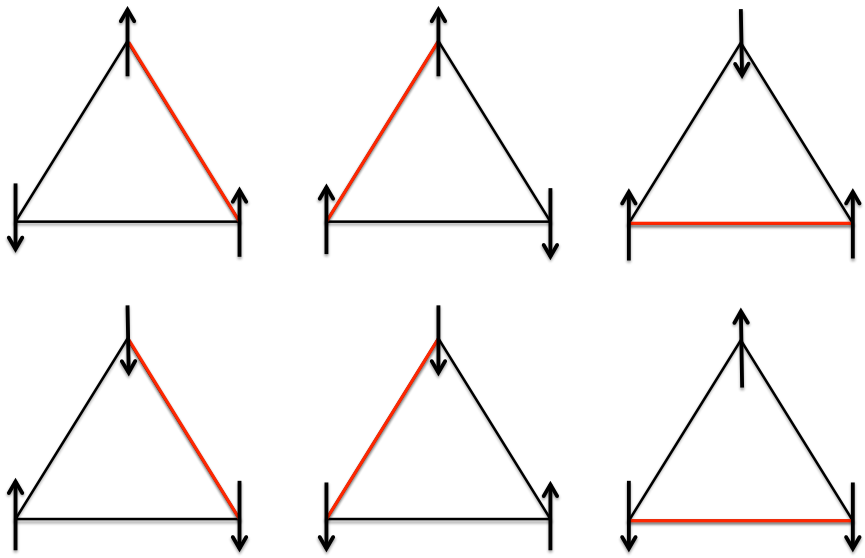

Figure 4.1: Six-fold degenerate ground state of Ising spins on a triangular lattice with an antiferromagnetic nearest neighbor interaction.

4.2 Rare-earth Titanates

4.2.1 Definition

A three-dimension analogue of the triangular lattice is that of the corner sharing tetrahedral lattice, which is often referred to as a pyrochlore lattice. The 'pyrochlore' nomenclature stems from the fact that $Na_2Nb_2O_6F$ tends to burn green when ignited [53]. The name is borrowed in this case because they share the same crystal structure (figure 4.2). This three dimensional system was first studied in the context of a frustrated magnetic system in 1956 by Anderson [54]. He noticed that an Ising spin system with a nearest-neighbor exchange on the pyrochlore lattice also results in a residual entropy. In fact, he recognized that this system shared many similarities to water ice. In water ice, hydrogen ions follow the so-called Bernal-Fowler ice rules such that two ions are situated near (covalent bond) each oxygen atom and two are situated far (hydrogen bond) with the oxygen atoms locaed on the diamond lattice (dual lattice of the pyrochlore) [55]. Anderson mapped the ice rules to the spins on the vertices on each tetrahedra so that two spins were pointing up and two were pointing down along the global z-direction with six possible permutations. As

in water ice, this degeneracy leads to a residual entropy which is very close to Pauling's zero-point entropy for water ice of $S_0 = (R/2)\ln(3/2)$.

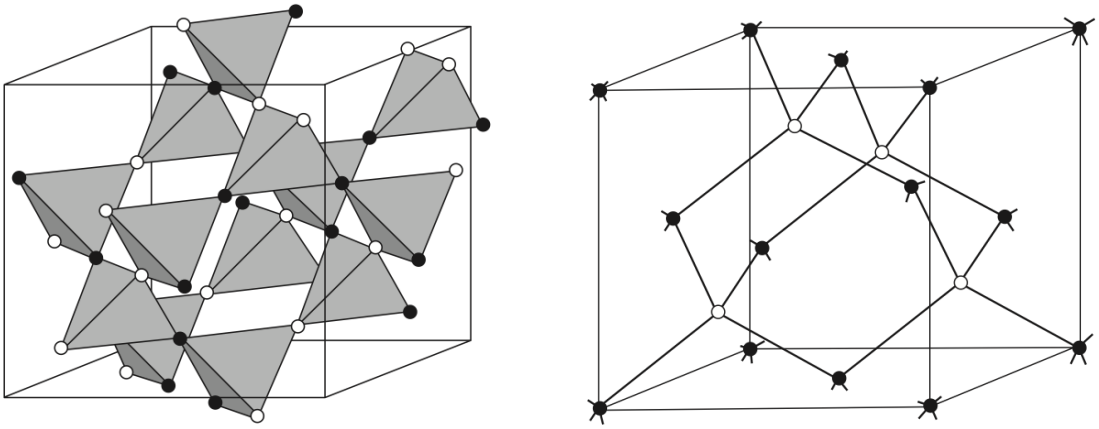

Figure 4.2: (a) Pyrochlore lattice. (b) Diamond lattice, dual lattice of the pyrochlore with sites at the centers of each tetrahedron [56].

We will focus on materials with chemical formulas of the form $A_2B_2O_7$ where A^{3+} is a trivalent rare earth metal located on the tetrahedral lattice sites and B^{4+} is often a tetravalent transition metal located on the diamond lattice. For this study, we focus on materials where A^{3+} is a magnetic ion (Dy^{3+} or Ho^{3+} for example) and B^{4+} is nonmagnetic Ti^{4+}. We call this specific class of materials the rare-earth titanates. A few rare-earth ions which are often found in these materials are listed in table 4.1 along with their electron configuration, ground state term and measured p value [5].

Element	Electron configuration	Ground-state	Measured p
Tb^{3+}	$4f^8$	$^7F_6$	9.5
Dy^{3+}	$4f^9$	$^6H_{15/2}$	10.6
Ho^{3+}	$4f^{10}$	$^5I_8$	10.4
Er^{3+}	$4f^{11}$	$^4I_{15/2}$	9.5
Yb^{3+}	$4f^{13}$	$^2F_{7/2}$	4.5

Table 4.1: Some rare-earth ions that are often found in the titanates of the form $A_2Ti_2O_7$. Their basic electron configuration, ground-state term and measured p values are also listed.

The p value is the effective Bohr magneton number used in Curie's law for magnetic

susceptibility which states:

$$\chi = \frac{1}{3}\frac{N}{V}\frac{\mu_B^2 p^2}{k_B T} \tag{4.2}$$

Curie's law provides a good description of insulating magnetic materials containing rare-earth ions which behave paramagnetically. That is, the spins favor alignment with an external magnetic field.

4.2.2 Hamiltonian

The Hamiltonian for the rare earth titanates is much more complicated than in the two dimensional triangular lattice we looked at earlier. This is true in general for real systems. The Hamiltonian is comprised of three main parts, a crystal field term, the Zeeman term and the hyperfine term such that

$$H = H_{CF} + H_{Zee} + H_{hf} \tag{4.3}$$

with the largest coming from the electric crystal fields in zero applied magnetic field. The most general form of the crystal field Hamiltonian can be written as:

$$H_{CF} = \sum_i \sum_{l,m} B_l^m O_l^m(J_i) \tag{4.4}$$

Here, B_l^m are the crystal field parameters, O_l^m are the Stevens operator equivalents and J_i is the angular momentum operator [53]. The Stevens operator equivalents are a convenient way to evaluate the matrix elements of the crystal field potential. A few common lower order operators are given in table 4.2.

O_l^m	in $\lvert J, m\rangle$ basis
O_2^0	$3J_z^2 - J(J+1)$
O_2^2	$\frac{1}{2}(J_+^2 - J_-^2)$
O_4^0	$35J_z^4 - 30J(J+1)J_z^2 + 25J_z^2$ $- 6J(J+1) + 3J^2(J+1)^2$
O_4^4	$\frac{1}{2}(J_+^4 + J_-^4)$
O_6^6	$\frac{1}{2}(J_+^6 + J_-^6)$

Table 4.2: Select low-order Stevens operator equivalents.

The crystal field parameters, B_l^m, are determined through high resolution optical spectroscopy measurements. For more information on Stevens operator equivalents and the crystal field Hamiltonian see references [57, 58].

The Zeeman term will contribute mainly when an external magnetic field is present and will lift the (2J+1) degeneracy of the ground state. The Hamiltonian associated with the Zeeman contribution is written as

$$H_{Zee} = -g_J \mu_B \vec{J} \cdot \vec{H} \tag{4.5}$$

Here g_J is the g-factor ($g_J = 5/4$ for the J=8 ground state of the Ho^{3+} ions), μ_B is the Bohr magneton and $\vec{H}$ is the magnetic field due to applied external fields and the internal field in the ferromagnetic state. Similarly the hyperfine interaction splits the energy levels further and can be written as

$$H_{hf} = A_j \vec{J} \cdot \vec{I} \tag{4.6}$$

where A_j is the strength of the hyperfine interaction and $\vec{I}$ is the nuclear angular momentum. These interactions are much smaller that the overall electric crystal fields and only slightly lift the (2J+1) degeneracy of the ground state energy level, splitting it into a collection of singlets and doublets. However, we are mainly concerned with the ground state term since it is often the only accessible level at low temperatures and thus we will not focus our attention on these additional interactions.

In order to determine whether the ground state is a singlet or a doublet, we can take advantage of Kramer's theorem. It states that the energy levels of rare-earth ions with an odd number of valence electrons (Dy, Er, Yb) are split into doublets in zero field. Ions of this type are called Kramers ions. However, rare-earth ions with an even number of electrons (Tb, Ho) can split into a collection of doublets or singlets and are known as non-Kramers ions. The electric crystal fields then determine which of the energy levels are accessible.

4.3 Dipolar Spin Ice

As mentioned earlier, the ground-state of an Ising spin system with a nearest-neighbor interaction on a pyrochlore lattice has many similarities to water ice. Before we study these similarities further, we will first examine some properties of water ice. Recall that the locations of the hydrogen ions in water ice is governed by the Bernal-Fowler ice rules such that two hydrogen atoms are located close (hydrogen bonded) to each oxygen atom and two hydrogen atoms are located farther (hydrogen bonded) from each oxygen atom (see figure 4.3). The ice-rules lead to six possible orientation per oxygen atom and thus results in a highly degenerate ground state. This degeneracy in turn causes a residual entropy which is well described by Pauling's zero-point entropy such that $S_0 = (R/2)\ln(3/2)$.

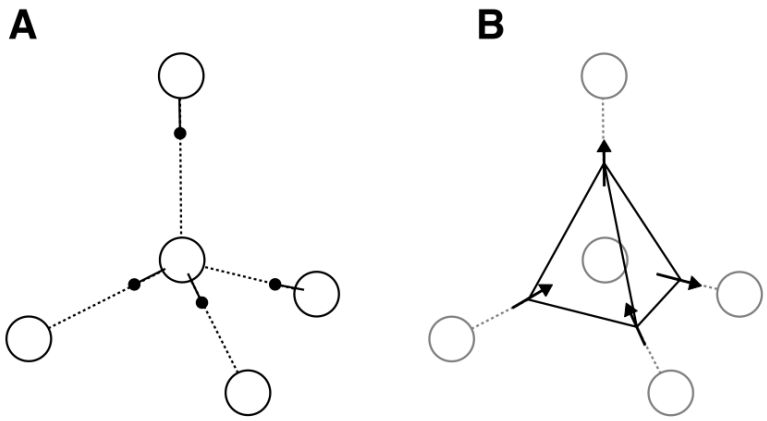

Figure 4.3: **(A)** A schematic view of the local proton arrangement in water ice. The oxygen ions (large open circles) are situated on the diamond lattice sites, that is, each oxygen ion is coordinated tetrahedrally with four other oxygen ions. Two protons (small black circles) are located near (covalent bonded) and two protons are located far (hydrogen bonded) from each oxygen ion. This is the so called Bernal-Fowler 'ice rules'. **(B)** A single tetrahedron from the pyrochlore lattice (centered on the diamond lattice) seen in HTO or DTO with magnetic moments (the arrows) located on the vertices which are aligned parallel to the local $\langle 111 \rangle$ direction. The direction which the spins point is analogous to the locations of the protons in water ice such that two spins are pointing in and two spins are pointing out of each tetrahedron. This illustrates the analogy between water ice and spin ice, hence the name 'spin-ice' [59].

We will focus our attention on $Dy_2Ti_2O_7$ (DTO) and $Ho_2Ti_2O_7$ (HTO). Note that Dy^{3+} is a Kramers ion with $J = 15/2$ and thus the ground state is a doublet. Conversely, Ho^{3+} is a non-Kramers ion with $J = 8$ so the ground state could be either a spin singlet or a doublet. However, due to the local crystal field, the ground state in $Ho_2Ti_2O_7$ is in fact a spin doublet. Early susceptibility measurements have revealed that both of these ions have very large magnetic moments at low temperatures of approximately $\mu = 10\mu_B$ with an antiferromagnetic exchange interaction. Now, unlike Anderson's model where the spins were aligned along the global z-axis, in DTO and HTO, the spins are quantized along the local $\langle 111 \rangle$. That is, the spins are either pointing directly into or out-of each tetrahedron. The ground state maintains the same six-fold degeneracy which Anderson described except in this case two spins point into and two spins point out-of each tetrahedron.

To be certain of the $\langle 111 \rangle$ quantization of the spins in HTO, Jana and Ghosh calculated

the crystal field parameters and found that the splitting between the ground state doublet and the next excited state is ∼215 K [60]. The susceptibility can be calculated using these values to be $\chi_{\parallel}/\chi_{\perp} \sim 180$ at 10 K. This ratio describes the anisotropy of the spins which align parallel to the local ⟨111⟩ direction rather than perpendicular. The splitting was measured by Rosenkranz to be 236 K using neutron spectroscopy [61]. Similarly susceptibility measurements show that $\chi_z/\chi_{\perp} \sim 350$. Therefore, even though Ho^{3+} is a non-Kramers ion, the ground state is still a well isolated doublet with $|J, m_j\rangle = |8, \pm 8\rangle$ quantized along the local ⟨111⟩ direction. We know from Kramers theorem that the ground state of DTO is a doublet with $|J, m_j\rangle = |15/2, \pm 15/2\rangle$. This is verified since the separation from the ground state doublet and the next excited state is ∼348 K and $\chi_z/\chi_{\perp} \sim 300$ [60, 61].

Specific heat measurements of DTO have shown that the magnetic contribution displays a broad peak centered at about 1.2 K seen in figure 4.4. This is in good agreement with Monte Carlo simulations in zero field. Recall that the entropy can be calculated from the specific heat via:

$$S_{mag}(T) = \int_0^T \frac{C_{mag}(T^*)}{T^*} dT^* \tag{4.7}$$

Also note that the entropy of a system of Ising spins in the paramagnetic state is $S = R\ln(2)$ and will be achieved when $T \gtrsim 10$ K. As it turns out, the broad peak observed in the specific heat measurement of DTO does not account for all of the expected entropy. In fact, the residual entropy is very close to Pauling's entropy! Hence, these rare-earth titanates have been termed 'spin ices' because of the analogy to water ice.

The magnetic specific heat is much more convoluted in HTO since the Ho^{3+} ions carry a large nuclear heat capacity. This reveals itself as a large peak in the specific heat just below 500 mK in addition to the broad peak at 2 K similar to the one seen in DTO. This is illustrated in figure 4.5. The large nuclear contribution can be fitted to a Schottky peak in order to extract the magnetic contribution which shows a broad peak at 2 K, indicating the development of the spin ice correlations. The magnetic contribution is also in good agreement with Monte Carlo simulations that leads to a residual entropy close to Pauling's entropy.

One other curiosity is that the specific heat in both DTO and HTO shows no sign of ordering right down to the lowest temperatures measured (∼50 mK). The ordering of the spins would reveal itself as a peak in the specific heat akin to a phase transition.

The spins not only have an anti-ferromagnetic nearest neighbor exchange coupling but also a large dipole-dipole interaction which is ferromagnetic. The large dipole term is a

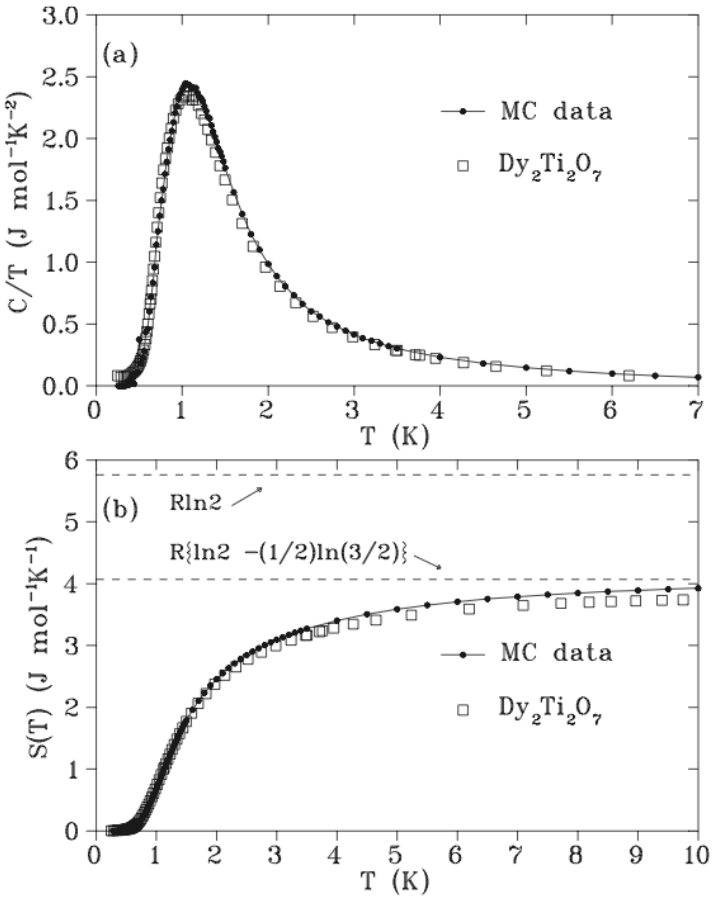

Figure 4.4: Experimental and Monte Carlo simulations of the specific heat (top) and entropy (bottom) of $Dy_2Ti_2O_7$ [62, 63].

result of the large magnetic moment exhibited in these materials. Thus these materials are often referred to as dipolar spin ice. A theoretical model describing the dipolar spin ice model has been developed by den Hertog an Gingras. The Hamiltonian has an exchange interaction, J, and a long range dipole coupling term, D:

$$H = -J \sum_{(ij)} S_i^{\hat{z}_i} \cdot S_j^{\hat{z}_j} + D r_{nn}^3 \sum_{i>j} \frac{S_i^{\hat{z}_i} \cdot S_j^{\hat{z}_j}}{|\mathbf{r}_{ij}|^3} - \frac{3(S_i^{\hat{z}_i} \cdot \mathbf{r}_{ij})(S_j^{\hat{z}_j} \cdot \mathbf{r}_{ij})}{|\mathbf{r}_{ij}|^5} \tag{4.8}$$

Due to the local $\langle 111 \rangle$ quantization of the spins, the nearest neighbor exchange energy is defined as $J_{\rm nn} = J/3$. The dipole-dipole interaction can be written as $D = (\mu_o/4\pi) g^2 \mu^2 / r_{\rm nn}^3$

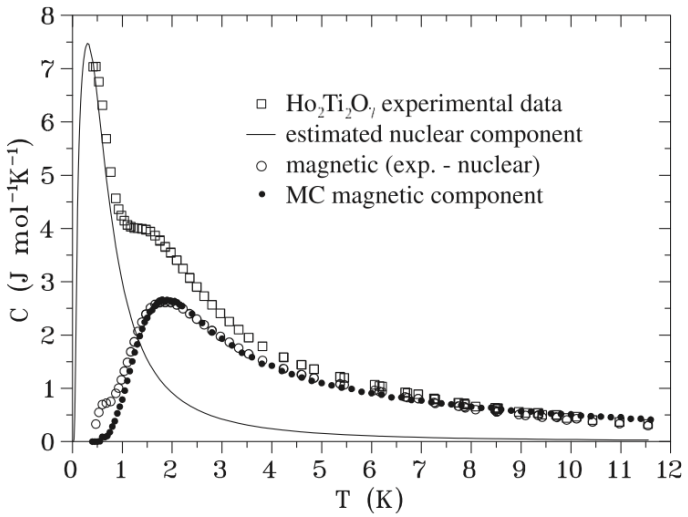

Figure 4.5: Specific heat of $Ho_2Ti_2O_7$ [64]. The data agrees with Monte Carlo simulations after subtracting off the Schottky peak.

and at nearest neighbor distance, $D_{\text{nn}} = 5D/3$. This Hamiltonian can be simplified to an effective nearest neighbor exchange defined as $J_{\text{eff}} \equiv J_{\text{nn}} + D_{\text{nn}}$ which retains the nearest neighbor spin ice physics. The Hamiltonian can then be written as:

$$H = -J_{\text{eff}} \sum_{(ij)} S_i^{\hat{z}_i} \cdot S_j^{\hat{z}_j} \tag{4.9}$$

Figure 4.6 shows a phase diagram of T/D_{nn} vs $J_{\text{nn}}/D_{\text{nn}}$ was mapped out via Monte Carlo simulations using a standard single Ising spin flip Metropolis algorithm. We see that for ratios above $J_{\text{nn}}/D_{\text{nn}} \geq -0.91$ a spin ice ground state is realized. A four-in-four-out anti-ferromagnetic state exists below this ratio. It is important to note that the long range dipolar term was correctly accounted for using an Ewald summation rather than truncating the sum at the fifth nearest neighbour as in Refs. [66, 67] which can lead to frivolous results. Properly accounting for all long range dipole-dipole interactions via an Ewald summation successfully recovers the spin ice ground state in both DTO and HTO. The nearest neighbor exchange coupling is $J_{\text{nn}} \sim -1.24$ K for DTO and $J_{\text{nn}} \sim -0.52$ K for HTO. The nearest neighbor dipole-dipole coupling is $D_{\text{nn}} \sim 2.35$ K for both DTO and HTO. Therefore the effective exchange coupling is net ferromagnetic in both cases with $J_{\text{eff}} \sim 1.1$ K for DTO and $J_{\text{eff}} \sim 1.8$ K for HTO.

Melko and Gingras introduced non-local dynamics into the simulation to impede the

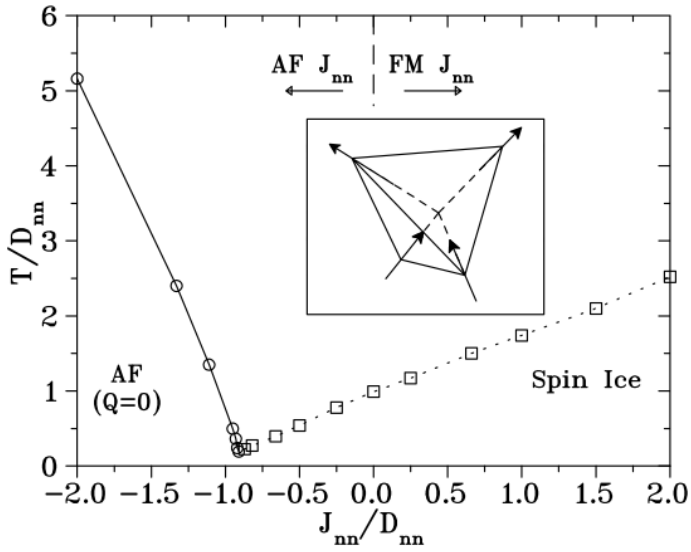

Figure 4.6: T/D_{nn} vs. J_{nn}/D_{nn} phase diagram produced by den Hertog and Gingras [65].

freezing of the spins by developing a loop algorithm which provides a method to release the trapped entropy in the spin ice state. This essentially speeds up the slow, low temperature dynamics and promotes the creation of a long range ordered state. Simulations reveal a long range ordered ground state described by $\mathbf{q} = (0, 0, 2\pi/a)$ (and the other two symmetrically equivalent wave-vectors) which satisfies the ice rules but recovers all of Pauling's entropy. Specific heat and consequently the entropy is obtained from these simulations and is seen in figure 4.7. The specific heat displays a broad peak similar to experiments but there is a large peak indicative of a first order transition at about 180 mK. This causes the entropy to have a plateau at Pauling's entropy followed by a rapid drop to zero, indicating the recovery of all the $R\ln(2)$ entropy. The resulting phase diagram of of $T/D_{\rm nn}$ vs $J_{\rm nn}/D_{\rm nn}$ is seen in figure 4.8 which shows the ordered state occurring at 180 mK regardless of the values of $J_{\rm nn}$ and $D_{\rm nn}$ as long as $J_{\rm nn}/D_{\rm nn} \geq -0.91$. Although each loop of spin flips may cause minimal change in the overall energy, there is an initial large energy barrier to overcome in order to access the other nearly degenerate ground states. That is, upon cooling the crystal, the spins freeze into a two-in-two-out state and spin flips become unfavorable, this leads to large energy barriers that separate the nearly degenerate ground states. It may not be feasible to overcome this energy barrier experimentally. Thus this ordered ground state has not been officially realized to date.

Before going any further, I will first quickly mention that in addition to the absence of

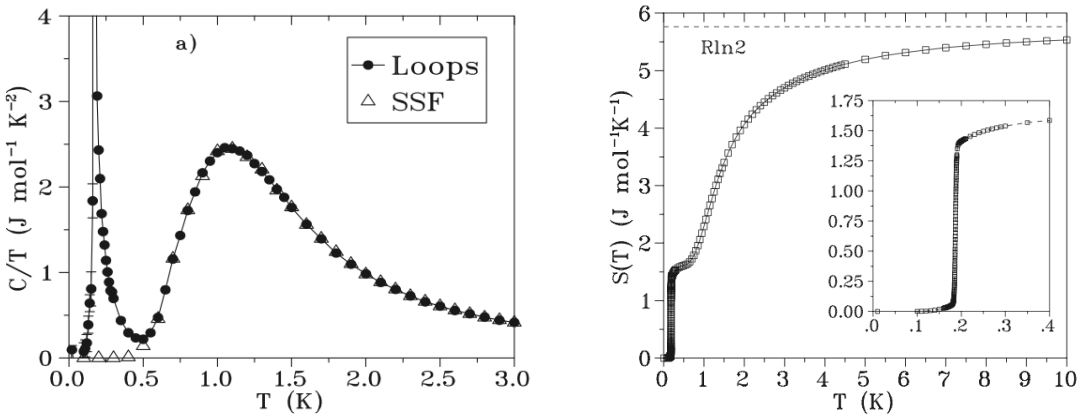

Figure 4.7: Monte Carlo simulations of specific heat (left) and entropy (right) for a spin ice system including a loop flip algorithm, illustrating the onset of an ordered state below 0.5 K [63].

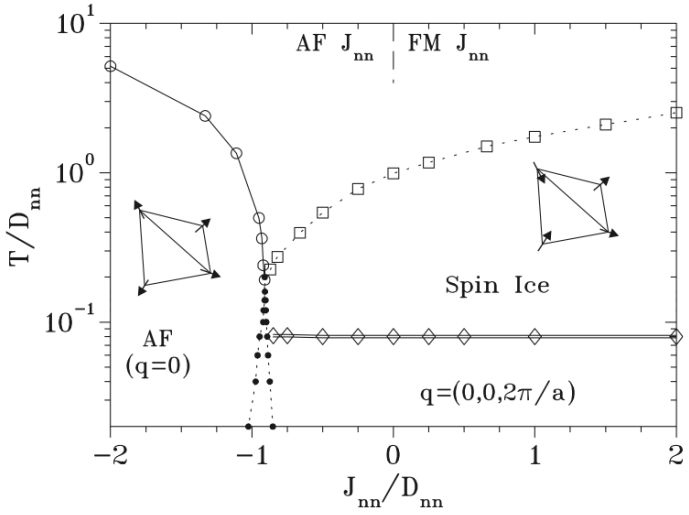

Figure 4.8: T/D_{nn} vs. J_{nn}/D_{nn} phase diagram with ordered ground state from loop flip algorithm simulation [63].

an ordered ground state, a slowing of the spin dynamics is observed via ac-susceptibility measurements. Matsuhira *et al.* [68] first discovered this unconventional freezing in polycrystalline samples of $Ho_2Ti_2O_7$ and $Ho_2Sn_2O_7$ in 2000 when he noticed that the relaxation time was well described by a thermally activated Arrhenius behaviour with energy barriers

of 27.5 K and 19.6 K respectively. Shortly after this discovery, both Matsuhira *et al.* [69] and Snyder *et al.* [70] separately performed similar measurements on the relaxation times in both temperature and frequency space in DTO. Matsuhira found that above 10 K, DTO displays a thermally activated behaviour with an activation energy of 220 K. Below 10 K, the temperature dependence of the relaxation time flattens into a plateau until about 2 K. At which point there is a crossover to a second thermally activated behaviour is seen below 2 K with an energy barrier of approximately 10 K associated with a single relaxation mode. Snyder went a step further and included the application of an externally applied magnetic field. The applied magnetic field enhanced the freezing temperature which is inconsistent with the freezing seen in spin glasses, where an applied field suppresses the freezing temperature.

4.3.1 Spin ices in a magnetic field

The effects of the application of a magnetic field to a spin ice material is greatly anisotropic. The effect of an external field applied along three main cubic symmetries ([100], [110], [111]) of the pyrochlore lattice are examined via magnetization measurements which is used in conjunction with specific heat measurements to create a B vs. T phase diagram.

H ∥ [100]

A magnetic field applied along [100] will effect all spins equally. Thus, the application of a magnetic field will induce long range order.

H ∥ [110]

Applying a field in the [110] direction will decouple the spins into isolated, perpendicular chains. The α chain is parallel to [110] and the β chain is along $[1\bar{1}0]$ and is thus not affected by the magnetic field. The α spins are thus free to align with the magnetic field whilst not violating the two-in-two-out ice rules.

H ∥ [111]

The pyrochlore lattice can be thought of as alternating stacked layers of kagome planes and triangular planes in the [111] direction. Now recall that the spins are quantized in the local $\langle 111 \rangle$ which points directly into or out-of each tetrahedron. So, the spins on the

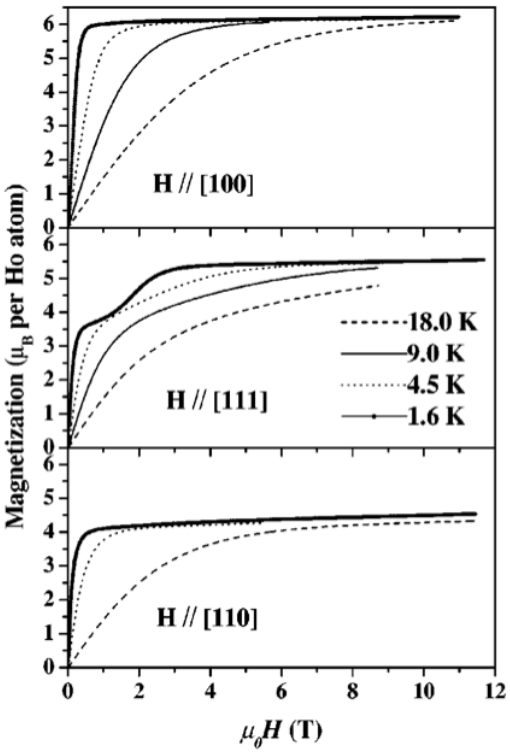

Figure 4.9: magnetization curves of DTO with the field along (a) [100], (b) [111] and (c) [110] [71].

triangular planes are perpendicular to the plane (parallel to the [111] direction) and the spins on the kagome planes will have components both in the plane and perpendicular to the plane. Applying a magnetic field along a global [111] direction will thus be parallel to one spin in each tetrahedron and it will effect the other three spins equally with a lesser magnitude. So, at low temperatures (in the spin ice state) a single spin in each tetrahedron will align with the magnetic field leaving the other three spins free to satisfy the ice rules. This special case of the 3-D spin ice state is referred to as the "kagome ice" state since the spins in the triangular lattice are ordered (aligned with the field) leaving a degenerate number of ground states for the spins in the kagome planes to satisfy the ice rules. Note that excitations out of this state are confined to the 2-D kagome planes, perpendicular to the field. When the field is raised further, the spins in the kagome planes will attempt to align with the field which violates the ice rules (3-in-1-out) and leads to a fully polarized state.

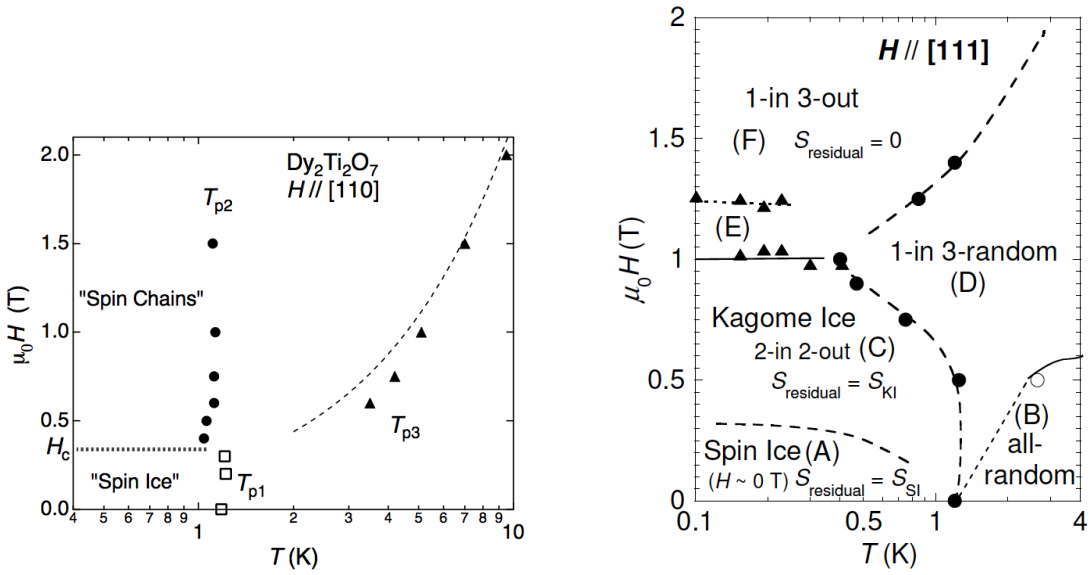

Figure 4.10: $H \parallel [110]$ [72] and [111] [73] phase diagrams for $Dy_2Ti_2O_7$.

4.4 Magnetic monopoles

4.4.1 Introduction to Monopoles

Phenomena occurring in nature is often follows a symmetrical pattern. Thus one might expect a magnetic monopole charge as a counterpart to the electron from Maxwell's equations. If you have ever played with bar magnets you know that obtaining a monopole is not as simple as breaking that magnet in half, instead you end up with two smaller magnets, each with their own north and south poles. The search for a magnetic monopole started long ago in 1931 when Dirac established that they were allowed under the quantum mechanical formalism such that their quantized magnetic charge was equal to $q = m\hbar c/e$ where m is an integer or half integer. These monopoles were termed 'non-Abelian' monopoles whose gauge theory predicted huge masses on the order of tens of TeV. This is way outside of the range of current particle accelerators (LHC is presently operating at about 4 TeV [74]). Thus the direct search for free monopoles is currently futile.

Fortunately for us the story does not end here. In 2008, Castelnovo *et al.* proposed a fractionalized magnetic monopole quasi-particle as an excitation out of the spin ice ground state. A monopole anti-monopole defect pair is created upon a single spin flip resulting in a

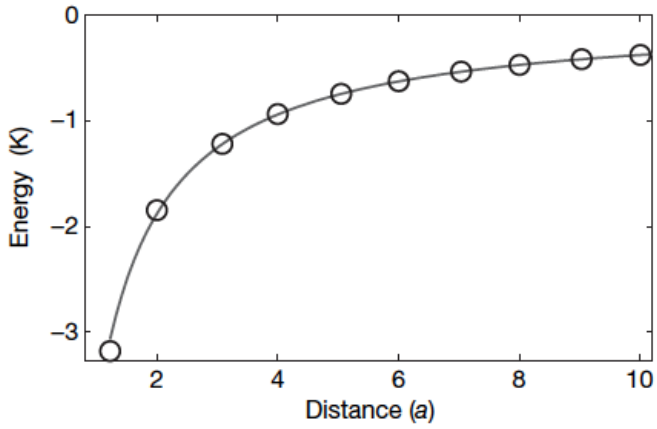

Figure 4.11: Coulomb energy versus distance in units of lattice spacing, a [75].

tetrahedron with 3 spins in, 1 spin out (monopole) and a tetrahedron with 1 spin in, and 3 spins out (anti-monopole). Figure 4.12 a-d illustrates a way to think about each individual spin as a dipole with a north (red ball) and a south pole (blue ball). So the 2-in-2-out state will have two positive charges and two negative charges in each tetrahedron. Now, when one of these dipoles flips one tetrahedron will have three positive charges and one negative charge resulting in a net positive charge and similarly a corresponding tetrahedron will have a net negative charge. This charge is quantified as $q_m = \pm 2\mu/a_d$ where a_d is the diamond lattice constant (distance between the center of neighboring tetrahedra). What is interesting is that subsequent spin flips separating the the monopole anti-monopole defect pair does not further violate the ice rules, rather they behave as free particles interacting with a coulomb potential. The coulomb interaction energy is described by $-\mu_o q_m^2/(4\pi r)$. It is important to note that the coulomb energy at nearest neighbor distance is equal to 3.06 K [75]. The separation of the monopole anti-monopole pair does however leave a trail of flipped spins which is known as a Dirac string, this is seen in figure 4.12 e).

It turns out that Ryzhkin had proposed the existence of monopoles as defects in the spin ice ground state in 2005, three years earlier! He likened them to ionic defects in water ice, that is when an oxygen atom has three hydrogen ions near and one far, and another oxygen atom only has one hydrogen ion near and three far. Ryzhkin went on to derive an expression for the frequency dependence of the susceptibility:

$$\chi(\omega) = \frac{q^2/\Phi}{1 - i\omega\tau} \tag{4.10}$$

such that ω is the frequency of the applied magnetic field, q is the magnetic charge, and

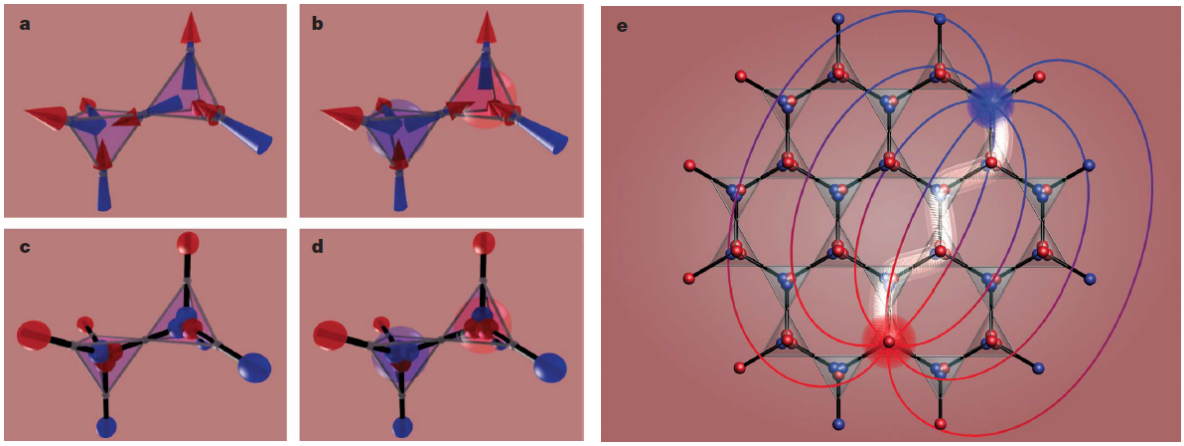

Figure 4.12: The dumbbell model illustrating the creation of a monopole anti-monopole pair. (a) Spin-ice ground state configuration with two spins pointing in and two spins pointing out of each tetrahedron. (b) A single spin flip causes one tetrahedron to have three spins in, one spin out and a neighbouring tetrahedron with one spin in, three spins out. (c,d) The arrows are replaced with dumbbells. (e) Subsequent spin flips separate the monopole anti-monopole pair which are connected by a Dirac string [75].

$\tau^{-1} = (\mu_1 n_1 + \mu_2 n_2)\Phi$ is the relaxation time with $\Phi = 8/\sqrt{3}ak_BT$ and where μ_i is the mobility and n_i is the defect density. This theoretical work assumes that the magnetic point defects (monopoles) are non-interacting.

4.4.2 Observation

After Castelnovo proposed the idea of magnetic monopoles in spin ice materials, a flurry of experiments searching for signatures of monopoles were conducted in a short amount of time. Experiments attempting to probe monopole dynamics include neutron scattering, muon spin resonance (μSR), specific heat and thermal conductivity measurements. There has also been several attempts to theoretically describe the monopole behaviour using Monte Carlo simulations, Debye-Hückel theory and Onsager's theory of weak electrolytes. A brief overview of these methods will now be discussed.

Jaubert and Holdsworth started by imposing a Coulomb gas of monopoles constrained to the diamond lattice (centers of the tetrahedra) in a spin ice [76]. Monte Carlo simulations were used to obtain characteristic relaxation timescales of the Dirac strings connecting monopole anti-monopole pairs. These time scales were then compared to the times scales

extracted from the ac-susceptibility measurements of DTO by Snyder *et al.* [77]. Similar characteristics were seen in the simulations that were observed experimentally such as the unconventional crossover regime between the plateau state to the low temperature Arrhenius behaviour at around 2 K. Although the agreement is not perfect, the development of the low temperature freezing into the spin ice state is well described to 1 K as can be seen in figure 4.13. This provides additional experimental evidence supporting the monopole picture.

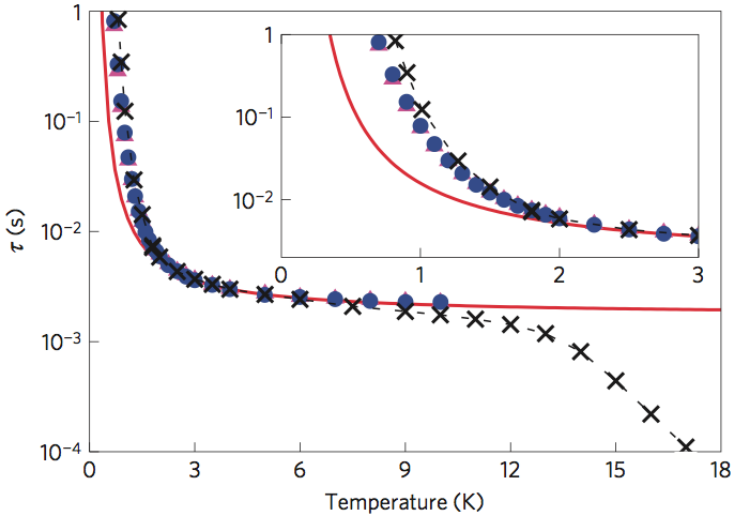

Figure 4.13: Relaxation times extracted from ac-susceptibility measurements of DTO in comparison with Monte Carlo simulations [76].

Neutron scattering measurements were made on HTO and DTO by Fennell *et al.* and Morris *et al.* respectively. Fennell used polarized neutron scattering measurements to separate spin flip and non-spin flip correlations by analyzing the polarization. This method is the only way to observe pinch points in in the neutron scattering. These pinch points are interpreted as reciprocal space evidence for a long range Coulomb force which is dipolar in nature. This result was corroborated with good agreement from Monte Carlo simulations. Confirmation of a low temperature Coulomb phase in HTO strengthens the monopole picture in spin ice materials.

Morris focused on using neutron scattering measurements to observe Dirac strings in DTO. This was achieved by applying a magnetic field in the [001] (symmetrically equivalent to [100]) which arranges the spins into the two-in-two-out spin ice state. Monopole quasiparticles are then thermally excited out of this ground state and are free to separate

creating Dirac strings. This results in a cone of scattering seen in the neutron scattering experiment and is reproduced in simulations. He also measured the specific heat in DTO and found reasonable agreement with the Debye-Hückel theory of a dilute Coulomb gas below 1 K. This increases the evidence for monopole-like excitations out of the spin ice ground state.

Klemke used a thermodynamic field theory in conjunction with thermal relaxation and transport measurements to extract the time constants corresponding to different components of the magnetic excitations in the spin ice phase. Specific heat is used to extract two times scales below 1.1 K, τ_α^R ($\sim$ 1 to 100 s) and τ_β^R ($\sim$ 0.1 to 10 s). τ_α^R is associated with the spins along the α chain (along the [110] direction) which behave paramagnetically, since a field along [110] can easily align these spins. τ_β^R is associated with the spins along the β chain which is perpendicular to the α chain and the spins are thus effectively isolated from the α spins. The β spins are therefore treated as an Ising spin system with nearest neighbour interactions. An activated behaviour is seen below 1 K down to $\sim$ 500 mK

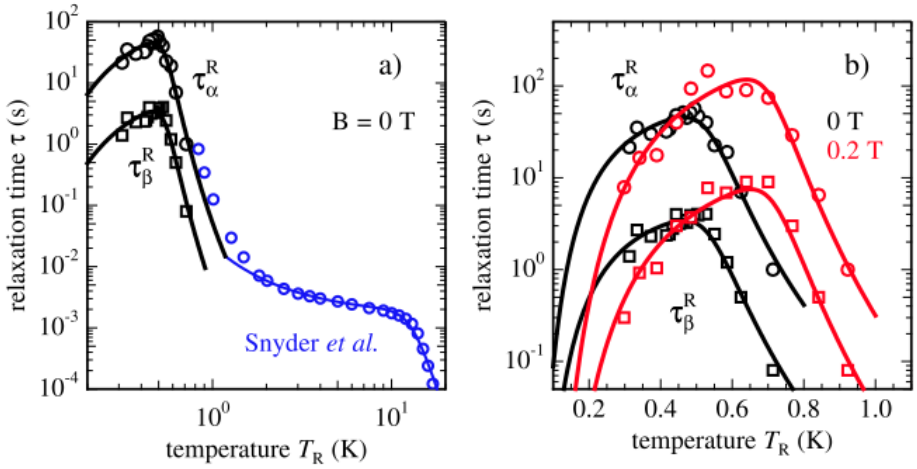

Figure 4.14: α and β relaxation times extracted from specific heat measurements of DTO [78].

at which point a plateau is reached in the relaxation time. This change in behaviour is explained as a transition from a regime with strong magnetic charge screening to a regime with weak screening of the charges [78].

A third, and much faster time scale, τ_γ^R ($\sim 10^{-8}$ s), is extracted from thermal conductivity using kinetic theory and Matthiessen's rule.

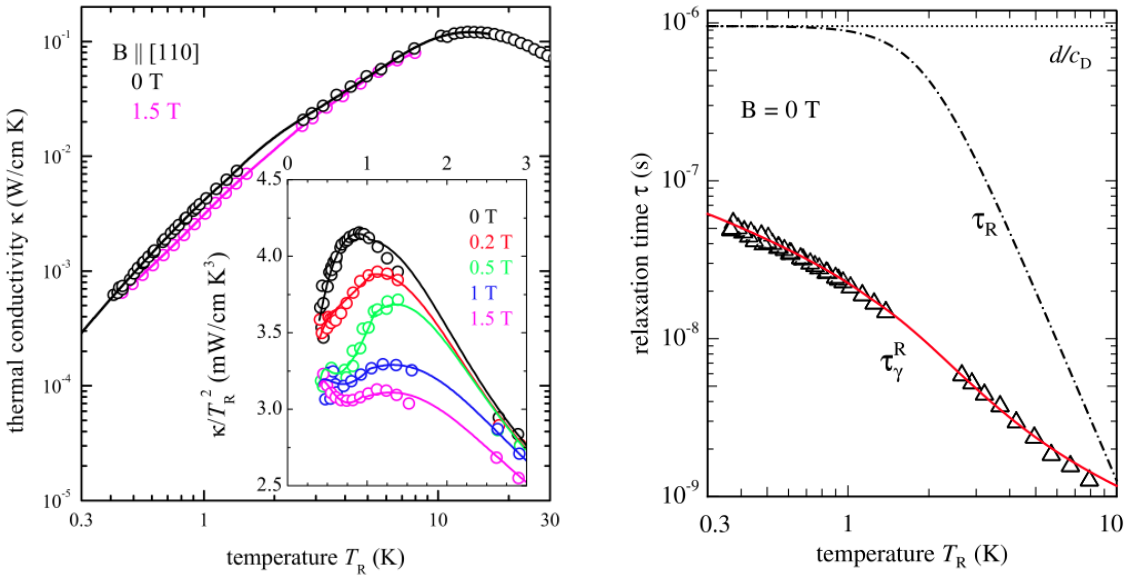

Figure 4.15: Thermal conductivity of $Dy_2Ti_2O_7$ with heat flow and applied magnetic fields parallel to [110] (left). The much faster τ_γ time constant extracted from thermal conductivity measurements (right) [78].

These relaxation times were fitted to the spin-lattice relaxation for a rare-earth salt (Kramer's salt in the case of DTO) described by Orbach. This is done under the assumptions that the magnetic excitations are localized and affect thermal transport only through their interaction with phonons. Orbach states that the spin-lattice relaxation time in a Kramers salt is determined by Raman and thermally activated processes given by:

$$\tau_\nu^R = a_\nu T_R^9 + b_\nu \exp\left(-\frac{E_\nu}{k_B T_R}\right) \tag{4.11}$$

where $\nu = \alpha, \beta, \gamma$ and E_ν is to activation energy and T_R is the thermal bath temperature. This gave good agreement with experiment above 1.3 K, including specific heat measurements by Snyder *et al.*. However, in the spin ice phase, $T_R < 1.1$ K, an attempt frequency is needed to describe the data which takes the form:

$$b_\nu(T_R) = \bar{b}_\nu + d_\nu T_R \exp\left(\frac{E_\nu + \epsilon_\nu}{k_B T_R}\right) \tag{4.12}$$

where $\bar{b}_\nu$ is the attempt frequency for strong screening and the exponential term takes into account the weakening of the screening with potential ϵ_ν. Fitting the low temperature

specific heat data yields $E_\alpha/k_B = E_\beta/k_B = 8.3$ K, and $\epsilon_\alpha/k_B = \epsilon_\beta/k_B \sim 1$ K. A fit to the low temperature thermal conductivity gives $E_\gamma/k_B = 5.3$ K, and $\epsilon_\gamma/k_B = 0.1$ K. These results were taken to be experimental proof of thermally activated monopole anti-monopole defect pairs out of the spin ice ground state.

Low temperature AC susceptibility measurements on DTO by Yaraskavitch *et al.* [79] revealed an Arrhenius behaviour with an activation energy of 9.79 K ($\sim 9J_{\text{eff}}$) down to the lowest temperatures measured (See figure 4.16). This is in contrast with the deviation from the activated behaviour seen in the inset of figure 4.16. Yaraskacitch's explanation of the discrepancy is that Klemke's data below 500 mK has in fact fallen out of spin-lattice equilibrium, leading to a much shorter relaxation time than the freezing seen in the AC susceptibility measurements. This result suggest that current monopole theories fail to capture the entire picture surrounding the creation and dynamics of monopole excitations in DTO.

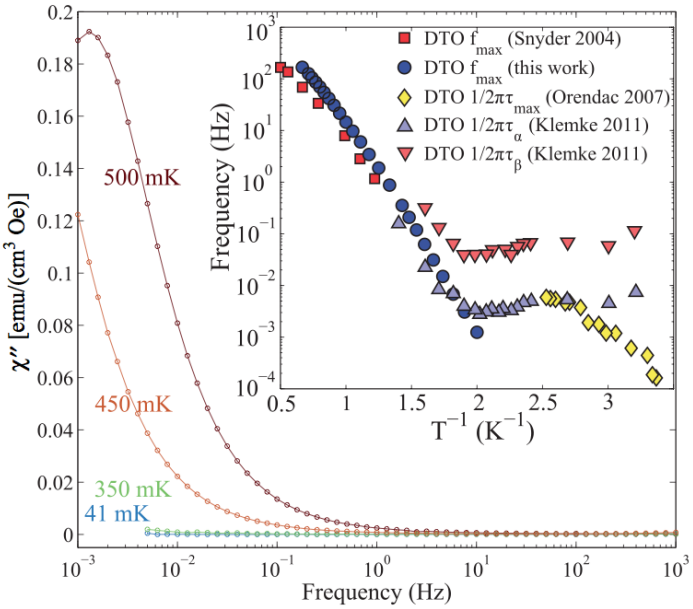

Figure 4.16: AC susceptibility of DTO by Yaraskavitch *et al.* showing the freezing behaviour in the spin-ice state. *Inset:* A comparison of a variety of measured relaxation times [77, 80, 78, 79] revealing the deviation of Ref. [78] data from the activated behaviour seen in AC susceptibility.

Debye-Hückel theory describes the interaction of a dilute Coulomb gas. It considers that an electrolyte consists of a discrete central reference ion surrounded by an atmosphere

of charge made up of the other ions. Debye Hückel theory also assumes that the distribution of ions making up the charge atmosphere is not random, but rather ions nearest to the reference ion are of opposite charge to that of the reference ion. Castelnovo *et al.* applied this theory to that of a dilute sea of monopoles in the Coulomb phase, likening the 'magnetolyte', a term originally coined by Giblin *et al.*, to that of a weak electrolyte. He was able to utilize this theory to calculate the monopole defect density per tetrahedron, $\rho(T)$, given by:

$$\rho(T) = \frac{2e^{-\Delta_d/T}}{1 + 2e^{-\Delta_d/T}} \tag{4.13}$$

where Δ_d is the dressed creation cost of a single isolated monopole which can be calculated via:

$$\Delta_d = \Delta - \frac{1}{2}\frac{E_{nn}}{\frac{\xi_{Debye}}{a_d}} \tag{4.14}$$

Here, Δ is the unscreened value of the energy required to create an isolated monopole (Δ = 4.35 K for DTO, and 5.79 K for HTO). $E_{nn} = 3.06$ K is the magnitude of the Coulomb energy between a monopole pair at nearest neighbouring sites and $a_d = \sqrt{3/2}\ a = 4.34$ Åis the diamond lattice constant, which is the distance between the center of neighbouring tetraherda. The screening length, ξ_{Debye}, is a function of monopole density, $\rho(T)$ and temperature, T and is written as:

$$\frac{\xi_{Debye}}{a_d} = \sqrt{\frac{2}{3\sqrt{3}\pi E_{nn}}}\sqrt{\frac{T}{\rho(T)}} \tag{4.15}$$

No analytic solution exists for this system of equations and therefore they must be solved self-consistently (see figure 8.6). Castelnovo attempted to describe specific heat and susceptibility with some success, however, it provided no improvement over the work of Jaubert and Holdsworth. Castelnovo mentions several methods which could improve this theory, such as including interactions between monopole pairs. He also states that Debye-Hückel theory is only applicable in the low monopole density limit which limits the usefulness of this theory to low temperatures.

Bramwell *et al.* used transverse field μSR measurements on DTO to extract the magnetic charge of a monopole and the associated magnetic current [81]. Transverse Field μSR measures the spin fluctuation rate. The rate at which this precession decayed yielded an effective elementary magnetic charge of $Q \sim 5\mu_B \mathring{A}^{-1}$.

Although this method was only accurate below 300 mK (where the effective charge is temperature independent and where there is a low density of Dirac strings), it provided

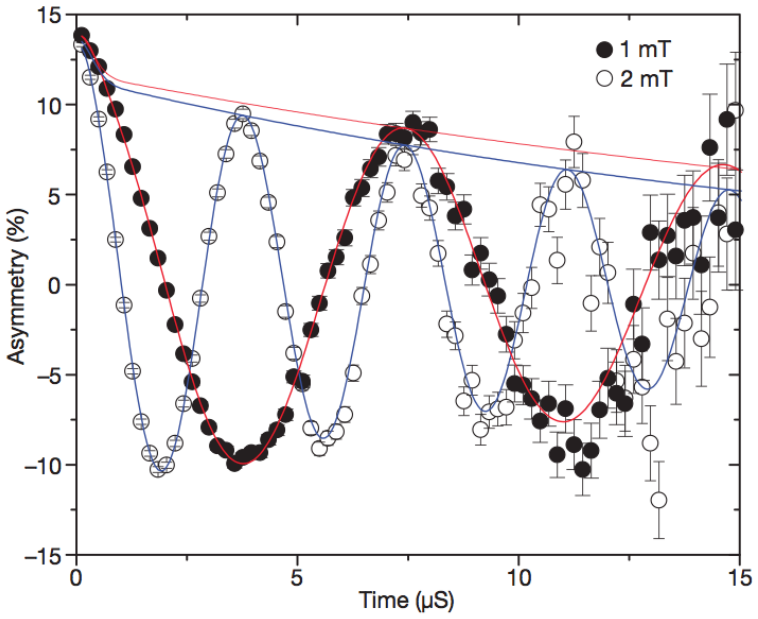

Figure 4.17: μSR measurement used to determine the effective value of the magnetic charge [81].

excellent agreement with Onsager's theory of a three-dimensional Coulombic liquid. This is because the sea of magnetic monopoles, with a coulomb interaction, is mapped onto a weak electrolyte. He uses the example of autoionization of water where $2H_2O = [H_3O^+OH^-] = H_3O^+ + OH^-$. That is, the quasiparticle vacuum is equivalent to a bound pair of charges which is then equivalent to free charges. In the case of spin ice, the bound charges are monopole antimonopole pairs which are connected by a Dirac string. A result of Onsager's theory is the dissociation constant as a function of field:

$$K(B) = K(0)\left(1 + b + \frac{b^2}{3} + ...\right) \tag{4.16}$$

where b is a dimensionless renormalized field defined by:

$$b = \frac{\mu_o Q^3 B}{8\pi k_B^2 T^2} \tag{4.17}$$

This shows that Onsager's theory provides a good description of both electric and magnetic systems.

Bramwell's μSR work [81] was refuted by Dunsiger *et al.* [82] on account that transverse field μSR is unable to resolve the monopole excitations. Monte Carlo simulations showed that the local field at the muon sites is on the order of 300 mT, which is much larger than the monopole signature, on the order of 1 mT. This shows that transverse field μSR is not an ideal candidate for detecting an Onsager effect in spin ice materials as it is not have the sensitivity. Dunsiger claimed that the exponential decay in the spin precession was actually an artifact of the GaAs sample mount. μSR measurements were made on DTO on a GaAs mount, a Ag mount and of a GaAs mount with no sample present (figure 4.18). This produced clear evidence that the muon precession seen in Ref. [81] was largely due to the GaAs sample mount. However, careful μSR measurements in various configuration revealed persistent spin dynamics below 5 K, evidence for a low temperature thermally activated behaviour.

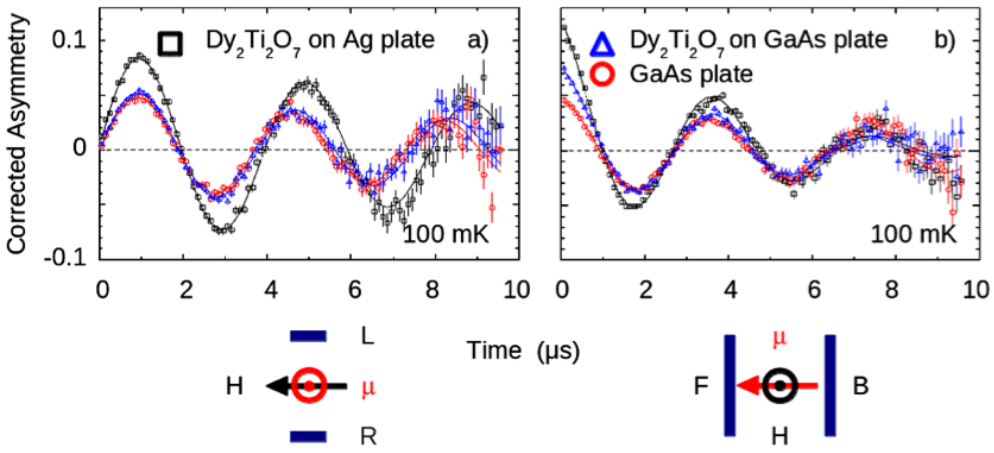

Figure 4.18: Muon spin precession of $Dy_2Ti_2O_7$ on a Ag mount and a GaAs mount as well a GaAs plate with no sample mounted measured by Dunsiger *et al.* [82]. This was used as evidence that the μSR measurements of DTO in Ref. [81] were not sensitive enough to detect monopole signatures, and they were merely measuring the sample holder.

This on going debate about the existence and dynamics of monopole excitations from the spin-ice ground state demands further investigation, both theoretically and experimentally.

Part II

Experimental Details

Chapter 5

Dilution Fridge

The ability to perform measurements at temperatures approaching absolute zero is key in understanding many phenomena in nature. Achieving this extreme environment is a non-trivial task. There are many cryostats available to get to varying base temperatures each with their advantages and draw-backs. For example, a helium-4 pump probe has a large temperature range from room temp to 1 K and is relatively easy to use. However this thesis focuses on a temperature range up to two orders of magnitude lower. Thus, a ^{3}He-^{4}He dilution fridge is needed to attain these temperatures.

5.1 How a Fridge Works

In principle, a dilution refrigerator is quite simple - mechanically driving a first order phase transition which draws a latent heat out of the surrounding system. What makes a ^{3}He-^{4}He dilution refrigerator unique, however, is the fact that this latent heat exists down to absolute zero! ^{3}He-^{4}He mixtures with a ^{3}He concentration of 6.6% or more will eventually phase separate into a ^{3}He rich phase and a ^{3}He dilute phase (^{4}He rich phase) when cooled below 0.87 K. A ^{3}He-^{4}He phase diagram is seen in figure 5.1. As the temperature approaches absolute zero the ^{3}He rich phase becomes pure but the ^{4}He rich phase will retain a constant ^{3}He concentration of 6.6%. Taking advantage of this residual ^{3}He concentration in the ^{4}He rich phase is the key to achieving such low temperatures. If we maintain the ^{3}He dilute phase at a temperature of 0.7 K then the ^{3}He vapor pressure is about 1000 times larger than that of the ^{4}He. Thus, pumping on this phase will draw ^{3}He atoms out of the dilute phase leaving it out of equilibrium. ^{3}He atoms from the rich phase will then cross the phase boundary into the dilute phase to maintain the 6.6% concentration. The act of crossing

this phase boundary results in a positive entropy change, that is, it requires energy which it gains from its environment - cooling the system. The ^{3}He vapor that is pumped away is then circulated and re-condensed into the ^{3}He rich phase.

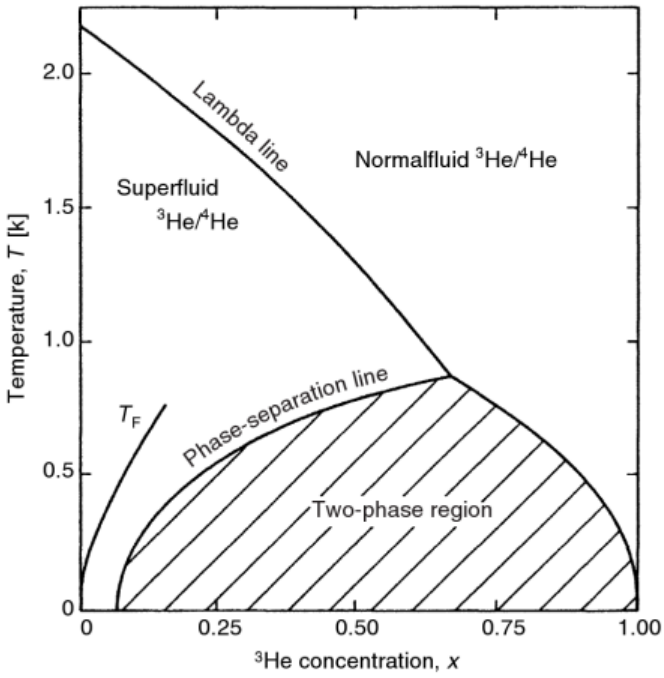

Figure 5.1: ^{3}He-^{4}He temperature vs. ^{3}He concentration phase diagram [83].

5.2 Components

Now that we know the theory of how a dilution fridge works, I will briefly discuss how it works in practice by introducing the various components involved and the procedure to run a fridge. The six main components in a dilution fridge are the mixing chamber, the still, the pumps, the cold traps, the 1K pot and the heat exchangers. A schematic drawing of a dilution fridge is featured in figure 5.2.

1. *Mixing chamber.* The mixing chamber is where the phase separation and thus all the cooling takes place. That being said, this is where your experiment must be thermally anchored.

2. *Still.* Once the ^{3}He-^{4}He mixture has phase separated, the ^{3}He rich phase will float on top of the ^{3}He dilute phase since the ^{3}He atoms are lighter than the ^{4}He atoms. A tube then connects the bottom of the mixing chamber to the still where the dilute phase is then warmed to about 0.7 K using a small heater, this is to promote the circulation of the ^{3}He by increasing its vapor pressure.

3. *Pumps.* The effectiveness of the dilution fridge is in essence a result of how quickly the ^{3}He can be circulated through the system, since the cooling power is a consequence of crossing the ^{3}He rich phase to the ^{3}He dilute phase. Thus, a powerful turbo pump, the roots pump, backed by a sealed rotary pump is needed to circulate the ^{3}He atoms. The 1K pot also requires a rotary pump to cool to 1K and will be discussed more later.

4. *Cold traps.* The tubes throughout the fridge can be quite small, including one with a built in impedance to increase the incoming helium pressure which aids in condensation process. If any other gas (most likely nitrogen or oxygen from the atmosphere) were to contaminate the ^{3}He-^{4}He mix it would freeze to the walls of these tiny pipes, eventually blocking the flow completely. In order to prevent this, two levels of 'filters' are used to clean the mix. The first defense is a liquid nitrogen cold trap at 77 K which condenses out any nitrogen or oxygen that might have leaked into the system. This will remove most of the contaminates but a second level of filtering is done using a liquid ^{4}He cold trap which is at 4.2 K. This will guarantee that only a pure ^{3}He-^{4}He mixture will enter the fridge.

5. *1K pot.* The purpose of the 1K pot is to cool the returning ^{3}He to about 1 K (as the name might suggest). This is done via pumping on ^{4}He, driving a liquid-vapor phase transition which cools the surroundings.

6. *Heat exchangers.* Even though the returning ^{3}He is cooled to about 1 K from the 1K pot, this is still often an order of magnitude hotter than the mix in the mixing chamber. Thus it must be cooled further before re-entering the mixing chamber. An efficient method to do this is by transferring its heat to the ^{3}He dilute phase on its way to the still to be pumped away. All this takes place throughout several heat exchangers, both continuous and step heat exchangers.

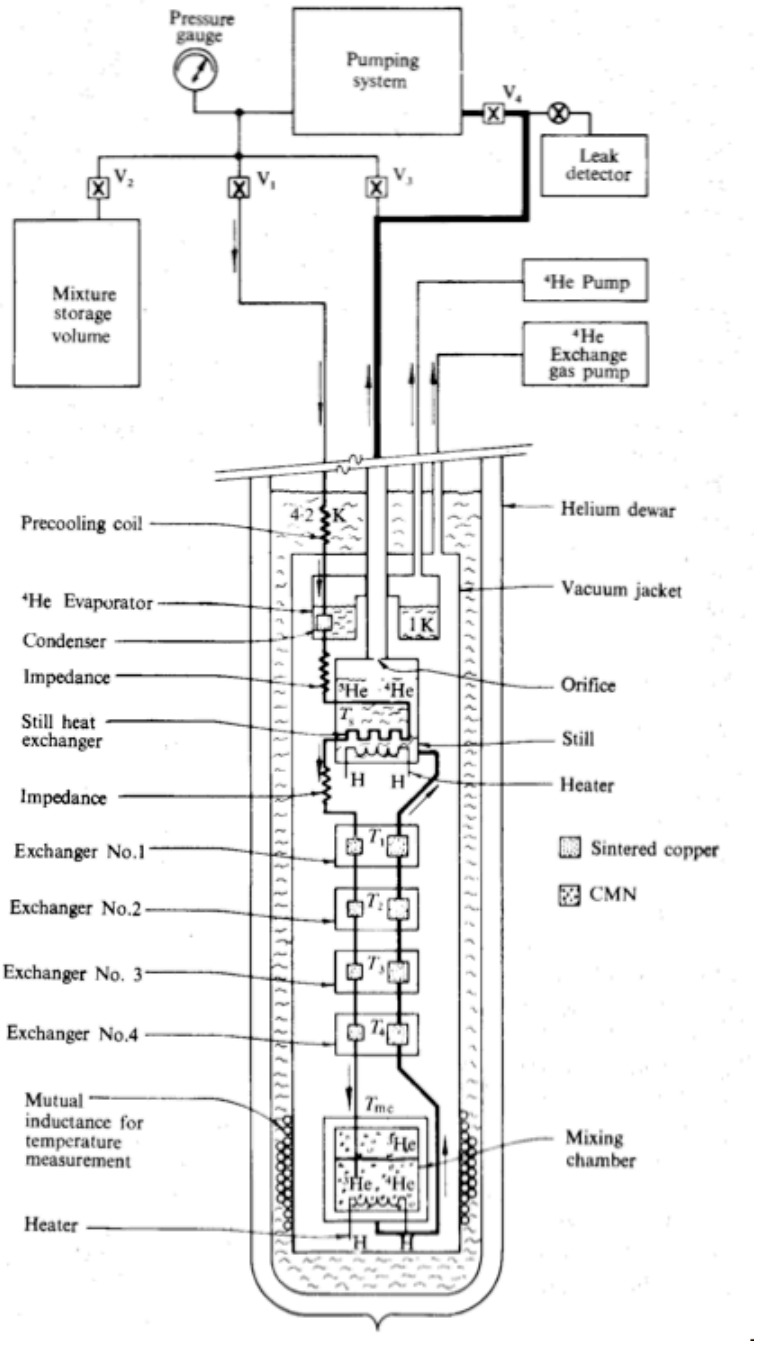

Figure 5.2: Schematic drawing of a Dilution fridge [83].

5.3 Dewar and vibration reduction

The fridge is covered by a radiation shield which is then sealed inside of a vacuum chamber. This whole assembly is then submerged in a liquid ^{4}He bath, the inner chamber in the dewar. The dewar also contains a nitrogen jacket which surrounds the inner helium bath, separated by a vacuum. The helium bath is the ^{4}He source for the 1K pot and it is also where the superconducting magnet is located. The nitrogen jacket provides a layer of insulation for the helium bath from ambient room temperature, which minimizes liquid helium boil off.

Low temperature experiments are often extremely sensitive to vibrations, especially thermal conductivity. Therefore, many precautions must be taken to reduce the vibrations felt by the experiment. This is achieved by suspending the dewar from large wooden beams, made from Canadian maple, which is supported on either side by 8000 lbs of concrete. The concrete pillars extend out of a larger slab of concrete containing a 6' deep pit. This entire structure is isolated from the buildings foundation which separates it from the vibrations in the building. Space was left between the top of the pillars and the wooden beam for the addition of an air spring if so desired in the future as an additional vibration damping mechanism.

Chapter 6

Thermal Conductivity Measurement

6.1 Measurement Technique

As we have seen in chapter 2 the thermal conductivity, κ, is defined as the ratio of the applied heat to the temperature gradient across a sample. In practice this is done by attaching one end of the sample to the fridge and the other to a resistive heater. The applied heat is known because a known current is passed through the resistive heater. Two thermometers then measure the temperature at two points on the sample at a known distance apart, d. The thermal conductivity can then be calculated via:

$$\kappa = -\frac{Q}{T_{cold} - T_{hot}} \cdot geom \tag{6.1}$$

where $geom = d/A$ is the geometric factor.

Figure 6.1 shows a schematic of the one-heater-two-thermometer method used to measure thermal conductivity. The resistive thermometers are uncalibrated and are calibrated in situ against the fridge temperature every temperature sweep. This is done while the heat is off so the thermometers are in thermal equilibrium with the fridge. The sample heater is then turned on to initialize a temperature gradient across the sample. A typical calibration curve for both the cold and hot thermometers is seen in figure 6.2. The heat off points are fitted with a polynomial (usually 3rd order) over a floating window of points (of about 20 points). Figure 6.2 also shows the error in this fit by plotting the residual of the data and the curve. The resistance values of the heat on points are then compared to the calibrated curve to extract the corresponding temperatures.

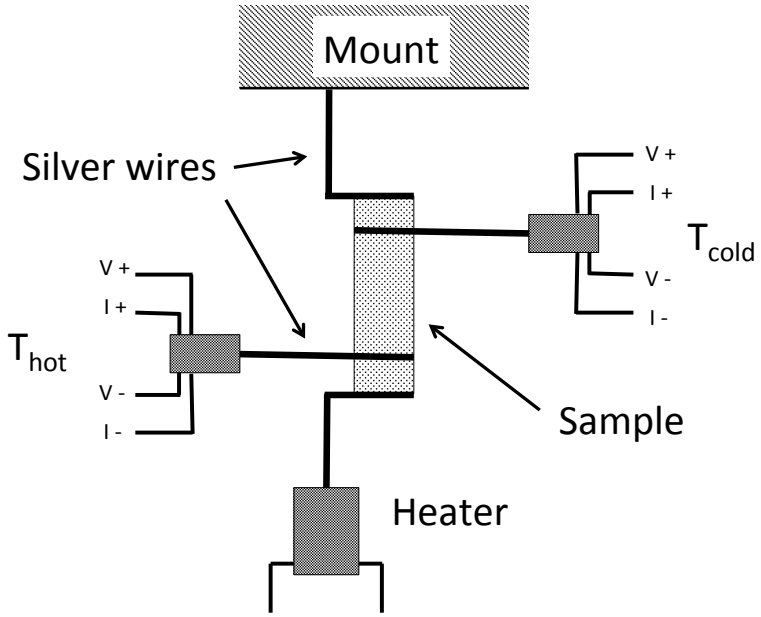

Figure 6.1: Schematic drawing of a thermal conductivity measurement.

6.2 Thermal Conductivity Device

The steady state, one-heater-two-thermometer method for measuring thermal conductivity is quite simple in theory - a known amount of heat is applied at one end of the sample and two thermometers measure the subsequent temperature gradient. The thermal conductivity is then obtained via Fourier's law of heat conduction,

$$\dot{Q} = \kappa \Delta T \frac{A}{l} \tag{6.2}$$

where $\dot{Q}$ is the supplied heat, κ is the thermal conductivity, ΔT is the temperature gradient, A is the cross sectional area and l is the sample length. However, in practice complications arise due to the extreme low temperatures at which these measurements are made and size constraints set by the bore of the superconducting magnet in which the experiment sits. Three of the main obstacles that must be overcome are as follows.

1. Thermally isolating the heater and two thermometers from the mount and the rest of

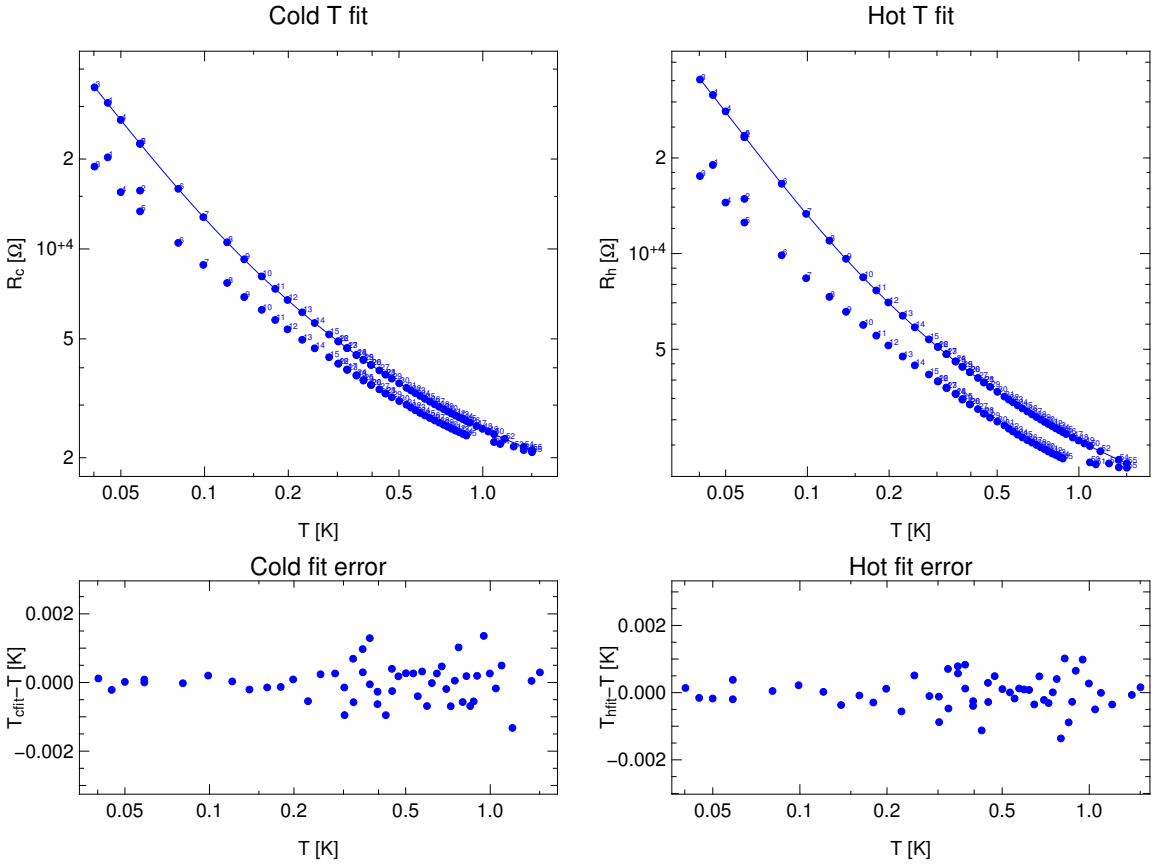

Figure 6.2: Calibration curves for both the cold and hot thermometers for a thermal conductivity measurement. The heat off points are fitted with a polynomial with the residual plotted below. The heat on resistance values are interpolated to the calibrated curve to extract their corresponding temperatures.

the cryostat yet remaining in good thermal contact with the sample, hence insuring all the heat flows through the sample.

2. Minimizing the noise which in the measurement which can be caused by either electromagnetic interference (EMI) in the measurement circuit or from temperature fluctuations in the resistive thermometers or in the fridge temperature.

3. Finally, handling the many wires needed to perform these measurements in a way that minimizes noise and is mechanically robust.

In the following sections, we discuss how to address these issues and provide a quantitative assessment of performance.

6.2.1 Constructing the Heater and Thermometers

The thermometers are fabricated in such a way as to maximize the thermal link between each thermometer and the sample, and to thermally isolate the thermometers from the rest of the mount yet remaining electrically connected.

The concern about thermal isolation of the thermometers is approached by comparing the various thermal resistances in the system. Each thermometer is suspended from a single filament from a strand of dental floss (nylon) or Kevlar with a width of about $10\mu m$ spanning about $1cm$ to either end of the thermal conductivity mount, resulting in a thermal resistance of $w_{nylon} = \frac{l}{A}\frac{1}{\kappa_{nylon}} = \frac{1\text{cm}}{\pi(10\mu\text{m})^2}\frac{1}{0.25\text{W/Km}} = 1.27\cdot 10^{10}\text{K/W}$. Platinum tungsten (Pt 92% / W 8%) wires with electrical resistivity $\rho_{PtW} = 62\mu\Omega\text{cm}$ are used as the electrical connections for the resistance measurement of each thermometer. The thermal resistance of these wires is related to the electrical resistance through the Wiedemann-Franz Law (WFL) using the Sommerfeld value of the Lorenz number L_0.

$$\frac{\kappa}{\sigma T} = L_0 = 2.44 \cdot 10^{-8} W\Omega/K \tag{6.3}$$

Thus, $7.8cm$ of $25\mu m$ thick wire is tightly wound into coils in order to satisfy the size constraints imposed by the dimensions of the thermal conductivity mount. This results in a resistance of $R_{PtW} = 99.1\Omega$ and a thermal resistance of $w_{PtW}(300\text{K}) = \frac{R_{PtW}}{L_0 T} = 1.37\cdot 10^7\text{K/W}$. Therefore, the total thermal resistance to the cold bath is $w_{total} = (2\frac{1}{w_{nylon}} + 3\frac{1}{w_{PtW}})^{-1} = 4.56 \cdot 10^6\text{K/W}$ since the nylon extends out both ways from the thermometer and there is one coil coming from each of the thermometer leads and an additional coil from the sample resistance voltage lead. The thermal resistance between the sample and the thermometer is limited to a short length of silver wire and the contact resistance to the sample which is used as both the thermal link between the sample and the thermometer and also as the V+ (V-) voltage lead for the sample resistivity measurement. The silver wire is about 8mm long and 50μm in diameter with a resistivity of $\rho_{Ag} = 1.6\mu\Omega\text{cm}$ and thus has a resistance of $R_{Ag}(300\text{K}) = 65\text{m}\Omega$. The contact to the sample is comprised of silver paste and contributes a resistance on the order of a few milli-Ohms. Whence, the thermal resistance to the sample is $w_{total} \approx 9.6 \cdot 10^3\text{K/W}$ which is 0.2% of the thermal resistance to the cold bath. In fact, it is much better than this at low temperatures. Silver has a residual resistivity ratio of about 100, thus at 4 K the resistivity decreases by a factor

of 100. So the resistance of the silver wire at 4 K is only $R_{Ag} = 0.65\text{m}\Omega$. The resistance imparted by the sample contacts at low temperature, will often be the limiting factor of the thermal resistance from the to the sample as it will remain a few milli-Ohms. Thus extreme precautions are taken to ensure minimal contact resistance to the sample. As for the thermal resistance to the cold bath at low temperature, the resistance of the PtW wire will reduce as temperature is decreased, lowering its thermal resistance. However, since PtW is an alloy, its RRR will be much lower than for pure metals like Ag, so the resistance does not decrease as much as for Ag. That is, even though the thermal resistance to the cold bath decreases with temperature, it remains much higher than the thermal resistance to the sample. Therefore the heat loss to the sample mount is minimal, especially at low temperatures.

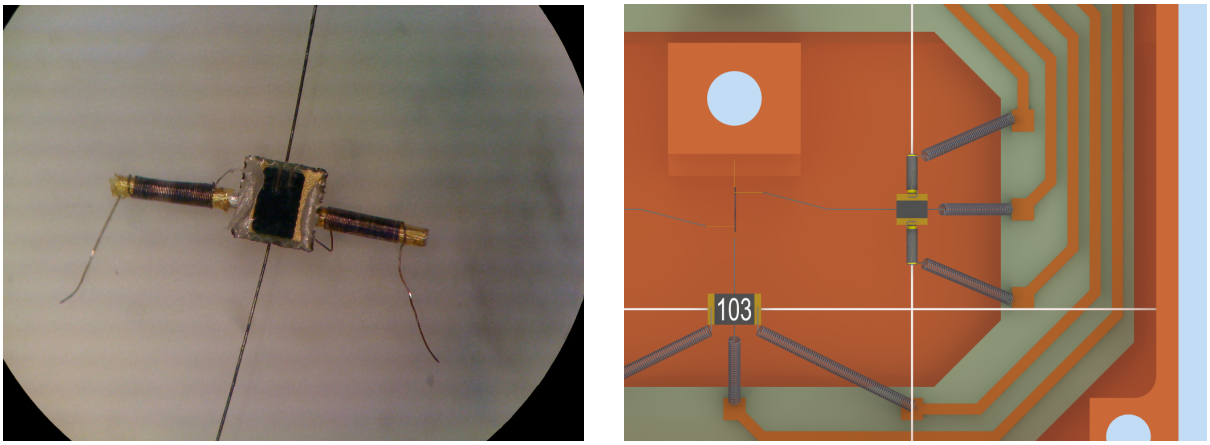

Figure 6.3: A digital image (left) of a thermometer prior to affixing PtW wires to the end of the Ag wires coiled around the Ag rod. A computer rendered image (right) of a sample thermometer and he heater mounted on a nylon filament.

In order to ensure a good thermal link from the thermometer to the sample the substrate on which the RuO_2 resistive thermometer is mounted is thinned from 800μm to about 300μm. A 300μm silver wire rod is wrapped in a layer of 7μm Kapton film (from DuPont) and subsequently a 25μm silver wire is coiled onto the rod. This rod is affixed to the back of the thermometer and the coiled wires are connected to the resistor contacts using silver epoxy since this will provide the best thermal connection to the thermometer. the PtW wire coils are attached to the opposite ends of the silver wire coils. The 25μm silver wire which connects to the sample is also affixed to the back of the thermometer using silver epoxy. An image of a completed thermometer is seen on the left in FIG. 6.3.

A similar approach is taken when addressing the thermal isolation of the sample heater.

It is imperative that all the heat produced by the resistive heater travel through the sample to the cold bath since it is crucial to know the the amount of heat put into the system when measuring the thermal conductivity. In this case a 50μm silver wire is affixed to the back of a 10 kΩ metallic resistor which is used as both the thermal link to the sample and the I+ current lead used in the 4 wire sample resistivity measurement.

6.2.2 RF Shielding and Noise Reduction

When operating in the tens of milli-Kelvin regime, even small amounts of heating will have a large effect. For example, to induce a temperature gradient of $\Delta T/T = 10\%$ at $50mK$, the heat required from the sample heater is on the order of $0.1nW$. Hence, extreme care must be taken in minimizing unwanted sources of heat, in particular, RF pickup in the electrical circuits.

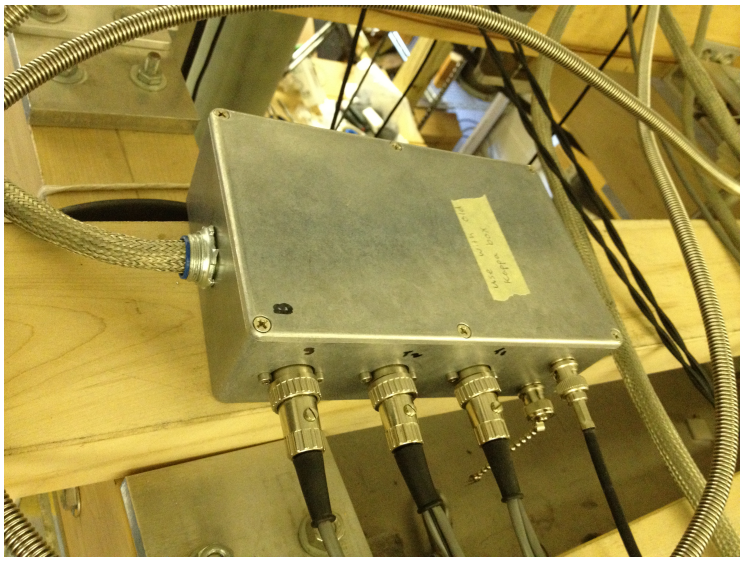

Figure 6.4: Shielded breakout box at the top of the dilution fridge routing the 24 wire cable through several low pass filters then on to three 5 pin bayonet connectors and 2 BNC connectors.

The two routes to minimizing RF noise are (a) proper shielding and filtering of the room temperature wires at the top of the cryostat and (b) shielding of the experiment mounted on the fridge. A low voltage Fischer connector is used at the top of the fridge. The cable directly enters a RF shielded box (figure 6.4) where the signal is filtered using multiple low pass filters which removes any high frequency noise. This box is also used to

separate each of the signals from each thermometer and the sample resistance to a 5-pin bayonet connector used by the LR-700 resistance bridge multiplexer. The current leads for the sample heater is also located on this box as a pair of BNC connectors. The shielded box is then grounded to the fridge. This provides excellent shielding from RF noise outside the cryostat. To effectively shield the experiment from EMI locally on the cryostat, the entire thermal conductivity measurement is built inside of a copper box (FIG. 6.6).

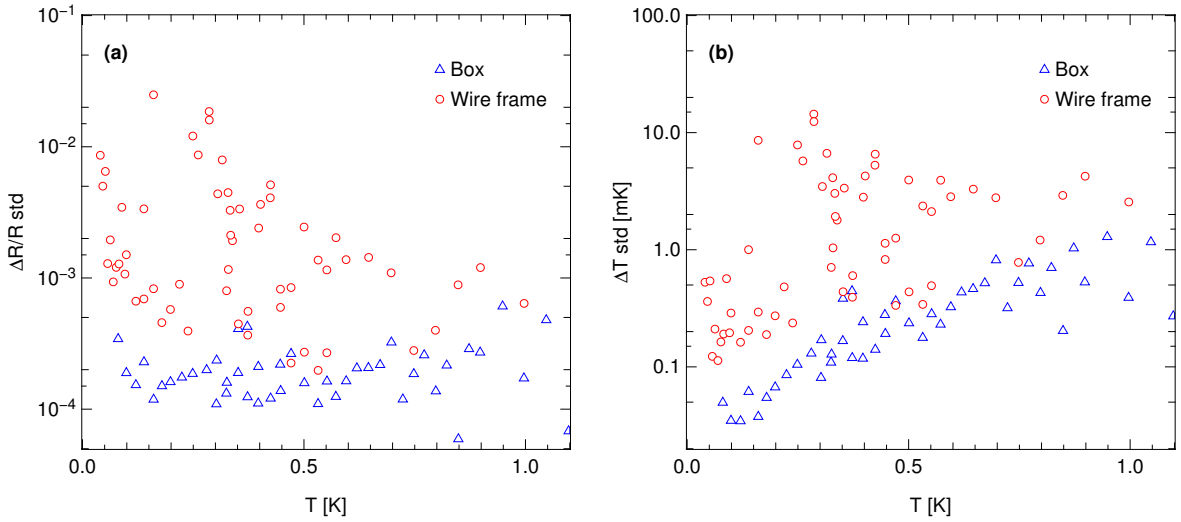

Figure 6.5: **(a)** Standard deviation of the measured resistances normalized by the resistance for sample thermometers mounted on a wire frame (red circles) and in a copper box (blue triangles). **(b)** Standard deviation of the temperatures corresponding to the resistances from sample thermometers.

FIG. 6.5 (a) shows the normalized standard deviation of the resistance values from thermometers mounted on both an open wire frame and in a copper box. It is clear that the standard deviation is up to 2 orders of magnitude lower for the thermometer in the box than on the wire frame. This is clear evidence that the noise due to electromagnetic interference (EMI) is much lower in the copper box. FIG. 6.5 (b) shows the standard deviation of the resistances of the thermometers converted to temperatures which further confirms that the noise in the thermometer in the box is much lower than on the wire frame.

Proper treatment of the grounded sheath surrounding the wires is essential. The entire system must be grounded through a single point and branch out from there to ensure that every grounded sheath and grounded box are at the same potential as the ground. This is done to eliminate ground loops, which arise when two or more points in the system that

should be at the same potential, are not, often because they are grounded through two different paths (ie. through a water pipe and through the grounding spike in the pit). This causes a small current to run through the grounded sheath which is a major cause of noise and interference in the circuit. Improper grounding can be a serious problem when trying to achieve the lowest base temperature possible and thus should be addressed accordingly.

Computers are inherently electrically noisy machines. However, they are needed to run the experiment and acquire data. Thus it is important to electrically isolate the computer from the rest of the scientific equipment such as the resistance bridge used in measuring the sample thermometers. This is done via optical isolation. The electrical signal from resistance bridge is converted to an optical signal, which is transmitted through a fiber optic cable and is then converted back to an electrical signal to be acquired by the computer. Essentially, optically isolating the computer from the measurement equipment will only allow the transmission of the desired signal between the two, isolating the noise associated with the computer.

Johnson-Nyquist Noise

It is worth noting that even with all these noise reducing precautions, there is a minimum limit to the electrical noise in a resistance measurement regardless of the applied voltage. This noise is due to the thermal agitation of the electrons and is called the "Johnson-Nyquist noise" as it was first measured by J. B. Johnson in 1926 and described by H. Nyquist. We are able to measure the Johnson-Nyquist noise in our sample thermometers because of the high quality resistance bridge used (Linear Research LR-700), and thus it provides a good test to see if all other sources of noise have successfully been removed from the system. The minimum variance in the voltage, $\overline{v}$, per Hertz of bandwidth is given by:

$$\overline{v}^2 = 4k_B T R \tag{6.4}$$

where k_B is Boltzmann's constant, T is the temperature and R is the resistance. It is often more useful to talk about the root-mean-square (RMS) of the voltage which can be written as:

$$v_{RMS} = \sqrt{4k_B T R \Delta f} \tag{6.5}$$

where Δf is the frequency bandwidth. For example, the voltage RMS of a 1 kΩ resistor at 300 K will be equal to 4.07 nV/$\sqrt{\text{Hz}}$. Applying this to our system, a 3 second digital filter is used on the LR-700 resistance bridge, which equates to a bandwidth of 0.053 Hz. We are also able to set the excitation voltage, V, used to measure the resistance. So, the

RMS of the resistance value at 300 K is:

$$R_{RMS} = 0.03 \frac{R^{3/2}}{V} \text{ n}\Omega \tag{6.6}$$

Now, because we are assuming that the noise takes on a Gaussian probability density function, we know that 98.7% of the noise will be within 5 standard deviations and thus the peak-to-peak noise amplitude is equal to 5 times the RMS value. Thus, a 1 kΩ resistor with an excitation voltage of 300 μV will have a peak-to-peak Johnson-Nyquist noise of about 3 mΩ.

6.2.3 Mechanical Stability

The usefulness of a device is often closely related to its longevity. The two areas that must be addressed are the treatment of the 14 wires (4 wires for the hot thermometer, 4 wires for the cold thermometer, 2 wires for the heater and 4 wires for the sample resistance) needed to perform a thermal conductivity measurement and the protection of the delicately balanced thermometers, heater and sample.

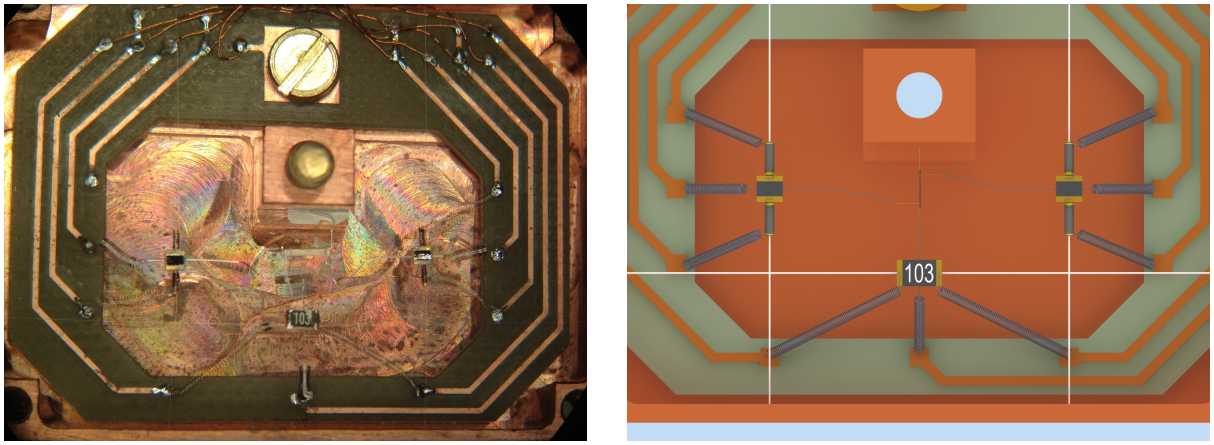

Figure 6.6: A digital image (left) and a computer rendered image (right) of the printed circuit board with both thermometers and heater mounted and soldered to the PCB.

The coils from the thermometers and the heater are soldered directly to a printed circuit board (PCB) which collects all the leads together at one end of the mount. A PCB is used because it is the most efficient and orderly method of handling the leads from the thermometers and heater while preventing any damage of the wires and conforming to the strict size constraints.

A ribbon cable (product code: A8-311 from Oxford Instruments) comprised of 12 twisted pairs is soldered to the PCB. Twisted pairs are used because they minimize noise caused by electromagnetic interference, and cross-talk from neighbouring wires. The ribbon cable is also affixed to the mount with a small about of epoxy resulting in a sturdy joint between the two. The ribbon cable is a prime candidate for handling many small wires while maintaining mechanical stability since any strain on the cable is managed by the cotton ribbon and the wires are left unharmed. The other end of the ribbon cable is soldered into a micro-D connector (part number: MDM-25 SSB from ITT Cannon). A block of epoxy (STYCAST 2850FT Black from Emerson & Cumings) is then cast on the back of the micro-D connector to minimize the chance of breaking wires and to maximize the overall strength of the cable-connector junction. An image of the completed box and cable assembly is seen in FIG. 6.7.

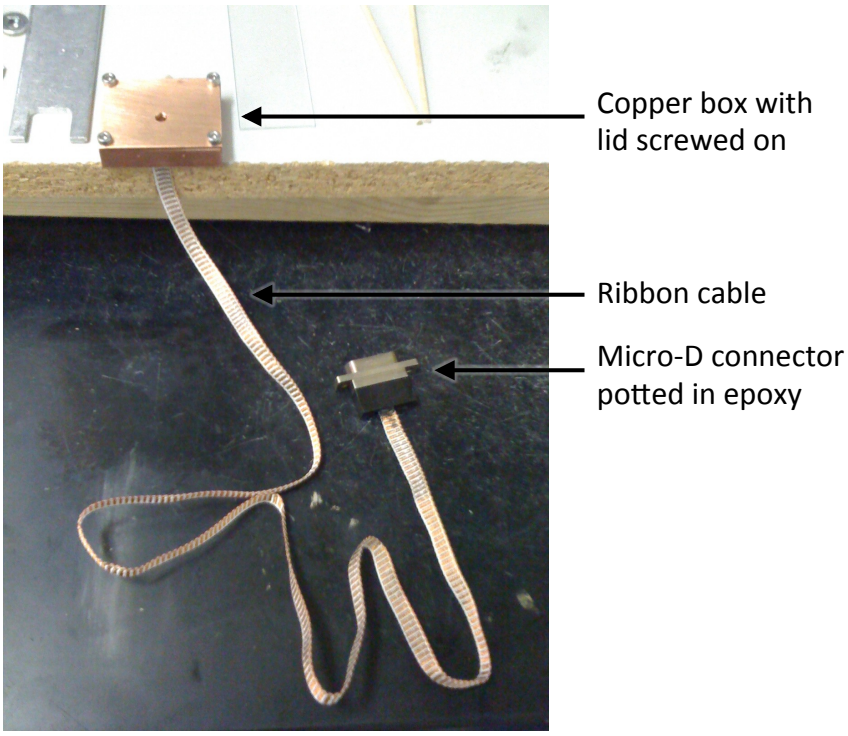

Figure 6.7: Completed thermal conductivity box with the lid screwed on and the 12 twisted pair ribbon cable stemming out the bottom terminating at the epoxied micro-D connector.

It is also very important and practical to protect the thermometers, heater and sample from damage due to external circumstances (for example, getting bumped while putting

the radiation shield on the fridge). In order to attain this protection, the sample mount is built directly into a small copper box which is made to house the entire PCB assembly. This box also acts as a local electromagnetic interference (EMI) shield as previously stated.

6.2.4 Mounting the device on the fridge

A copper plate is secured to the bottom of the mixing chamber, so they will be at the same temperature. This plate has a number of tapped holes for the purpose of mounting experiments and thermometers. Since this plate is directly attached to the mixing chamber, it is well outside of the superconducting coils, where the high magnetic fields are generated. Thus, if we wish to subject our sample to an external applied magnetic field, the experiment must be mounted to the end of a silver extension known as the 'tail'. Silver is used because it has a low thermal resistance at low temperatures, and does not have a large nuclear component to the specific heat in field like copper does. The tail itself is about 30 cm long, with several mounting positions at the lower end to ensure that the sample is located directly in the magnetic field.

Part III

Experimental Results

Chapter 7

LaFePO

7.1 Introduction

In conventional superconductors the pairing mechanism is phonon mediated and the superconducting gap function is known to have a fully gapped, s-wave symmetry. The high-T_c cuprate superconductors, although not fully understood are known to have a d-wave superconducting gap and are thought to have a pairing mechanism which is magnetic in origin. However, in the iron based superconductors the superconducting gap function is still unknown and is the center of much debate. It is worth noting that the d-wave symmetry is seen in all of the cuprates, whereas the symmetry of the order parameter may not be the same in all of the iron based superconductors, although they may share a common pairing mechanism. Knowledge of the superconducting gap is extremely useful due to its connection with the pairing mechanism. It doesn't appear that the electrons are paired via a phonon interaction due to a weak electron-phonon interaction [4]. In addition to potentially having a pairing mechanism which is magnetic in nature [84], it has also been shown that LaFePO has a multiband Fermi-surface. This leads to the possibility of a wide variety of superconducting gaps symmetries across the multiple Fermi surfaces. Many of these gaps have also been shown to lay very close in energy [39], and thus we must make very careful measurements to distinguish between them.

Previous thermal conductivity measurements of LaFePO have been conducted by Yamashita *et al.* at temperatures down to 460 mK in fields parallel to both the c direction and the ab planar direction [85]. However, this study does not go to low enough temperatures to accurately extract the linear electronic term of the thermal conductivity by extrapolating to $T = 0$ K. Therefore, our study provides a much more rigorous examina-

tion of the residual electronic contribution to the thermal conductivity as we go an order of magnitude lower in temperature, reaching 40 mK.

7.2 Experimental details

This study focuses on the iron based superconductor LaFePO with $T_c \sim 7.5$ K and a reported $H_{c2} \sim 900$ mT from previous transport measurements [85]. The LaFePO sample we measured was a small, single-crystal platelet of dimensions 200 μm x 50 μm x 20 μm grown using the Sn flux method [86]. Electrical resistivity measurements verified the high quality of the sample which revealed a residual resistivity ratio (RRR) of $\rho_{300\mathrm{K}}/\rho_{0\mathrm{K}} = 65$ with $\rho_0 = 2.4\mu\Omega$cm. This was measured by suppressing superconductivity with $H = 2$ T applied along the c-axis.

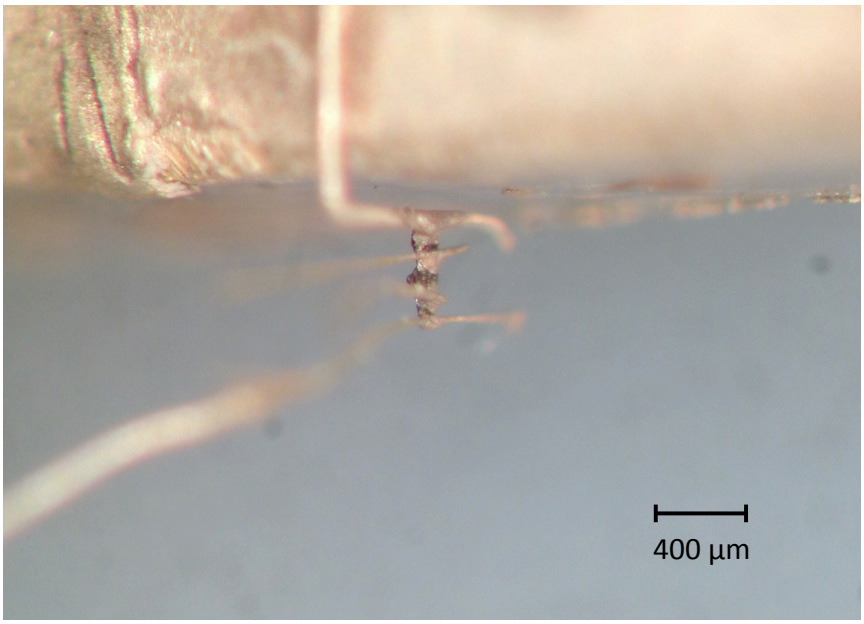

Figure 7.1: Digital image of the LaFePO sample.

It is essential that the sample contacts have a very low thermal (and electrical) resistance when measuring thermal conductivity for $T < 1$ K, as the electric and phonon degrees of freedom can decouple, potentially leading to an underestimation of κ_e [87]. Low resistance thermal contacts were prepared on the sample by initially etching the crystal surface with Ar and then sputtering Pt contacts. Gold wires were then bonded to these pads with silver

epoxy. The electrical resistance of the contacts is less than 1 Ωm at low temperatures, and thus also have a low thermal resistance.

Thermal conductivity measurements were made using the one-heater-two thermometer method as described in chapter 6 at temperatures down to 40 mK in the ab-plane and in applied magnetic fields up to 5 T parallel to the c-axis. The application of a magnetic field allows us to accurately separate the electronic (κ_e) and lattice (κ_{ph}) contributions. Field-cooling the samples is done to ensure homogeneous flux penetration. This entails cycling to temperatures greater than T_c before changing the field. The absolute error in the conductivity is approximately 10% due to uncertainties in the geometric factor ($length/area$) of the sample. However, the relative error between the various temperature sweeps is lower, on the order of 3%.

7.3 Results and discussion

Recall that the specific heat can be written in general as $c_v/T = \gamma + \beta T^2$ where γ is the electronic contribution and βT^2 is the phonon contribution and thus the total thermal conductivity can be written as $\kappa/T = A + BT^2$ since $\kappa = c_v v l/3$ from kinetic theory. So, the intercept of a plot of κ/T versus T will directly give us the electronic term of the thermal conductivity, A, by extrapolating to $T = 0$ K, and the phonon term, B, by fitting the temperature dependence to a quadratic. So, thermal conductivity divided by temperature is plotted versus temperature in figure 7.3. The zero field temperature dependence of κ/T is much stronger than in the in field data. This large zero field temperature dependence is quickly suppressed in an applied field of 20 mT (figure 7.3). Similar behaviour is also seen in the cuprate [29] and the filled skutterudite [88] superconductors (figure 7.2). Above this field, the temperature dependence reduces in magnitude and become equivalent between field strengths. Thus the temperature dependence in the 20 mT data is likely to be entirely due to phonons which are assumed to be field independent. We can then fit the observed phonon conductivity with a quadratic, which results in $\kappa_{ph}/T = \kappa(20\text{mT})/T - \kappa_o(20\text{mT})/T = 1.2T^2$ mW/K^{4}cm. The phonon conductivity can also be calculated using kinetic theory which states $\kappa_{ph} = \frac{1}{3}\beta T^3 v_s l_{ph}$ where $\beta = 0.16$ mJ/K^{4}mole is the coefficient of the phonon specific heat [89], $v_s = 6263$ m/s is the speed of sound which is estimated from the Debye temperature, $\Theta_D = 371$ K and $l_{ph} = \sqrt{4ab/\pi} = 2.7 \cdot 10^{-5}$ is the average sample dimensions. Thus the phonon conductivity divided by temperature is calculated to be $1T^2$ which is very close to the observed conductivity, and can be seen in figure 7.4.

Now the electronic component of the 0 T conductivity can be easily separated from

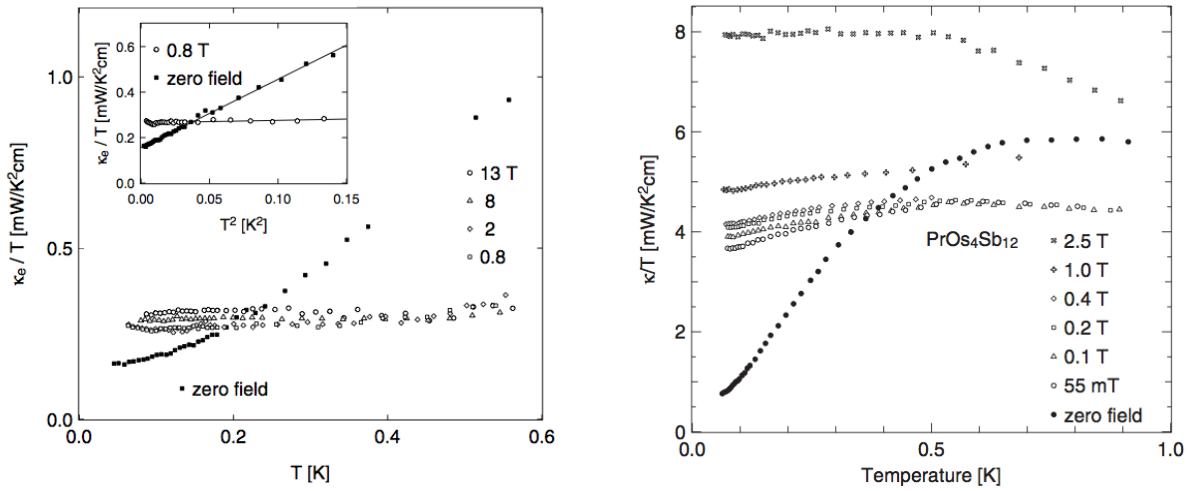

Figure 7.2: Electronic thermal conductivity of the high-T_c cuprate superconductor $YBa_2Cu_3O_7$ [29] (left) and of the filled-skutterudite superconductor $PrOs_4Sb_{12}$ [88] (right). Both materials show a rapid suppression of the temperature dependence with the applications of a magnetic field.

the phonon conductivity via $\kappa_e(0\text{T})/T = \kappa(0\text{T})/T - \kappa_{ph}/T$. Figure 7.4 shows $\kappa_e(0\text{T})/T$ is plotted versus T as well as the calculated and measured phonon contribution. The linear term in the electronic thermal conductivity is found by extrapolating κ_e/T to $T = 0$, resulting in a residual conductivity of $\kappa_0/T = 3.0 \pm 0.3$ mW/K^2cm. This can be interpreted as a non-zero electronic density of states as $T \to 0$ K. Superconductivity can be effectively suppressed in an applied magnetic field of 700 mT which will give us the normal state residual thermal conductivity $\kappa_o(700\text{mT})/T = 9.6 \pm 0.3$ mW/K^2cm. Therefore, the zero field residual thermal conductivity is a substantial fraction (0.31) of the normal state residual conductivity. This provides compelling evidence that the non-zero electronic conductivity is imposed by a nodal superconducting symmetry rather than by disorder. The inset of figure 7.3 shows the thermal conductivity and electrical resistivity in thermal units in an applied field of 2 T. The fact that they are co-linear illustrates the verification of the Wiedemann-Franz law, confirming that superconductivity is fully suppressed and the sample is int he normal state.

We are now able to compare the magnitude and temperature dependence of $\kappa_e(0\text{T})$ to several current theoretical models of the superconducting gap, namely, fully gapped $s\pm$, nodal $s\pm$ and d-wave symmetries [46, 90].

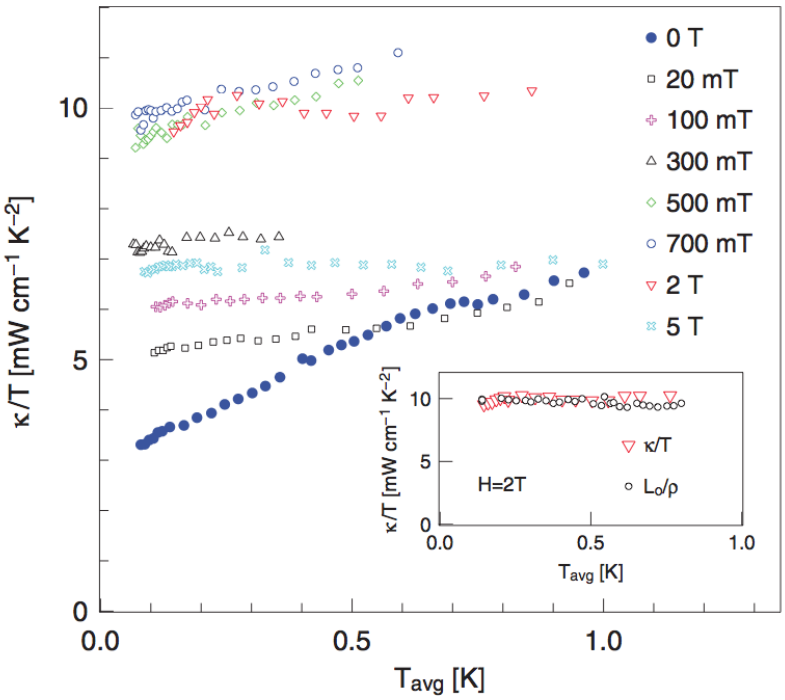

Figure 7.3: Thermal conductivity of LaFePO in applied magnetic fields between 0 T and 5 T. *Inset:* 2 T thermal conductivity divided by temperature lies directly on top of the electrical resistivity in thermal units (L_0/ρ) indicating that the WFL is obeyed. This shows that superconductivity is fully suppressed in a field of 2 T.

7.3.1 Fully gapped $s\pm$ symmetry

In a single band, isotropic s-wave superconducting gap, one expects the linear electronic term to tend to zero as the temperature approaches absolute zero because the electronic quasi-particle excitations are exponentially suppressed as $T \to 0$. However, in the multi-band $s\pm$ model, where the isotropic gaps on each band can lead to interband scattering resulting in a small finite density of states at low temperatures [46]. The ratio of the residual conductivity to the normal state residual conductivity is usually on the order of 1% which is much lower than the 31% we observed in our data. Therefore, the fully gapped $s\pm$ model is inconsistent with our data.

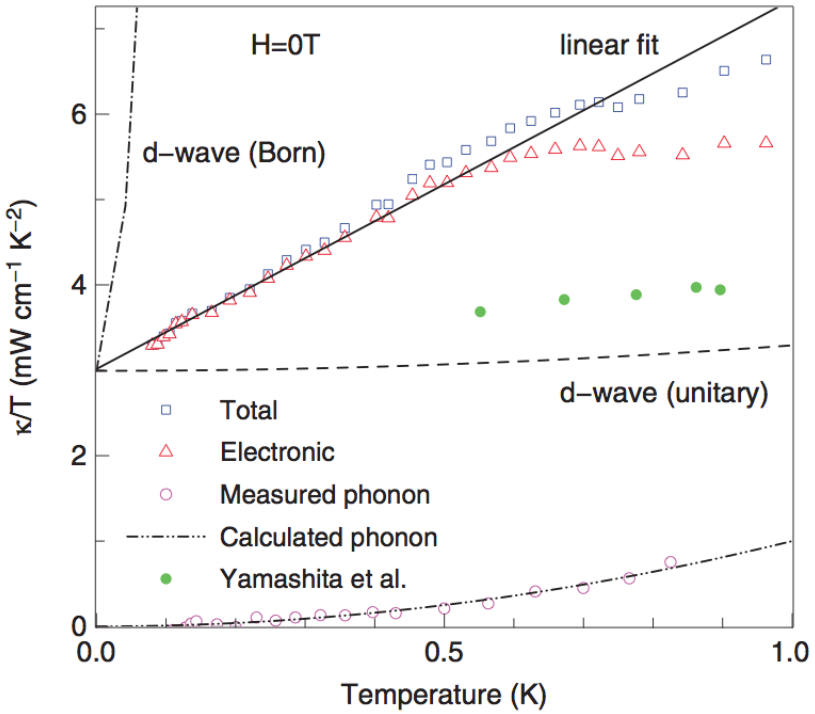

Figure 7.4: Zero field thermal conductivity divided by temperature vs. temperature of LaFePO along with data taken by Yamashita *et al.* [85] in comparison with the d-wave predictions in the Born and unitary limits. Both the measured and calculated phonon contribution are plotted as well.

7.3.2 Nodal $s\pm$ symmetry

We have already stated that the pairing mechanism is not phonon mediated due to a weak phonon-electron interaction which leaves the possibility of a magnetic pairing mechanism. Depending on the exact details of the magnetic fluctuations, the superconducting gap can become anisotropic, with the appearance of deep minima or even a sign changing node on one of the Fermi-surfaces. Many transport models which have been reported treat the Fermi-surface as a two band model with an isotropic electron pocket at the Gamma point with the anisotropy appearing on the hole pocket at the M point.

As in the case of a d-wave superconductor, $s\pm$ has a nodal superconducting gap which in the presence of impurity pair breaking leads to quasiparticle excitations which result in a residual linear electronic term to the thermal conductivity in the superconducting state.

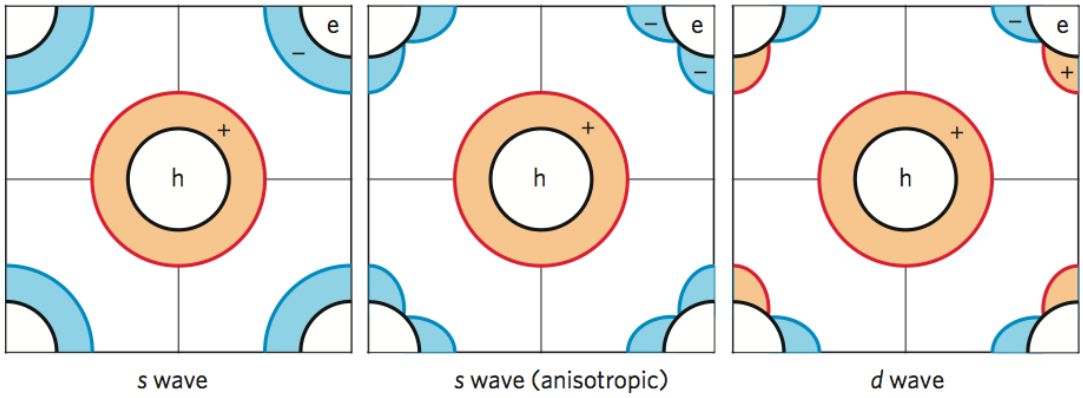

Figure 7.5: Possible order parameters projected onto the $(\mathbf{k}_x, \mathbf{k}_y)$ plane [32]. Accidental nodes can appear in the anisotropic s-wave case given that it does not break the four-fold rotational symmetry. However, in the d-wave scenario, the nodes are imposed by a change in sign of the superconducting gap. A rotation of the d-wave by $\pi/2$ does not return itself, that is, it violates the four-fold rotational symmetry [91].

However, one of the main differences between d-wave and nodal $s\pm$ symmetries is that the magnitude of κ_e/T is universal in the d-wave case with respect to the normal state scattering rate whereas κ_e/T is extremely dependent on scattering rate for the $s\pm$ case as seen in calculations from Mishra *et al.* [92].

In order to observe the effect of the scattering rate on the electronic thermal conductivity, we must first calculate the normal state scattering rate. We can estimate the scattering rate two different ways, directly from the measured normal state conductivity via kinetic theory and from de Haas-van Alphen measurements of the electron mean free path l_0. The first method uses kinetic theory which states $\kappa_e(N)/T = \gamma v_F^2 \tau/3$ where the scattering rate is defined as $\Gamma = 1/2\tau$. The electronic specific heat has been measured by two groups and found that $c_v/T = \gamma = 11.5$ mJ/K^{2}mole [89, 93]. The Fermi velocity has also been measured via ARPES measurements resulting in $v_F \approx 1.5 \cdot 10^5$ m/s [36]. Thus the scattering rate is $\Gamma = 1.1 \cdot 10^{12}$ s^{-1}, or in reduced units with respect to T_c gives $\hbar\Gamma/k_B T_c = 1.1$. Using the second method, we see that de Haas-van Alphen measurements give an electron mean free path of $l_0 = 1000\mathring{A}$ [86]. Thus the relaxation time is $\tau = l_0/v_F \approx 10^{-13}$ s resulting in a reduced scattering rate on the order of $\hbar\Gamma/k_B T_c \sim 0.8$, which is consistent with the first method. Other iron based superconductors have been observed to have similar large scattering rates with $\hbar\Gamma/k_B T_c \sim 1 \rightarrow 2$ [41, 94, 95].

A scattering rate of this magnitude is expected to substantially suppress T_c for a d-

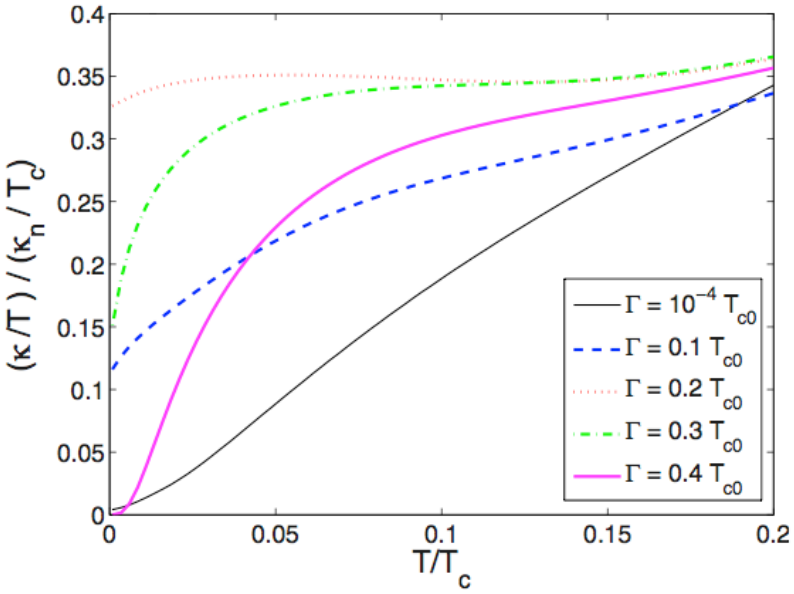

Figure 7.6: Normalized thermal conductivity versus temperature of the anisotropic s-wave model for varying interband scattering rates, Γ [92].

wave superconductor. This is not the case in LaFePO. It has been shown that even raising ρ_0 by a factor of 5 does not noticeably effect T_c [96]. This is consistent with current theoretical models describing nodal $s\pm$ symmetry which suggest that the nodes can be lifted by disorder leading to a disorder induced suppression of T_c. This suppression is much more gradual than described in Abrikosov-Gorkov theory for d-wave superconductivity [46]. Figure 7.7 shows the evolution of the critical temperature with the scattering rate, both normalized by critical temperature in the clean limit, for a number of iron-pnictide superconductors [91]. It shows that superconductivity will be suppressed in these iron-based superconductors when $\Gamma = 45 k_B T_{c0}$. This is approximately 50 times larger than the scattering rate needed to suppress super conductivity is the d-wave superconductors, where the maximum scattering rate is given by $\hbar\Gamma = 0.88 k_B T_{c0}$ [23].

Comparing the deep minima scenario to that of the sign changing nodal $s\pm$ scenario we find that such a large scattering rate can lead to the magnitude of the residual electronic conductivity being a sizable fraction of the normal state conductivity. The temperature dependence of κ_e/T is however expected to be proportional to T up to about $T = 0.2T_c$ in the nodal $s\pm$ scenario which is clearly observable in our data, whereas we would expect a constant temperature dependence for for deep minima case [92].

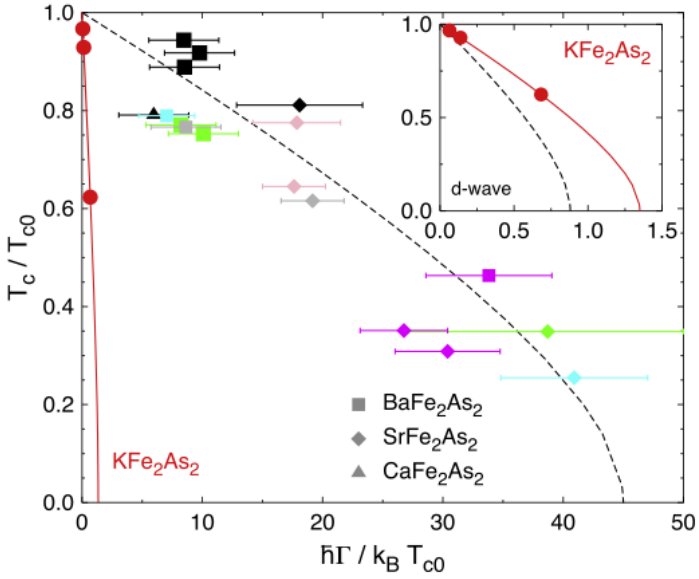

Figure 7.7: The critical temperature normalized by the clean limit, T_c/T_{c0}, is plotted versus the normalized scattering rate, $\hbar\Gamma/k_BT_{c0}$, for a number of different 122 iron-based superconductors [91]. The dashed line shows that superconductivity will be suppressed in these iron-pnictide superconductors when $\hbar\Gamma = 45k_BT_{c0}$. This is in contrast with the d-wave case where superconductivity is suppressed when $\hbar\Gamma = 0.88k_BT_{c0}$ [23] (seen in the inset).

7.3.3 d-wave symmetry

We have seen in section 3.4 that the d-wave symmetry predicts a universal temperature dependence of the electronic thermal conductivity. The second order term depends on the scattering rate, namely the impurity bandwidth γ, and a constant a which is dependent on the scattering strength and is given by [24]

$$\frac{\kappa_e}{T}(T) = \left[\frac{\kappa_0}{T} + \frac{7\pi^2}{15}\left(\frac{a^2T}{\gamma}\right)^2\right] \tag{7.1}$$

We are also able to estimate the first order, residual conductivity via:

$$\frac{\kappa_0}{T} = \left(\frac{4}{\pi}\frac{\hbar\Gamma}{\Delta_0}\frac{1}{\mu}\right)\frac{\kappa_n}{T} \tag{7.2}$$

where Γ is the scattering rate, Δ_0 is the magnitude of the gap and μ is the slope of the gap at a node. We can now compare our results to the d-wave model. If we assume that gap is purely d-wave then we are able to approximate the magnitude of the gap using $\Delta_0 = 2.14 k_B T_c$ and $\mu = 2$ (for a single band d-wave superconductor). Thus d-wave predicts that the universal linear conductivity is $\kappa_0/T = 2.7$ mW/K^{2}cm which is in excellent with our measured value. We can look at the temperature dependence on top of the residual conductivity in both the weak (Born) scattering limit and in the strong (unitary) scattering limit in the case of d-wave symmetry. In the Born limit we use $a = (\pi v_2 \tau_0)/2$ and $\gamma = 4\Delta_0 e^{-\pi\Delta_0/2\Gamma} = 0.1$ K. For the unitary limit, $\gamma = 0.63\sqrt{\Delta_0 \Gamma} = 8.5$ K and $a = 1/2$ [24]. The results from each of these limits can be seen in figure 7.4. Quantitatively, our data lies between both of these limits which suggests that the scattering phase shift is between 0 and 2π which indicates that the acceptable impurity bandwidth is between 0.1 and 8. However, from a qualitative stand point, our data displays a T^2 temperature dependence which is different from the T^3 behavior that d-wave predicts.

We can also look at the sensitivity of κ_e/T to the scattering rate. As we have seen in a d-wave superconductor, the electronic thermal conductivity in the superconducting state should be universal regardless of the scattering rate. This is not the case in $s\pm$, which is theorized to be extremely dependent on scattering rate. Previously reported thermal conductivity measurements on LaFePO stated a normal state conductivity of 6.0 mW/K^{2}cm [85] as opposed to our normal state conductivity of 9.6 mW/K^{2}cm. This suggests that the previously measured sample has a scattering rate 1.6 times larger than our sample. However, both samples displayed a residual electronic conductivity of about 3.0 mW/K^{2}cm. Thus the concept of a universal conductivity as in a d-wave scenario is not ruled out assuming a small error in the absolute magnitude of the measured conductivities and due to a 10% error in the measurement of the geometric factor.

7.3.4 Magnetic field dependence

As we have seen in the theoretical review section, a magnetic field can be used to suppress superconductivity. In addition to this a magnetic field can also provide valuable information about the gap topology by observing the field-induced quasi-particles effect on thermal transport. The inset of figure 7.5 shows the normal state conductivity divided by temperature where superconductivity is fully suppressed with a field of $H = 2$T $\parallel c$. The electrical transport is also represented in the inset, plotted in thermal units (L_0/ρ). The overlap of the two data sets verifies that the Wiedemann-Franz law holds, confirming that the system is in the normal metallic state. The field dependence of the conductivity at intermediate fields ($H < H_{c2}$) provides information on the structure of the gap. Figure 7.8 shows the

conductivity as a function of field for the $T \to 0$ extrapolated values. The $T = 0.46$ K values are also seen in figure 7.8 as a direct comparison to the data of Yamashita *et al.* All three curves are quantitatively consistent such that they all display a rapid increase in conductivity at low fields, at which point the conductivity plateaus before continuing up to the normal state conductivity at $H_{c2} = 700$ mT. This is slightly less than the upper critical field reported by Yamashita *et al.* which stated that $H_{c2} = 900$ mT. The features in the field dependence are most apparent in the $T = 0$ K limit. An applied field of $H = 20$ mT doubles κ_0/T from the $H = 0$ T value. The conductivity continues to increase at a slower rate until $H_{c2} = 700$ mT. The 460 mK data also includes a phonon component and it is clear that at a slightly higher temperature ($T \geq 0.5$ K) the field dependence would be qualitatively different since the initial increase would be no longer present. Thus the $T \to 0$ K extrapolation of the conductivity yields the most reliable field dependence of the electronic thermal conductivity.

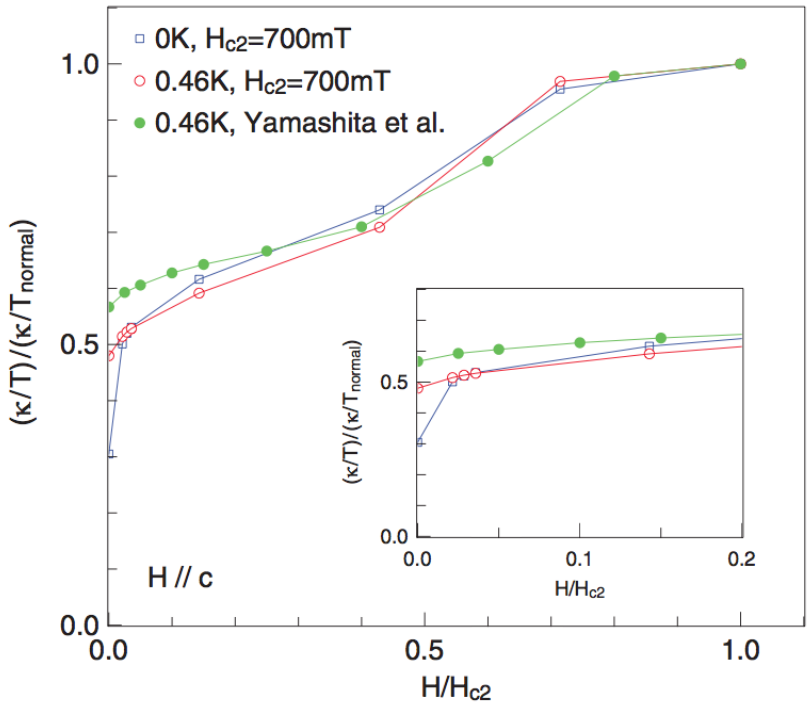

Figure 7.8: Field dependence of the thermal conductivity of LaFePO at $T \to 0$ K and $T = 0.46$ K in comparison with data taken by Yamashita *et al.* [85]. *Inset:* zoom in on the low field portion of the curve to show the rapid increase in residual conductivity in field.

Unfortunately in multiband theory, there is little difference in the thermal conductivity between d-wave and nodal $s\pm$ symmetries. The low field limit, the low-energy quasiparticles couple to the superfluid flow around the vortecies which Doppler-shifts the energy states so that the conductivity goes at $\sqrt{H}$ [97]. As the field continues to increase to H_{c2}, the fully gapped band becomes suppressed which opens a new channel for conductivity, this is observed as the increase in conductivity out of the plateau. The initial $\sqrt{H}$ behaviour is seen in the this T_c, cuprate superconductors [30], however the second upturn in conductivity as $H \to H_{c2}$ is difficult to check for experimentally as the upper critical field can be quite large, on the order of ~ 100 T [98].

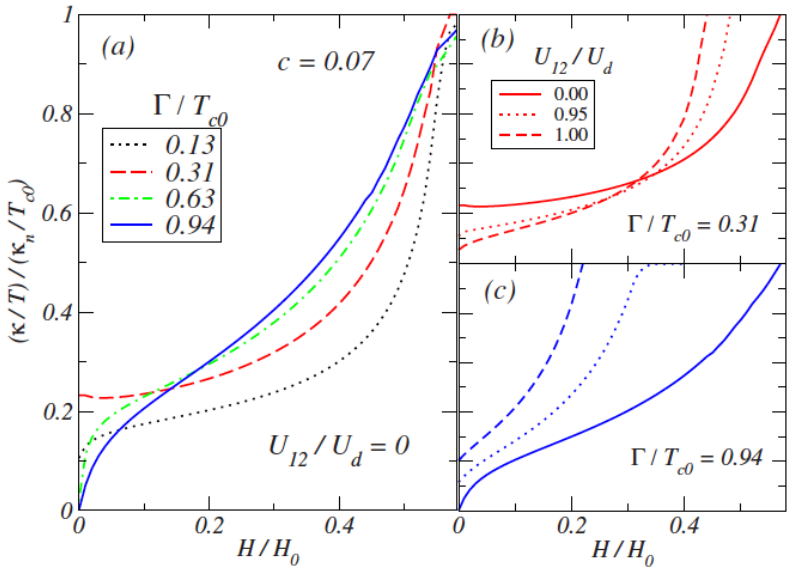

Figure 7.9: Normalized field dependence of the thermal conductivity for the nodal $s\pm$ symmetry as calculated by Mishra *et al.* [92].

We are able to qualitatively compare our normalized conductivity as a function of field to the nodal $s\pm$ gap symmetry because of the theoretical modeling of Mishra *et al.* [92] (see figure 7.9). Our data shows clear qualitative similarities to theory however the exact values of the normalized conductivity do not agree quantitatively. Further theoretical studies are needed to provide a better quantitative comparison by adjusting the tuning parameters to be material specific.

The field dependence of the conductivity does not provide compelling evidence to distinguish between either the multiband d-wave, or nodal $s\pm$ symmetries as it stands. This

being said, further experimental and theoretical efforts may help rectify the situation.

7.4 Conclusion

Our measurements of thermal and electrical conductivity at temperatures from 60 mK to 1 K on LaFePO show unambiguous evidence for low-energy, electronic quasiparticle excitations, ruling out a fully gapped order parameter. Attempting to describe the temperature dependence of the thermal conductivity with a d-wave symmetry proved fruitless in both the Born and unitary limits, building the case against the d-wave scenario for LaFePO. Comparing the field dependence of the conductivity to current theoretical models shows good qualitative agreement with the nodal $s\pm$ gap symmetry. Therefore, we conclude that the multiband, nodal $s\pm$ symmetry is a likely candidate for the symmetry of the order parameter for LaFePO, however, a careful study of universality in LaFePO will help to further distinguish between the two scenarios.

Chapter 8

$Ho_2Ti_2O_7$

8.1 Introduction

The rare-earth titanate $Ho_2Ti_2O_7$ (HTO) crystallises in the pyrochlore structure. That is, the magnetic Ho^{3+} ions are arranged on a lattice of corner sharing tetrahedra. The ground state of the large magnetic moments ($\mu = 10\mu_B$) form an almost perfect Ising system such that $|J, M_J\rangle = |8, \pm 8\rangle$ with the quantization parallel to the local $\langle 111 \rangle$ direction (into or out of each tetrahedra) [59]. We have seen that in HTO, the ground state doublet is not imposed by Kramers' rule since Ho^{3+} is a non-Kramers ion, rather it is a result of the local crystal fields. This being said, the ground state remains well isolated from the next excited state at 20.4 meV [61]. The nearest-neighbour exchange coupling between the spins is antiferromagnetic, however a dominant long-range ferromagnetic dipolar term results in a net ferromagnetic effective exchange coupling with $J_{\text{eff}} = 3$ K. This ferromagnetic effective exchange between the spins which are arranged on the pyrochlore lattice sites leads to an intriguing six-fold macroscopically degenerate magnetic ground state such that two spins are pointed into each tetrahedron and two spins are pointed out of each tetrahedron [59]. As it turns out, this arrangement of spins is analogous to the locations of the hydrogen ions in proximity with each oxygen ion in water ice. This is because each oxygen has two hydrogen atoms positioned near (covalent bonds) and two hydrogen atoms positioned far (hydrogen bonds) tetragonally [63] with the oxygen ions situated on the diamond lattice (centers of the tetrahedra in the pyrochlore lattice). The rules that describes the arrangement of protons in water ice are known as the Bernal-Fowler ice rules and therefore, the ground state spin configuration in HTO and in isostructural $Dy_2Ti_2O_7$ (DTO) also obey the Bernal-Fowler ice rules. Hence these materials have adopted the 'spin-ice' nomenclature [99, 63]. To

further validate the notion of a 'spin-ice', it has been shown that the degeneracy of the ground state gives rise to a residual entropy of $S = (1/2)\ log(3/2)$ per spin, calculated by integrating the specific heat [64, 99, 100, 72]. This yields a good approximation of Pauling's entropy for water ice. Many challenges arise when measuring the specific heat at low temperatures ($T \lesssim 500$ mK) in HTO due to extremely long time constants and a large nuclear contribution [64] which clouds the true magnetic contribution.

Excitations out of the degenerate, spin-ice ground state are the focus of much debate as they have been proposed to be analogous to 'magnetic monopole'-like quasi-particles. A monopole anti-monopole pair is created when an ice-rule breaking, spin flip occurs, creating a tetraherdon with 3 spins in and 1 spin out (monopole) and a neighbouring tetrahedron with 1 spin in and 3 spins out (anti-monopole). Now, what is interesting about these excitations is that once this initial energy barrier has been overcome, subsequent spins flips driving the pair apart do not further violate the ice rules. Instead, they move like delocalized particles following a Coulomb interaction [75]. The fundamental magnetic charge associated with a monopole is $q_m = 2\mu/a_d$, and the coulomb interaction is described by $-\mu_o q_m^2/(4\pi r)$, where r is the distance between two quasiparticles.

Sustained magnetic currents, coined 'magnetricity', have not been verified. However, attempts have been made to observe such behaviour. Somewhat controversial μSR measurements of DTO were made [81] which claimed to provide proof of monopoles, although this was disputed by another group [82] who state that the results seen in Ref. [81] were merely an artifact of the sample mount! Measurements of the electromotive force induced in a solenoid from a relaxing magnetic current were also made [101]. The results were interpreted as evidence of the magnetic Wien effect, that is, the sea of monopoles is mapped to Onsager's theory of electrolytes. The controversy surrounding the excitations out of the spin-ice ground state demands for further investigation.

Thermal conductivity measurements were made of HTO at a range of temperatures (50 mK to 1.5 K) and fields (0 T to 8 T) parallel to the [111] crystallographic direction in both the spin-ice state and the kagome-ice state. This is done to examine the magnetic excitations out of the degenerate ground state and to see how well the results can be described by current theoretical models. Thermal conductivity is an excellent tool for measuring delocalized quasi-particle excitations in materials. Thermal conductivity experiments have been conducted in DTO [78, 102], however, the magnetic excitations were assumed to either be localized and only effect the thermal conductivity through their interaction with the lattice conductivity [78], or that they are delocalized and conduct heat themselves with little effect on the phonon conductivity [102]. Either way, no thermal conductivity measurements have been made on HTO to date and thus it will add an additional perspective.

8.2 Experimental Details

The HTO sample was grown using the floating-zone image method [103]. The crystal was then prepared into a thin rectangular prism with sample dimensions 0.34 x 0.35 x 2.0 mm^3 such that the [111] crystallographic direction was parallel to the long axis. Thermal conductivity was measured via the one-heater-two-thermometer method in the spin-ice material HTO with the heat current and applied magnetic field parallel to the [111] crystallographic direction for temperatures from $T = 50$ mK to 1.4 K. The leads consisted of 50 μm silver wires which were affixed to the sample using silver epoxy in order to assure good thermal contact. Mounting the sample on the thermal conductivity device required a small copper "L" bracket, which provided a much more robust base for the sample to affix to as can be seen in figure 8.1. This also aided in aligning the crystal with the silver tail which is mounted on the fridge and is parallel with the applied field. A 10 kΩ metallic resistive heater was used and a pair of RuO_2 resistive thermometers were calibrated in-situ against the dilution fridge temperature.

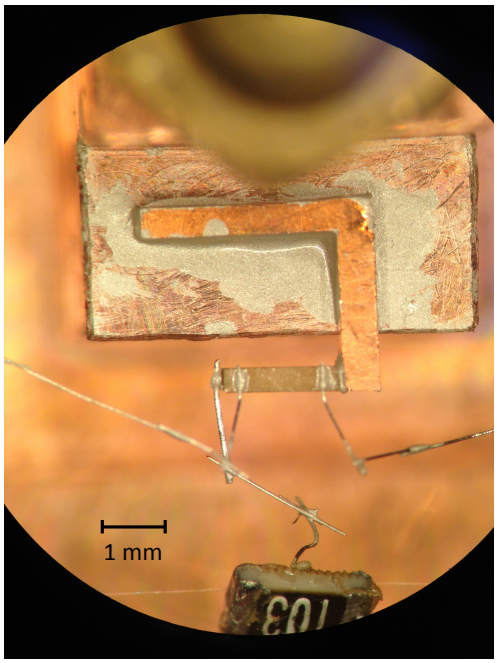

Figure 8.1: Digital image of the HTO sample with the long axis parallel to [111]. A copper "L" bracket is used to align the field with the [111] axis.

Figure 8.2 shows the magnetization curves for $H \parallel [111]$ at temperatures between 42

mK and 900 mK measured by Krey *et al.* [104]. For all reported temperatures, by the time a field of 500 mT is applied, a plateau in the magnetization is reached, indicating the onset of the "kagome-ice" state. When $H \gtrsim 2$ T (depending on the temperature) the magnetization increases to its final value, conveying that the spins are fully polarized. Thus, quasistatic temperature sweeps were conducted in a variety of applied magnetic fields between the spin-ice state at 0T and the plateau (kagome-ice) state at about 0.5 T and in the fully polarized state (the three-in-one-out/ one-in-three-out state) at 8 T in order to access the lattice contribution of the thermal conductivity.

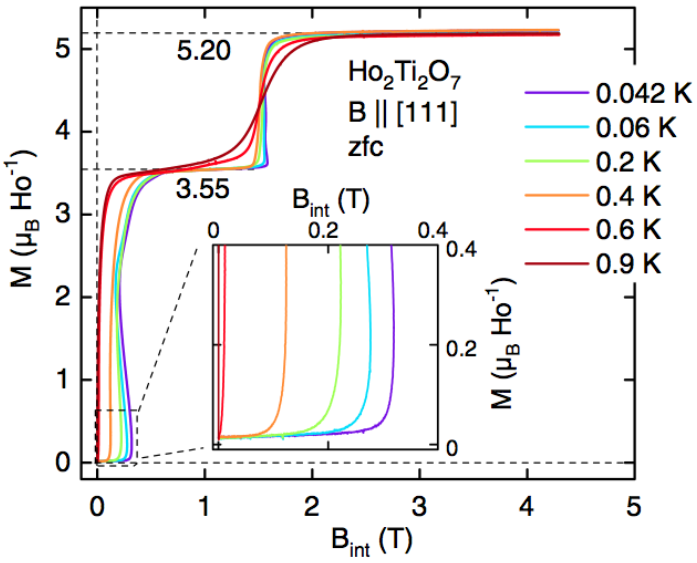

Figure 8.2: Magnetization versus field of $Ho_2Ti_2O_7$ for $H \parallel [111]$ at temperatures between 42 mK and 900 mK measured by Krey *et al.* [104].

Due to long time constants observed in the spin ice materials [78, 79], extended settling times, up to 1.5×10^4 seconds at the lowest temperatures, were allotted to ensure thermal equilibrium between the sample and the fridge. The absolute error in the value of the thermal conductivity is dominated by about a 10% uncertainty in the sample geometric factor. The relative uncertainty between temperature sweeps is less than 1%. The conductivity is also shown to be reproducible from run to run. The magnetic field was properly zeroed above 1.5 K by oscillating the polarity of the field, lowing the magnitude to zero. The sample was zero-field-cooled (ZFC) between field runs.

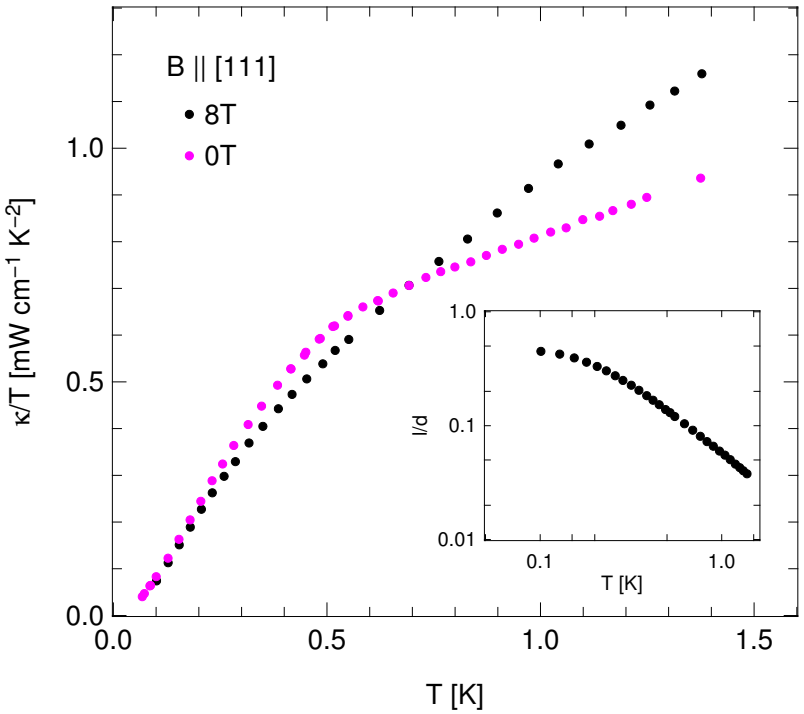

Figure 8.3: Thermal conductivity of HTO with heat current along the [111] direction in applied magnetic field of $B = 0, 8\text{T}$ parallel to [111]. *Inset:* Phonon mean free path l divided by sample width d.

8.3 Results and Analysis

Thermal conductivity divided by temperature versus temperature is plotted in figure 8.3 in applied magnetic fields of 0 T and 8 T parallel to the [111] direction. The 0 T data initially shows an increase in conductivity over the 8 T data for $T < 0.65$ K. However, above $T = 0.65$ K, the zero field conductivity is suppressed below the 8 T data, indicating the presence of an additional phonon scattering mechanism.

There are two main components to the thermal conductivity in insulating, magnetic materials: phonons and magnetic excitations. It can often be a challenge to separate these components. The phonon conductivity must first be established in the absence of any magnetic excitations in order to observe the effect of magnetic excitations on the thermal conductivity. This can be achieved a number of different ways, often by measuring a non-magnetic isostructural material or by polarizing the spins with a large magnetic field, suppressing any magnetic excitations [105]. The method of polarizing the spins was used in

this case. Magnetization measurements of HTO show that full polarization is achieved at 2.5 T for a field along the [111] direction [106]. Thus, a large 8 T field was applied parallel to the [111] direction at which point any magnetic excitations will be suppressed by this large polarizing field. Therefore, the 8 T thermal conductivity is attributed entirely to phonons. Conversely, the zero field conductivity will include contributions from magnetic excitations.

The phonon contribution to the thermal conductivity is done by examining the phonon mean free path, l. This can be extracted from the phonon conductivity via kinetic theory:

$$l = 3\frac{\kappa_{ph}}{c_{ph}v_s} \tag{8.1}$$

where $c_{ph} = 4.8\ T^3 \times 10^{-4}$ J K^{-1}mol^{-1} [72] is the phonon specific heat, $v_s = 3.2 \times 10^3$ ms^{-1} [107] is the speed of sound and $\kappa_{ph} = \kappa^{8T}_{Total}$. The mean free path, l, normalized by a geometric average of the sample width, $d = \sqrt{\frac{4A}{\pi}} = 0.41$ mm, is plotted verses temperature in the inset of Fig. 8.3. As $T \to 0$ K, the phonon mean free path approaches a value close to the sample boundary dimensions (Casimir limit), indicating that the phonon scattering is dominated by boundary scattering which is temperature independent.

As the temperature is increased, the deviation of the phonon mean free path from the boundary limited value indicates the presence of additional temperature dependent scattering mechanisms. This is described using kinetic theory and Matthiessen's rule

$$\kappa_{ph} = \kappa^{8T}_{Total} = \frac{1}{3}\frac{c_{ph}v_s^2}{\sum_i \Gamma_i} \tag{8.2}$$

where c_{ph} is the phonon specific heat, v_s is the speed of sound and Γ_i are the scattering rates from different non-magnetic mechanisms. These may include the sample boundaries (v_s/d), dislocations (T) and point defects (T^4) [10, 108]. Scattering off of point defects, dislocations and the ample boundaries are needed in order to successfully fit the phonon conductivity. The functional forms of the dislocation and point defect scattering terms are essentially exact and their coefficients are the fitting parameters, whose values can be found in table 8.1. The coefficient of the boundary scattering term, however, is entirely determined by the phonon specific heat, the sound velocity and the sample dimensions through equation 8.1. Recall that the phonon mean free path is temperature independent for boundary scattering, thus the conductivity is expected to be proportional to T^3 since the temperature dependence comes entirely from the phonon specific heat. A more realistic functional form has a power law temperature dependence whose exponent is slightly less

than 3 due to the varying effects of specular and diffuse phonon boundary scattering. This has been examined in depth in other insulating materials [7, 8, 9, 109]. The temperature dependence is thus found to to be $T^{2.85}$ from fitting the data. The complete fit of the phonon conductivity is seen in the inset of figure 8.5. The fact that point defect and dislocations play an important role in fitting the 8 T data may be a result of aspects of the crystalline structure that are not well understood, for example inter-site ion substitution or a non-stoichiometric oxygen concentration. Recent diffraction measurements on stoichiometric $Yb_2Ti_2O_7$ have revealed evidence for an excess of Yb^{3+} ions at the 2% level on the Ti^{4+} sublattice [110]. This type of weak disorder may be common in this family of pyrochlores. Further experiments are required to explore the origin of this observation in HTO.

Scattering type	**Symbol**	**Coefficient**
Boundaries	Γ_B	7.8×10^5 s^{-1}
Dislocations	Γ_D	$1.1 \times 10^7 T$ s^{-1}
Point defects	Γ_{PD}	$1.3 \times 10^6 T^4$ s^{-1}

Table 8.1: Fitting parameters of the various scattering mechanisms for the 8 T phonon conductivity.

Under the assumption that the 8 T data only consists of a phonon contribution in the absence of magnetic excitations, we now see that the 0 T data has two features that require explanation. First, there is an initial increase in conductivity over the 8 T data which indicates an additional channel for conductivity that is magnetic in origin. Second, there is a suppression of the conductivity for $T \gtrsim 650$ mK, indicating the presence of an additional scattering mechanism. Figure 8.4 shows the difference between the 8 T data and the zero field and low field data sets. This exemplifies the low temperature increase of conductivity over the 8 T data which is followed by a large decrease as the temperature is raised above 650 mK. This also illustrates how the initial increase in conductivity is suppressed with the application of a magnetic field. We can interpret this additional magnetic conductivity at low temperature as a result of delocalized magnetic monopole excitations. At the lowest temperatures the monopole density is sufficiently low that they do not significantly scatter phonons. As the temperature is increased, the density increases and thus become a source of scattering for themselves and of the phonons which results in the suppression of the thermal conductivity over the phonon conductivity in the absence of magnetic scattering. A qualitative explanation of the field dependence requires an examination of the pyrochlore crystal structure. From the perspective of the [111] direction, the pyrochlore lattice on which the Ho^{3+} reside, can be viewed as a stack of alternating kagome and triangular planes. The application of an external magnetic field in the [111]

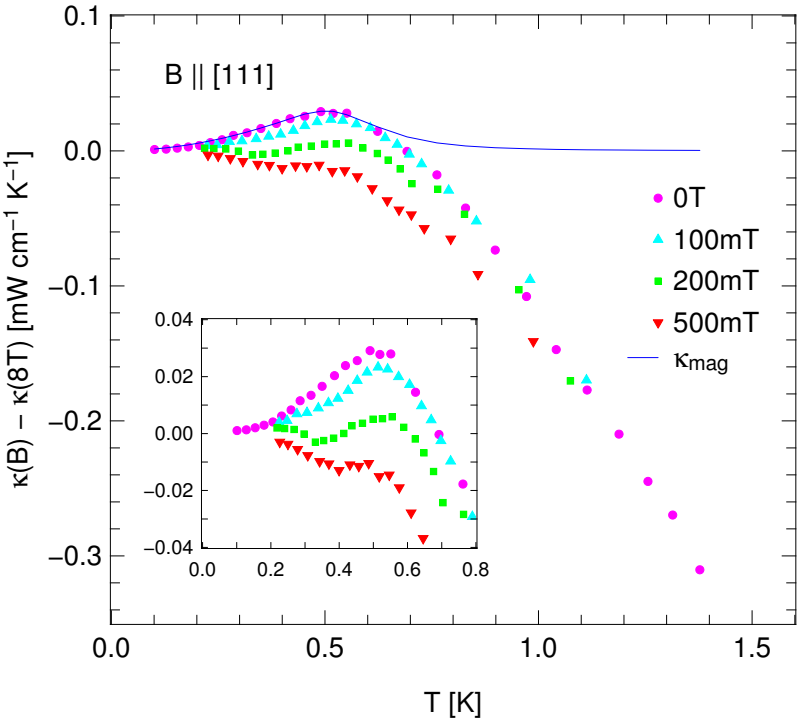

Figure 8.4: Difference between fully polarized 8 T conductivity and the low field conductivity with $B = 0, 0.1, 0.2, 0.5$ T. The magnetic contribution to the conductivity obtained from fitting is also included. *Inset:* Expanded view of the field dependence of the increase in conductivity plotted against temperature.

direction will polarize the spins in the triangular lattice first, as they are aligned parallel to the field. This effectively decouples the the triangular planes from the kagome planes while maintaining the two-in-two-out ground state. Full polarization of the spins in the triangular lattice occurs at a field around 0.5 T, at which point the system enters the 'kagome-ice' state [104]. In this state, the magnetic excitations are confined to the kagome planes which are perpendicular to the direction of heat flow and thus do not contribute to the conductivity. The excitations in this state will, however, continue to scatter phonons and thus the suppression of the conductivity above 650 mK remains. The small bump seen in the 500 mT data may be due to a slight misalignment of the crystal in the magnetic field. So, a small increase in conductivity is still observed in the kagome-ice state because of the transverse component.

The low field thermal conductivity clearly shows that the magnetic excitations conduct

heat and provide a scattering mechanism. Therefore, our fit of the the 0 T data must include an additional magnetic contribution to the conductivity, κ_{mag}, and also a magnetic contribution to the phonon scattering, Γ_{mag}. Thus the total zero field conductivity can be written as:

$$\begin{aligned}\kappa_{Total}^{0T} &= \kappa_{mag} + \frac{1}{3}\frac{c_{ph}v_s^2}{\Gamma_{mag} + \sum_i \Gamma_i} \\ &= \kappa_{mag} + \left(\frac{3}{c_{ph}v_s^2}\Gamma_{mag} + \frac{1}{\kappa_{Total}^{8T}}\right)^{-1}\end{aligned} \tag{8.3}$$

The functional form of the magnetic contribution to the conductivity, κ_{mag}, is unknown. We will assume that the main scattering mechanism at low temperatures is due to point defects and therefore temperature independent, we will use the form expected for massive excitations in three dimensions which states that $\kappa_{mag} \sim T^2$ [111]. As the temperature increases, the monopoles, which are mobile, begin to noticeably scatter each other. A simple form for the scattering rate is assumed to be proportional to the monopole density, $\rho(T)$. The total magnetic contribution to the thermal conductivity can thus be written as $\kappa_{mag} = T^2(a + b\rho(T))^{-1}$ where a and b are fitting parameters. The result of this fit can be seen in figure 8.4, which shows that this simple model provides an excellent fit of the data at low temperatures. The monopole density is low is the temperature regime, so the phonon scattering is small and the direct subtraction of the 8 T data form the 0 T data accurately reflects the magnetic contribution. However, after the peak in the conductivity, the monopole density rapidly increases and the increased scattering affects both the magnetic and phonon conductivity thus the subtracted data includes the suppression of both phonons as well as the monopole current.

Turning our attention now to the magnetic-phonon scattering, a first approximation is that it will also be proportional to the monopole density. That is, $\Gamma_{mag} \propto \rho(T)$ where $\rho(T)$ is derived from Debye-Hückel theory [112], such that:

$$\rho(T) \propto \frac{2e^{-\Delta_d/T}}{1 + 2e^{-\Delta_d/T}} \sim e^{-\Delta_d/T} \ (T \to 0K) \tag{8.4}$$

Δ_d is the dressed energy required to create an isolated monopole. Equation 8.5 shows how the surrounding monopoles cause a screening effect that reduces the Coulomb energy needed to separate a monopole-antimonopole pair until they are free. This results in a reduction of the energy required to create an isolated monopole from the unscreened value of $\Delta = 5.8$K [112] (a reduction of about 5% at T=0.5 K). Figure, 8.6 shows the

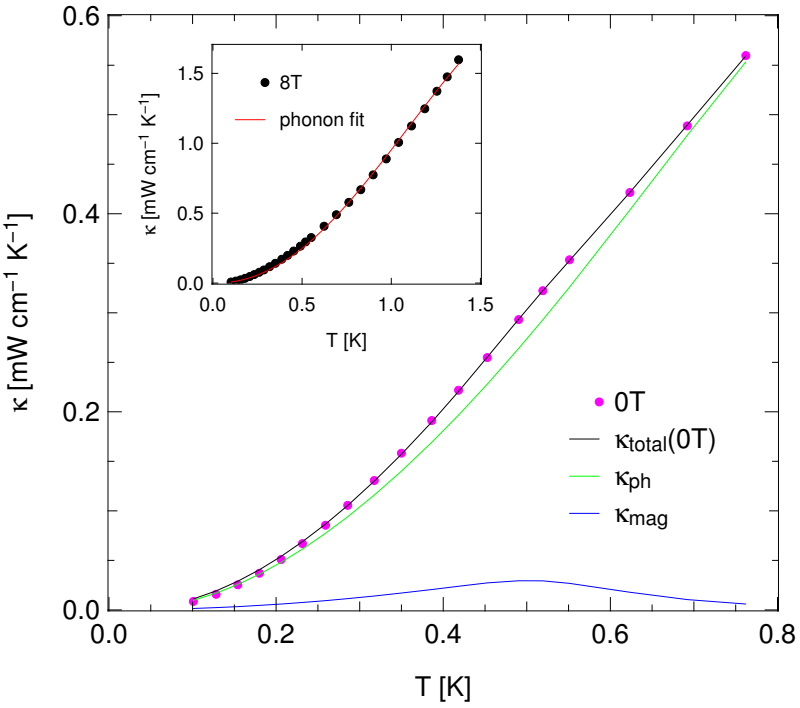

Figure 8.5: Full zero field thermal conductivity fitted to equation 8.3 such that $\kappa_{mag} = T^2(a + b\rho(T))^{-1}$ and $\Gamma_{mag} \propto \rho(T)$. The individual components to the conductivity, κ_{mag} and κ_{ph} (green line), are also represented. *Inset:* Thermal conductivity in an applied field of 8 T fitted using kinetic theory described in equation 8.2.

creation energy versus temperature in both the screened and unscreened cases as well as the monopole density as a function of temperature.

$$\Delta_d = \Delta - \frac{1}{2}\frac{E_{nn}}{\frac{\xi_{Debye}}{a_d}} \tag{8.5}$$

$$\frac{\xi_{Debye}}{a_d} = \sqrt{\frac{2}{3\sqrt{3}\pi E_{nn}}}\sqrt{\frac{T}{\rho(T)}} \tag{8.6}$$

The screening length, ξ_{Debye}, is calculated in equation 8.6. The diamond lattice constant, $a_d = \sqrt{3/2}\ a = 4.34$Å, is the distance between the centers of neighbouring tetrahedra and therefore the nearest neighbour distance between monopoles. The Coulomb energy of two monopoles on neighbouring sites is $E_{nn} = 3.06$K. There is no analytical solution to

equations 8.4 to 8.6 which must be solved self-consistently. The bisection method was used to solve for the monopole density and the creation energy, which are plotted in figure 8.6.

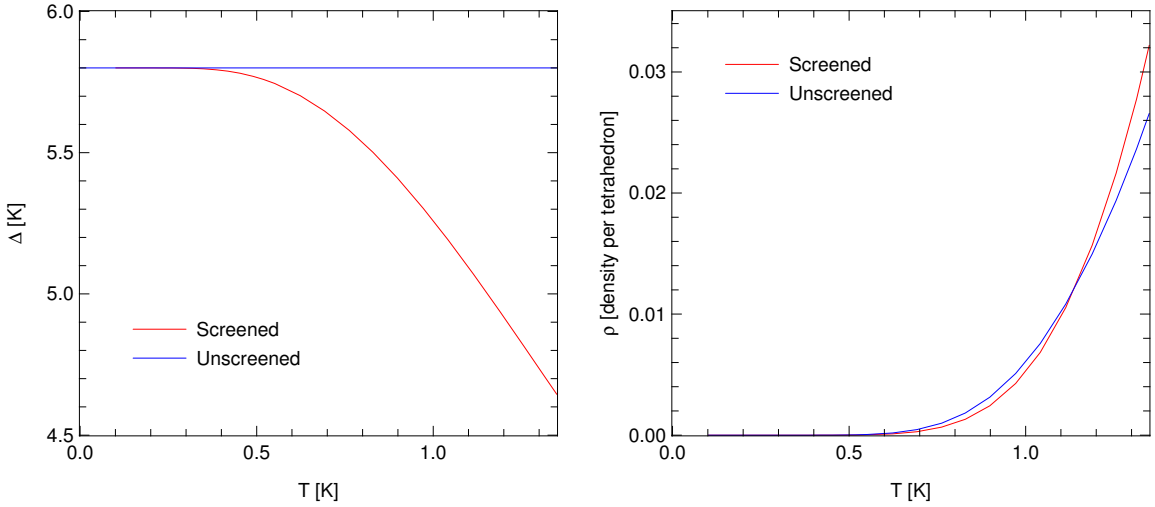

Figure 8.6: **(a)** Screened and unscreened isolated monopole energy cost. **(b)** Screened and unscreened monopole densities per tetrahedron determined by numerical solution to equations 8.4 to 8.6.

To access the monopole-phonon scattering, we fit the full zero field data to equations 8.3 - 8.6. The coefficients from the fit are listed in table 8.2. The best fit can be seen in figure 8.5 [**?**] along with the individual components to the conductivity, κ_{mag} and κ_{ph}.

Term	**Symbol**	**Functional form**
MP conductivity	κ_{mag}	$T^2(7.2 + 1.4 \times 10^5 \rho(T))^{-1}$
MP-PH scattering	Γ_{mag}	$1.2 \times 10^8 \rho(T)$

Table 8.2: Fitting parameters for the magnetic contribution to the thermal conductivity (MP conductivity) and the monopole-phonon scattering rate (MP-PH scattering).

This description of the temperature dependence is qualitatively excellent. This indicates that the additional transport is not only provided by the magnetic excitations well-described by our model, but also the monopole-phonon scattering that is proportional to the temperature dependence of the monopole density. From a quantitative stand point, the only fitting parameters are the two coefficients in κ_{mag} and the coefficient in front of $\rho(T)$ in Γ_{mag}. The monopole-phonon scattering rate obtained from our fit at $T = 500$ mK is approximately 10^8 s^{-1} which the same order of magnitude reported for the magnetic

scattering of phonons (τ_γ) in DTO [78]. Further theoretical work will be required to see if the other values obtained are reasonable.

We don't expect a contribution from collective magnetic excitations such as loop flips described by Melko *et al.* [63] as they are not experimentally accessible at these temperatures due to a large energy barrier.

8.4 Conclusion

The zero field thermal conductivity measurements have shown an additional channel for heat conduction at low temperatures and evidence for an additional phonon scattering mechanism for $T \gtrsim 0.65$ K which is magnetic in nature. This is interpreted as magnetic quasiparticle excitations which carry heat and are able to scatter each other as well as phonons. The additional magnetic contribution to thermal conductivity, κ_{mag} is a result of the monopole like excitations scattering off of each other and off of massive excitations. The magnetic-phonon scattering rate, Γ_{mag} is taken to be proportional to the monopole density, $\rho(T)$ which is determined by Debye-Hückel theory. This simple fit provides excellent qualitative agreement with the data. However, further theoretical work is needed to quantitatively investigate the validity of the fit parameter values. This provides compelling evidence that the delocalized magnetic excitations can be thought of as magnetic monopole-like quasiparticles.

Chapter 9

Conclusion

Thermal conductivity measurements were made on a variety of different systems in order to probe the behaviour of their ground states. This is because thermal conductivity provides information on low energy, delocalized quasiparticles either through the presence of an additional channel for conductivity, or an additional scattering mechanism. Hence, thermal conductivity is an extremely versatile measurement of the bulk and can be applied to many different materials. In this thesis we have seen how to improve the quality of thermal conductivity measurements by minimizing the noise caused by electromagnetic interference. We have then applied this technique to an iron-based superconducting material, LaFePO, and a spin-ice material, $Ho_2Ti_2O_7$, in an attempt to uncover details about their ground state and the excitations out of the ground state. A brief summary of the results follows.

9.1 Summary

A new design for an improved thermal conductivity mount is discussed. The design is in essence to build the mount directly into a copper box. This is done to provide an efficient RF shield of the sample thermometers, which also adds a layer of protection for the delicately balanced components and sample from foreign objects. The improvement is quantified by looking at the relative noise on the sample thermometers between the old wire frame design and the new box design which shows an order of magnitude reduction in noise.

The symmetry of the order parameter was probed in the iron-based superconductor, LaFePO using thermal transport measurements. A non-zero electrical component to the

thermal conductivity that is a substantial fraction of the normal state conductivity (31%) is observed. This is taken as unambiguous evidence for low-energy, electronic quasiparticle excitations, ruling out a fully gapped order parameter. Although the d-wave scenario accurately predicted the residual electronic thermal conductivity, it failed to describe the temperature dependence in both the Born and unitary limits. The field dependence, however, is consistent with current theoretical models of the nodal $s\pm$ gap symmetry. Therefore, the multiband, anisotropic $s\pm$ symmetry is the best candidate for the order parameter of LaFePO. This being said, further theoretical work is required to confirm one picture over the other.

Thermal conductivity measurements of the spin-ice $Ho_2Ti_2O_7$ in applied magnetic fields up to 8 T with both the heat current and field parallel to the [111] direction. Applying a field of 8 T fully polarizes the magnetic moments, allowing us to extract the phonon contribution which can be described using conventional, non-magnetic scattering mechanisms such as the sample boundaries, dislocations and point defects. The low field data shows that the excitations out of the spin-ice ground state give rise to an additional channel for heat conduction which also effectively scatters phonons. The magnetic contribution to the thermal conductivity is a result of the magnetic excitations scattering off of both massive excitations and off each other. The magnetic-phonon scattering rate is proportional to the monopole density as determined by Debye-Hückel theory. We interpret this as evidence for magnetic monopole-like excitations.

APPENDICES

Appendix A

β-$YbAlB_4$

A.1 Introduction

A quantum critical point (QCP) arises when a continuous phase transition occurs between two competing phases at zero temperature. In this case, strong quantum fluctuations drive the the transition rather than thermal fluctuations as in classical critical points. The quantum fluctuations can lead to the formation of a new phase of matter [113, 114] which may not follow normal Fermi-liquid behaviour in metals [115]. Heavy-Fermion materials are often in focus when studying antiferromagnetic quantum criticallity since there is a debate as to whether many types of QCPs exist and are differentiated by their macroscopic properties.

Generally, quantum criticallity in metallic systems is described by the Hertz-Moriya-Millis framework [116, 117, 118, 119]. Here, antiferromagnetic order stems from spin density wave (SDW) order. When this magnetic order is suppressed, a paramagnetic state materializes with heavy electronic quasiparticles due to the Kondo screening of the f-electron moments by the conduction electrons. This framework provides an excellent description of many materials, however, the presence of localized moments and Fermi surface reconstruction can lead to a more exotic type of quantum criticallity [120]. Theories attempting to describe this exotic behaviour by introducing an effective Kondo temperature collapses at the QCP leading to a breakdown of the heavy-Fermion metallic state [121, 122]. At the Kondo-breakdown QCP, the Kondo effect no longer occurs and the f electrons decouple from the conduction band [123, 124]. Distinguishing between these two scenarios can be difficult because the fermi-surface reconstruction and the breakdown of the Kondo effect are not easy to observe. Thus, attempting to detect the breakdown of the Landau quasi-

particles using thermal and electrical transport measurements is a promising alternative route to observing a more exotic type of QCP. For example, spinons are known to exist in the Kondo-breakdown picture, which are additional entropy carriers [125]. This means that the thermal conductivity will surpass the electrical conductivity resulting in a violation of the Wiedemann-Franz law (WFL) as $T \to 0$ K. A violation of the WFL is not expected to exist near more conventional QCPs since the quasiparticles are expected to stay intact. Therefore, thermal and electrical transport measurements are extremely useful tools for investigating quantum critical systems through the WFL.

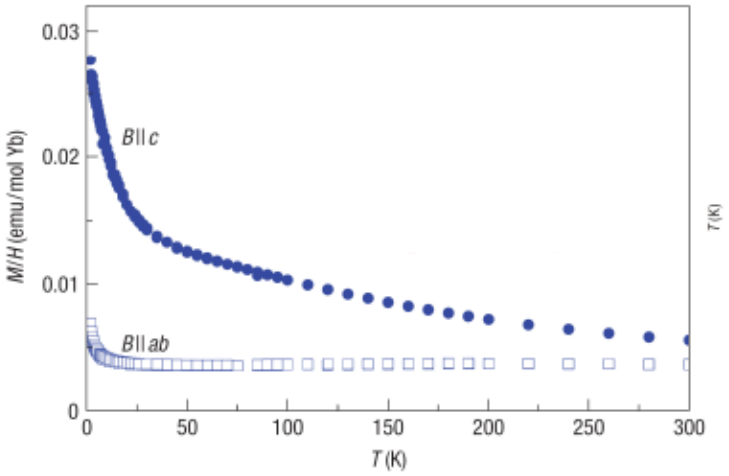

Figure A.1: Magnetization of β-$YbAlB_4$ measured by Nakastuji *et al.* [126] for $B \parallel c$ and $B \parallel ab$. The $B \parallel c$ magnetization diverges as $T \to 0$ K.

The focus of this chapter is on the heavy Fermion superconductor β-$YbAlB_4$ - the first Yb based, heavy Fermion metal which displays superconductivity. The superconducting transition temperature is ~ 80 mK which can be fully suppressed with a field of 50 mT. What is interesting about this material is that the QCP occurs almost exactly at ambient conditions, that is, it does not require an external tuning parameter such as pressure or magnetic field to generate the critical behaviour. Magnetic susceptibility measurements have shown an unusual T/B scaling (figure A.1) and an effective mass that diverges as $B^{-1/2}$. Specific heat measurements confirm a divergent effective mass as $T \to 0$ K (see figure A.2) [127]. Strong valance fluctuations have also been observed which suggests an unconventional QCP [128].

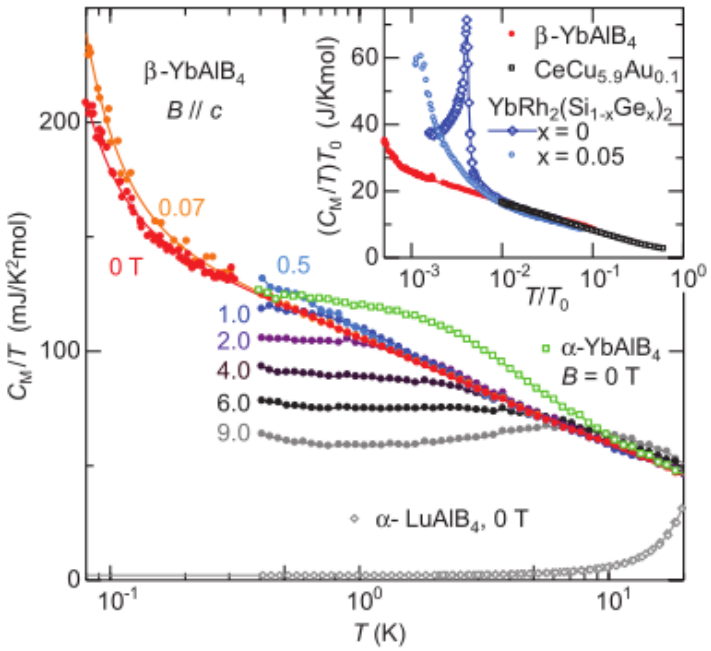

Figure A.2: Specific heat of β-$YbAlB_4$ diverging as $T \to 0$ K for $B = 0$ T. *Inset:* Specific heat of $CeCu_{5.9}Au_{0.1}$ and $YbRh_2(Si_{1-x}Ge_x)_2$ for $x = 0, 0.05$. The Ge substitution in $YbRh_2Si_2$ drives the peak in specific heat to $T = 0$ K, tuning the system to become quantum critical [127].

A.2 Experimental Details

Thermal conductivity and electrical resistivity measurements were made on high quality single crystals of β-$YbAlB_4$ using the one-heater-two-thermometer method described in section (Experimental Details). Thin platelets were grown using the flux method [129] with typical sample dimensions of approximately 2mm $\times$ 200μm $\times$ 15 μm with the b-axis perpendicular to the platelet. The residual resistivity ratio (RRR = $\rho_{300\,\mathrm{K}}/\rho_0$) and geometric factor ($geom$ = length/area) of the two samples presented here are found in table A.1. The magnitude of the RRR values ensure the high quality of these samples. The relative error between thermal and electrical measurement is estimated to be about 3%, due mainly to slightly different effective contact separations for heat and charge measurements.

Contacts with very low electrical resistance (<5 mΩ) were prepared by first ion milling the surface of the crystal to guarantee excellent thermal and electrical contact. Pt contacts

Sample	RRR	*geom* (cm^{-1})
1 (k9-5)	300	8547
2 (S5)	240	8757

Table A.1: Residual resistivity ratio (RRR) and geometric factor (*geom*) of the two β-$YbAlB_4$ samples presented in this chapter.

were then deposited onto the sample so that Au wires could be connected either by spot welding to the contacts or by using Dupont 6838 Ag epoxy.

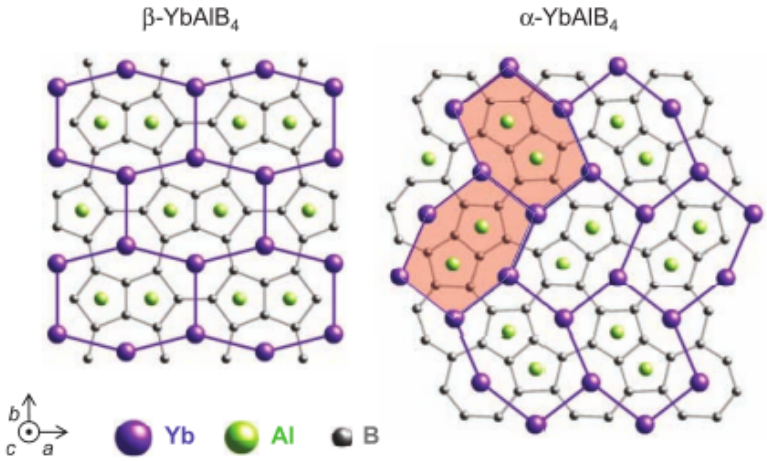

Figure A.3: The two structural forms that $YbAlB_4$ crystallizes into. α forms a zig-zag structure whereas β forms a straight structure [127].

Figure A.3 shows how Yb, Al and B can crystallize into two main forms, α-$YbAlB_4$ and β-$YbAlB_4$. Both comprised of repeating layers stacked in the c direction. The α structure forms a herringbone pattern whereas the β structure is more of a compressed honeycomb lattice. The focus of this section is on β-$YbAlB_4$ since is supports superconductivity and has unconventional quantum critical behaviour.

A.3 Results and Discussion

Thermal resistivity ($w = L_0T/\kappa$) and electrical resistivity (ρ) are plotted vs. temperature in figure A.4 for sample 2 (RRR $\sim$ 240) in zero field and in figure A.5 b)-e) for sample

1 (RRR $\sim$ 300) in a range of fields from 0 T to 2 T. The onset of superconductivity is clearly seen in figure A.4 as a rapid drop in the electrical resistivity with $T_c \approx 75$ mK which is easily suppressed with a field of 50 mT applied along the c direction. The critical temperature in sample 1 is slightly higher with $T_c \approx 80$ mK as it is cleaner. However, there is no corresponding feature in the thermal conductivity right down to 60 mK (the lowest measured temperature) in either sample. This might be an indication that superconductivity only exists on the surface or small sections of the sample, or that it only exists in the bulk at lower temperatures because thermal conductivity is a measurement of the bulk whereas electrical resistivity can be surface sensitive.

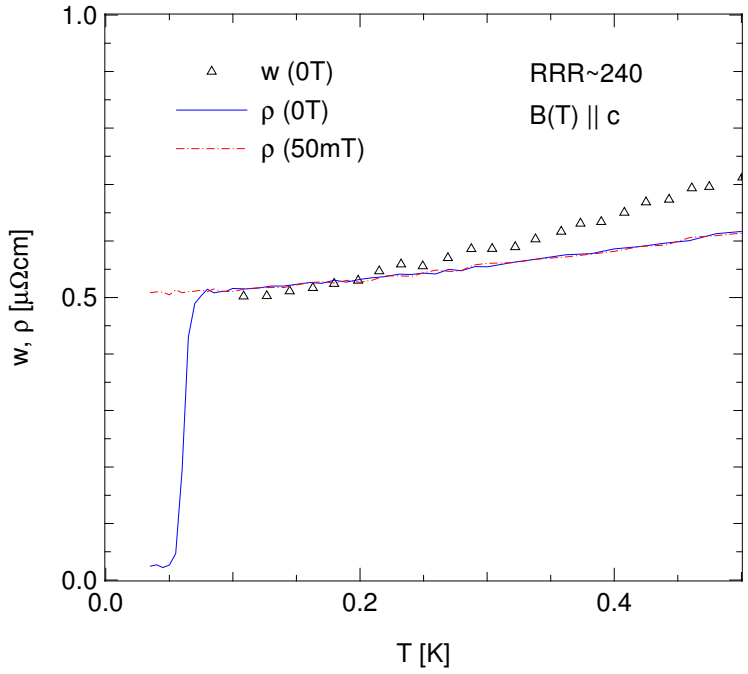

Figure A.4: Thermal (open triangles) and electrical resistivity are plotted vs. temperature. A field of 50 mT (red dashed line) is enough to suppress superconductivity seen in the zero field (blue solid line) data.

A schematic of the field vs. temperature phase diagram for β-$YbAlB_4$ based on the transport data in reference [126] is seen in figure A.5 a). It shows that in zero field, β-$YbAlB_4$ is in a non-Fermi-liquid (nFL) state at low temperatures which is characterized by an electrical resistivity $\rho(T) \sim T^{1.5}$, a magnetic susceptibility $\chi_c \sim T^{1/3}$ and an electronic specific heat $\gamma \sim ln(T^*/T)$ (see figure A.2) with $T^* = 200$ K [126]. The superconducting phase has been omitted from this diagram.

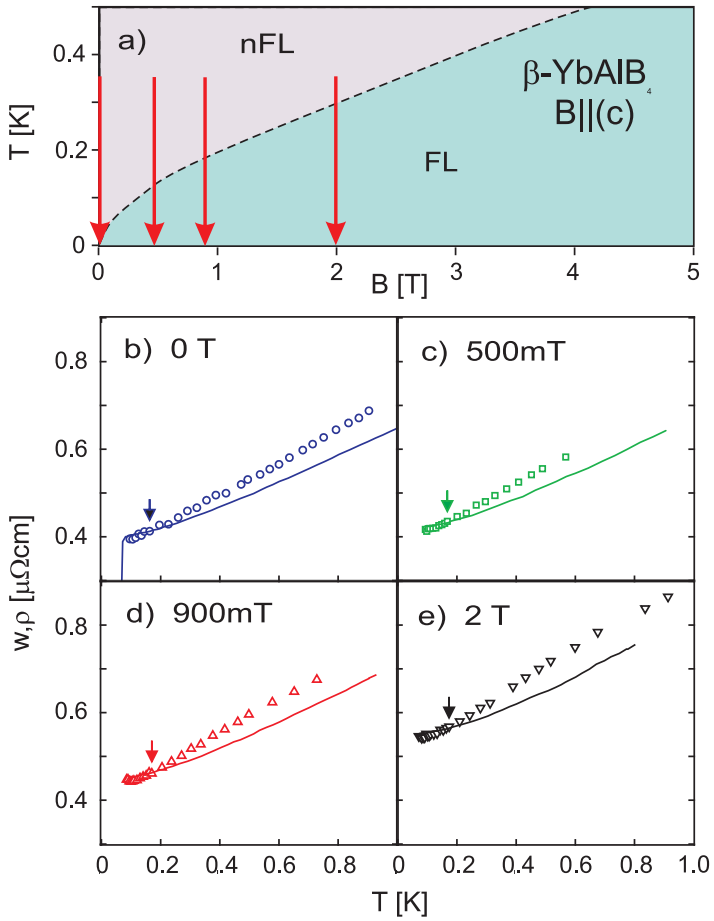

Figure A.5: (a) Schematic of a temperature vs. field phase diagram of the Fermi-liquid (FL) and non-Fermi-liquid (nFL) behaviour based on Nakastiji's transport data [126]. Thermal (open symbols) and electrical (lines) resistivity of β-$YbAlB_4$ (sample 1 with RRR $\sim$ 300) in fields of (b) 0 T, (c) 500 mT, (d) 900 mT and (e) 2 T with $B \parallel$ c. The arrows show where the WFL is recovered.

Fitting the 0 T resistivity in figure A.5 a) to $\rho(T) = \rho_0 + T^n$ yields $\rho_0 \sim 0.4\mu\Omega$cm and $n \sim 1.5$ which demonstrates the non-Fermi-liquid like behaviour of the system. As the field is increased, ρ_0 increases as can be seen in figure A.5 c)-e). Also, $\rho(T) \sim T^2$ by $B = 2$ T indicating the return to the normal Fermi-liquid behaviour.

In general, in a paramagnetic metal, heat conduction is caused by both electrons (κ_{el}) and phonons(κ_{ph}). However in the low T limit, the conductivity in samples with low

residual resistivities ($\rho_0 \lesssim 1\mu\Omega$cm) will be dominated by the electronic contribution. That is $\kappa_{el} \gg \kappa_{ph}$ and thus we can ignore the phonon conductivity for $T < 1$ K. This is the case in other metallic samples with similar residual resistivities, such as $YbRh_2Si_2$ [130], $CeCoIn_5$ [131], $CeRhIn_5$ [132] and $ZrZn_2$ [133].

A comparison of the thermal (w) and electrical (ρ) resistivities leads to a direct test of the WFL. The convergence of w and ρ in figures A.4 and A.5 provides clear evidence that the WFL is satisfied for $T < 200$ mK in both zero field and in applied magnetic fields for both reported samples to within the 3% experimental error. This becomes even more evident by looking at the Wiedemann-Franz ratio ($L = \kappa/\sigma T$) normalized by the Lorenz number ($L_0 = 2.44 \cdot 10^{-8}$ W Ω / K^2) as seen in figure A.6.

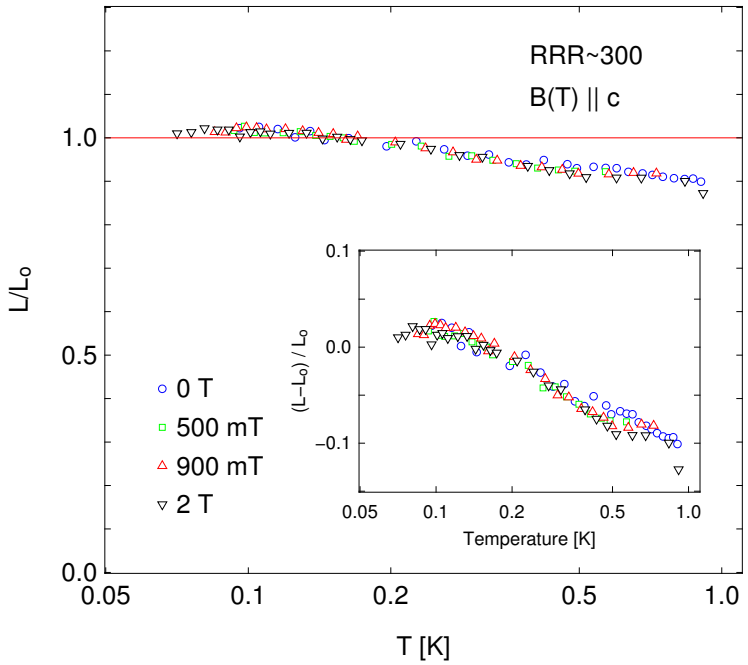

Figure A.6: Wiedeman-Franz ratio ($L = \kappa/\sigma T$) normalized by the Lorenz number ($L_0 = 2.44 \cdot 10^{-8}$ W Ω / K^2) vs. temperature. *Inset:* Deviation from the WFL.

Comparing these results to other similar quantum critical systems reveals some interesting differences. A recent study of $YbRh_2Si_2$ shows a 10% violation of the WFL at the Kondo-breakdown QCP [130]. They report $L/L_0 \sim 0.9$ as $T \to 0$ K indicating a higher conductivity of charge than heat. At the field tuned QCP in $CeCoIn_5$, the WLF is satisfied in one direction but violated in another [131]. It is thought that in these two materials that Landau quasiparticles no longer provide an accurate description of the excitations

out of the ground state. However, even though β-$YbAlB_4$ shows unconventional behaviour in transport and magnetic properties, the quasiparticles remain intact near the QCP and continue to carry heat and charge. Although some work has been done to describe the behavior seen in $YbRh_2Si_2$ [134], this theory has not yet been applied to β-$YbAlB_4$.

Looking at the temperature dependence of L/L_0 in figure A.6, it is evident that L/L_0 dips below unity for $T > 200$ mK. This is indicative of how inelastic scattering effects charge and heat carriers differently. This is because in a scattering event, both the charge and heat current can degrade due to the deflection of the electron. In an inelastic scattering event, the heat current is reduced even further because of the loss of kinetic energy but charge remains conserved. Thus elastic scattering events will effect both charge and heat conducting equally because kinetic energy is conserved, and therefore elastic scattering will not violate the WFL.

A possible explanation for the slight WFL violation is a fractionalized Fermi-liquid ground state, which is a suggested model for heavy-Fermion systems near unconventional QCP's [135, 136]. However, this model predicts a larger violation of the WFL than is observed, resulting in a poor description of the system. Another possibility is that the ground state forms a spin liquid with Fermion excitations known as spinons which carry heat but not charge [134]. The problem with this scenario is that it results in an excess of heat conductivity which would make $L/L_0 > 1$ which is not the case for our data.

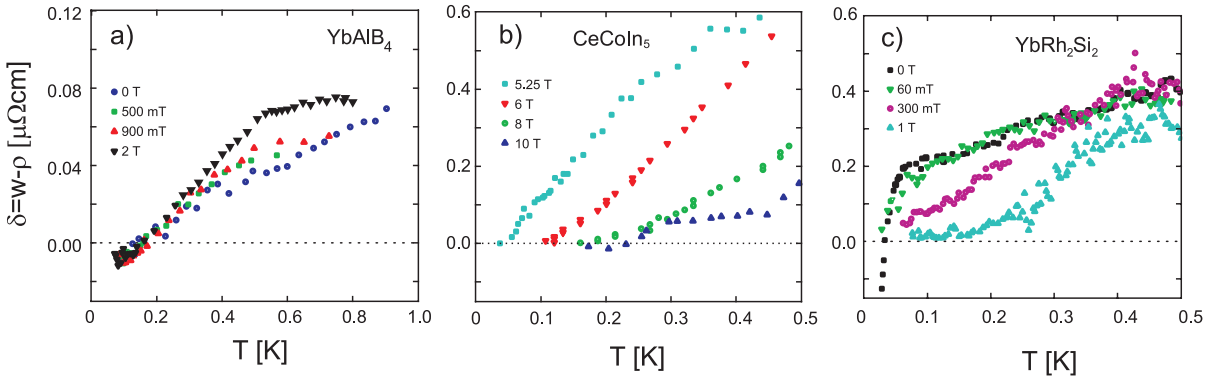

Figure A.7: Wiedeman-Franz ratio ($L = \kappa/\sigma T$) normalized by the Lorenz number ($L_0 = 2.44 \cdot 10^{-8}$ W Ω / K^2) vs. temperature. *Inset:* Deviation from the WFL.

Figure A.7 shows the difference between thermal and electrical resistivities ($\delta(T) = w - \rho$) vs. temperature for β-$YbAlB_4$, $CeCoIn_5$ and $YbRh_2Si_2$ for a variety of fields around their QCPs. $\delta(T)$ provides a good measure of the inelastic scattering caused by quantum

fluctuations [132, 137, 138]. One might expect $\delta(T) \sim T^2$ because of electron-electron scattering, or $\delta(T) \sim T^3 + T^5$ because of electron-phonon scattering [139], however this is not the case here where $\delta(T) \sim T$ up to about 500 mK followed by a slight sublinear behaviour for $T > 500$ mK. Another curiosity about the β-$YbAlB_4$ data is that $\delta(T)$ seems rather constant in field for $T < 500$ mK indicating a field independent scattering mechanism. This is in contrast to the field driven quantum critical systems such as $YbRh_2Si_2$ ($H_c = 60$ mT [130]) and $CeCoIn_5$ ($H_c = 5.2$ T [140]) which show substantial field dependence in $\delta(T)$. A final note worth pointing out is the relative magnitudes of $\delta(T)$ between the three samples. $\delta(T)$ in β-$YbAlB_4$ is about an order of magnitude lower than in $YbRh_2Si_2$ or $CeCoIn_5$. This shows that the inelastic scattering is much smaller in β-$YbAlB_4$ than in the other materials. That being said, it is not merely due to relative differences in the impurity scattering levels since it lies between the two: *ie.* $\rho_0 = 0.1\mu\Omega$cm for $CeCoIn_5$, $\rho_0 = 0.4\mu\Omega$cm for β-$YbAlB_4$ and $\rho_0 = 1.6\mu\Omega$cm for$YbRh_2Si_2$. These three questions still require more theoretical work in order to develop an accurate description of quantum criticallity in β-$YbAlB_4$.

A.4 Conclusion

A complex picture of quantum criticallity has been revealed in β-$YbAlB_4$. It has shown non-Fermi-liquid like behaviour in electrical resistivity, susceptibility and specific heat, all characteristics of an unconventional QCP. However, agreement with the Wiedemann-Franz law indicates that the Landau quasiparticles remain intact at or near the QCP, which is conventional QCP behaviour. Theoretical work is needed to devise a model which is able to describe the nFL behaviour yet agrees with the Landau quasiparticle picture. This theory also needs to address the issue of a linear $\delta(T)$ which is field independent and much smaller in magnitude than other comparable quantum critical systems.

Appendix B

Thermal Conductivity Mount Drawings

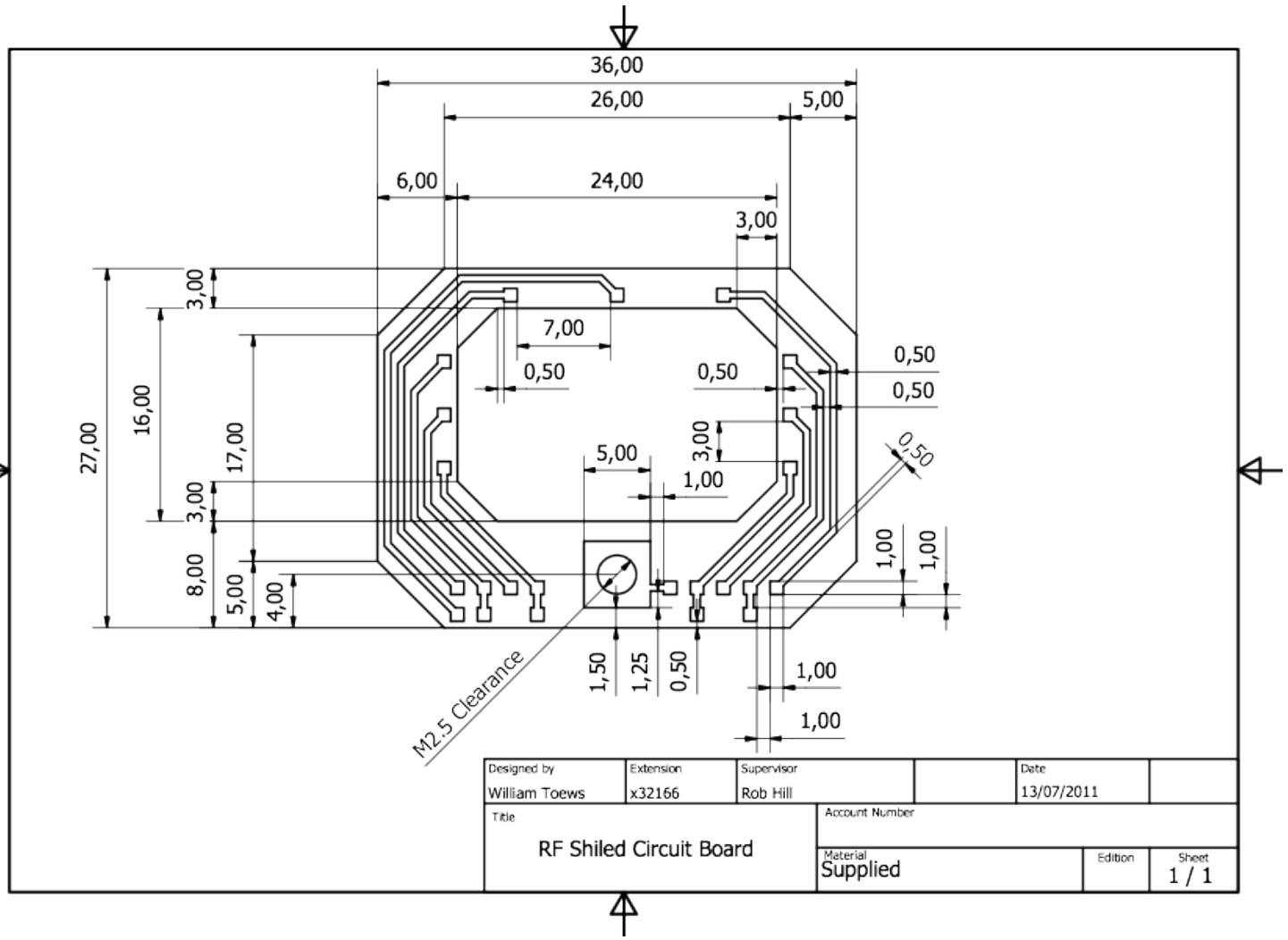
36,00
26,00
5,00
6,00
24,00
3,00
3,00
7,00
0,50
0,50
0,50
0,50
27,00
16,00
17,00
3,00
5,00
1,00
0,50
3,00
1,00
1,00
8,00
5,00
4,00
1,50
1,25
0,50
1,00
1,00
M2.5 Clearance
Designed by
William Toews
Extension
x32166
Supervisor
Rob Hill
Date
13/07/2011
Title
RF Shiled Circuit Board
Account Number
Material
Supplied
Edition
Sheet
1 / 1

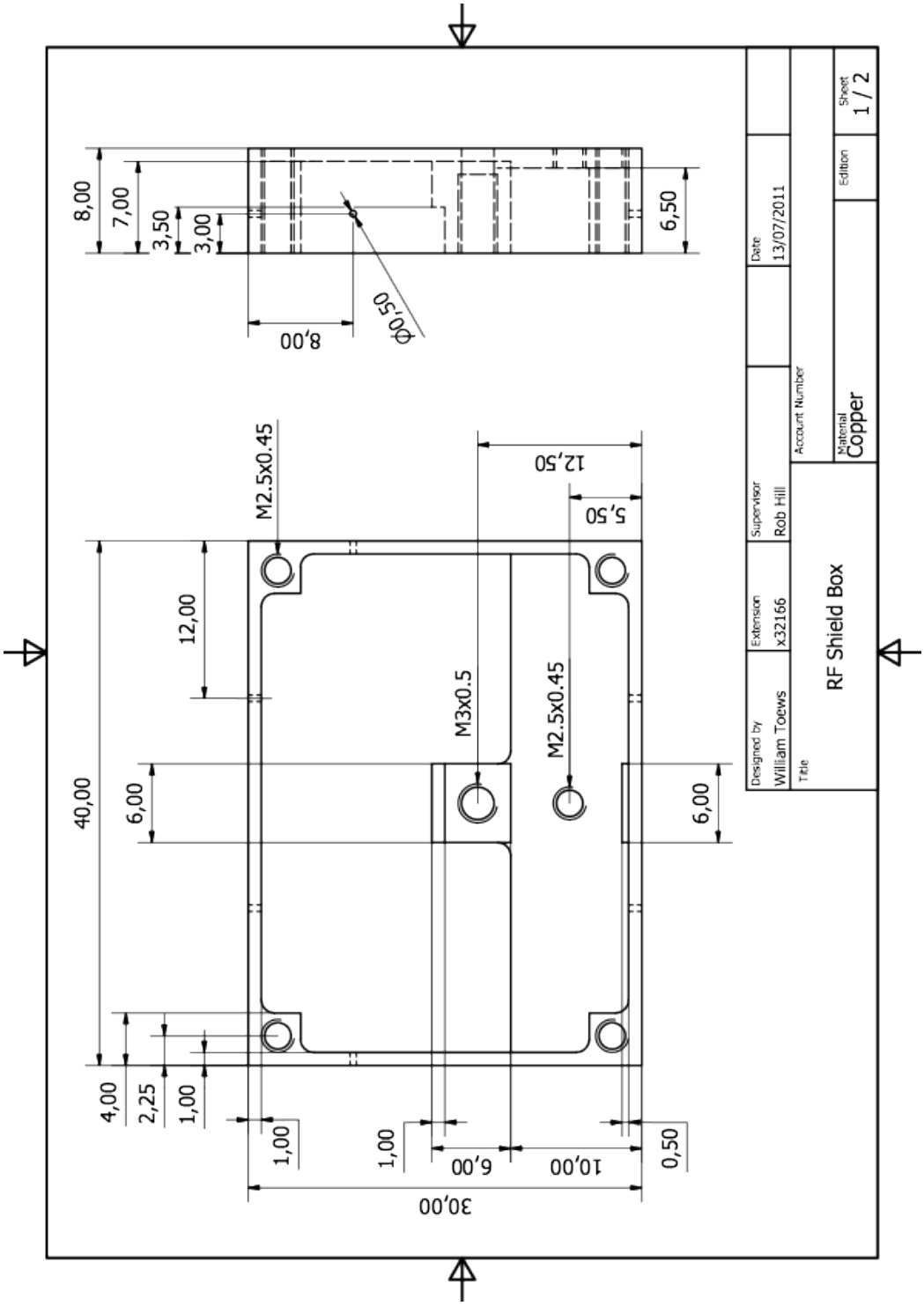
8,00
7,00
3,50
3,00
6,50
8,00
ϕ0,50
M2.5x0.45
12,50
5,50
12,00
M3x0.5
M2.5x0.45
40,00
6,00
6,00
4,00
2,25
1,00
1,00
1,00
6,00
10,00
0,50
30,00
Designed by
William Toews
Extension
x32166
Supervisor
Rob Hill
Account Number
Material
Copper
Date
13/07/2011
Edition
Sheet
1 / 2
Title
RF Shield Box

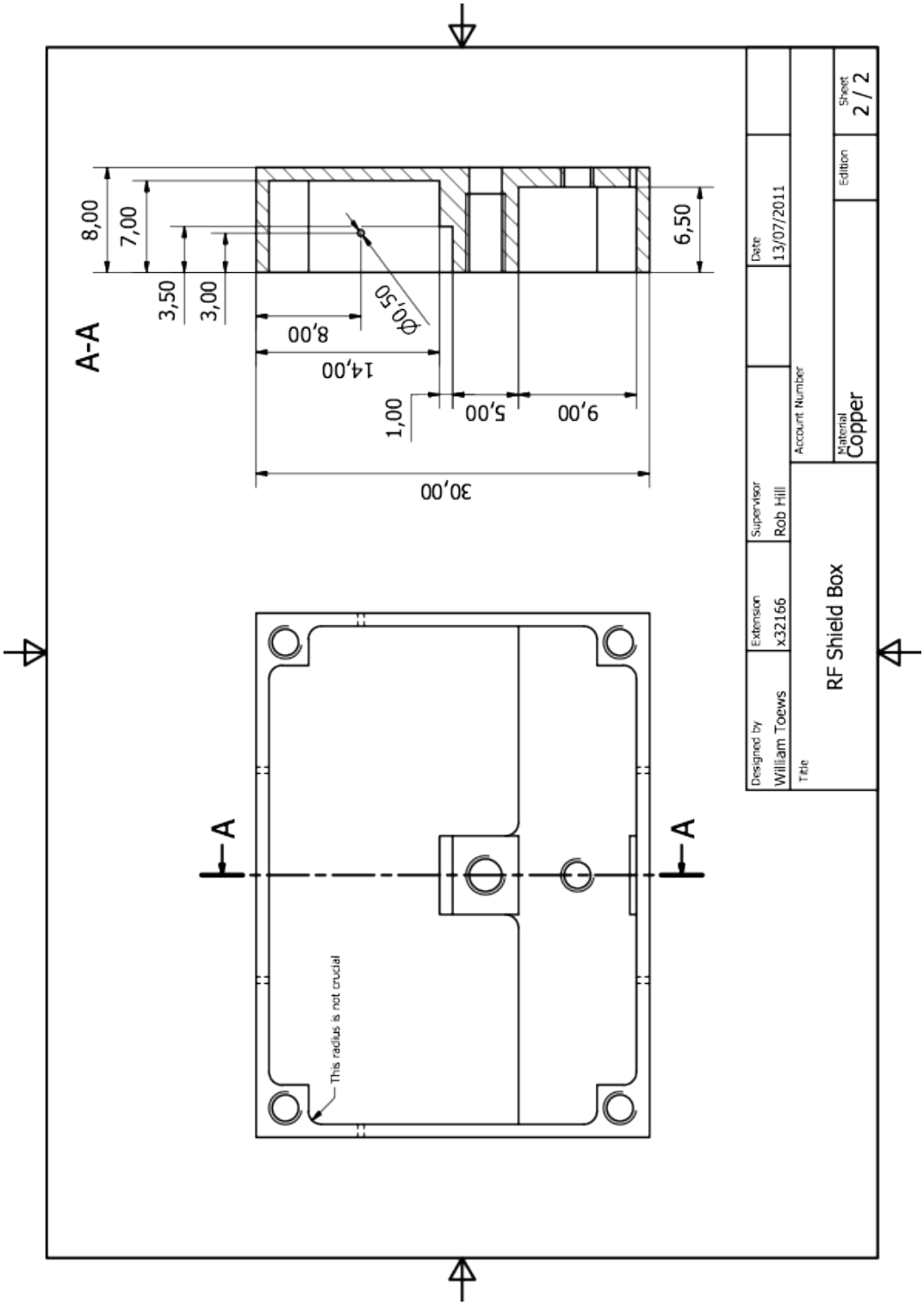
A-A
8,00
7,00
3,50
3,00
6,50
Ø0,50
8,00
14,00
1,00
5,00
9,00
30,00
A
A
This radius is not crucial
Designed by
William Toews
Extension
x32166
Supervisor
Rob Hill
Date
13/07/2011
Edition
Sheet
2 / 2
Account Number
Material
Copper
Title
RF Shield Box

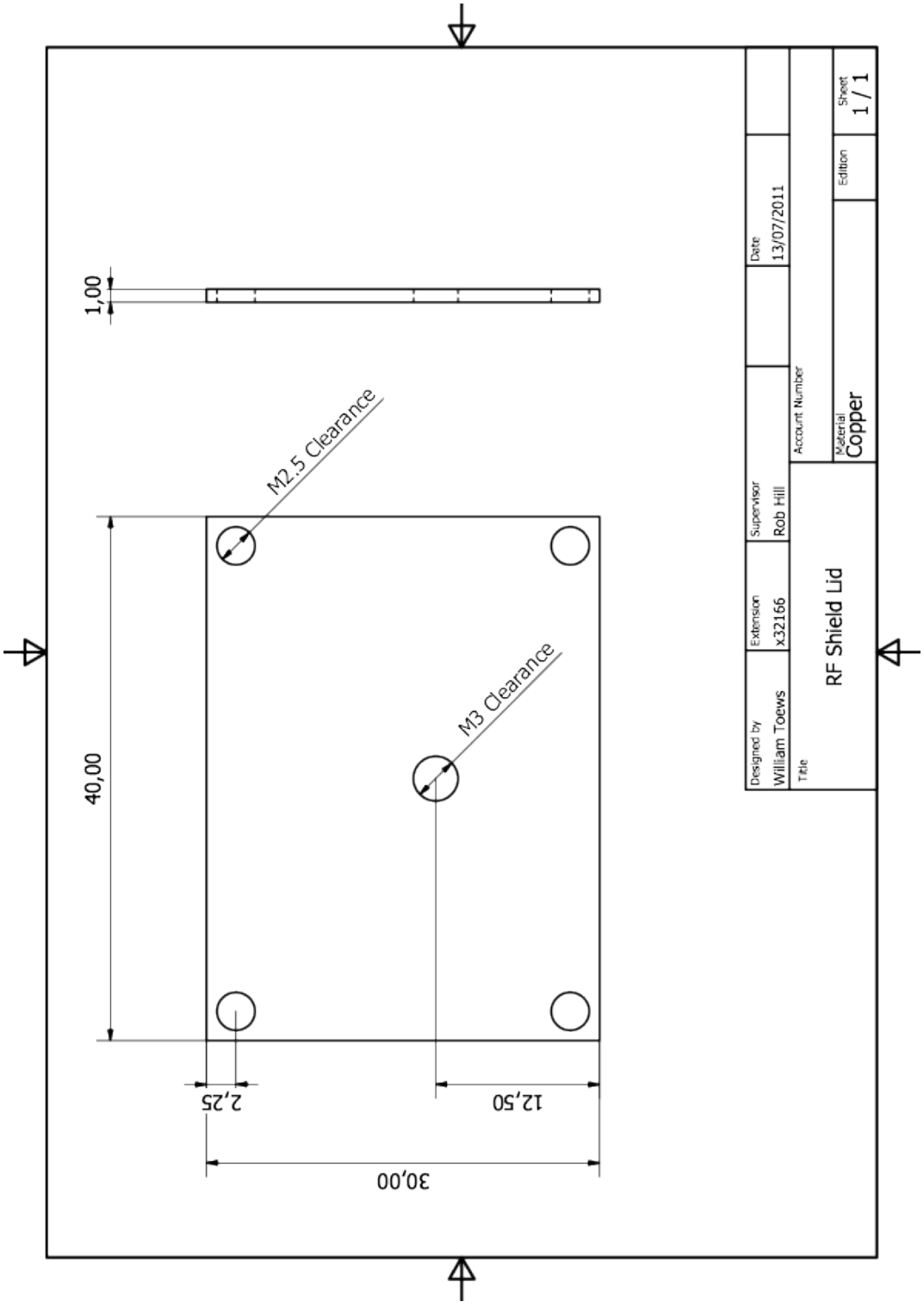
1,00
M2.5 Clearance
M3 Clearance
40,00
2,25
12,50
30,00
Designed by
William Toews
Extension
x32166
Supervisor
Rob Hill
Account Number
Material
Copper
Date
13/07/2011
Edition
Sheet
1 / 1
Title
RF Shield Lid

Appendix C

Thermal Conductivity LabView Program

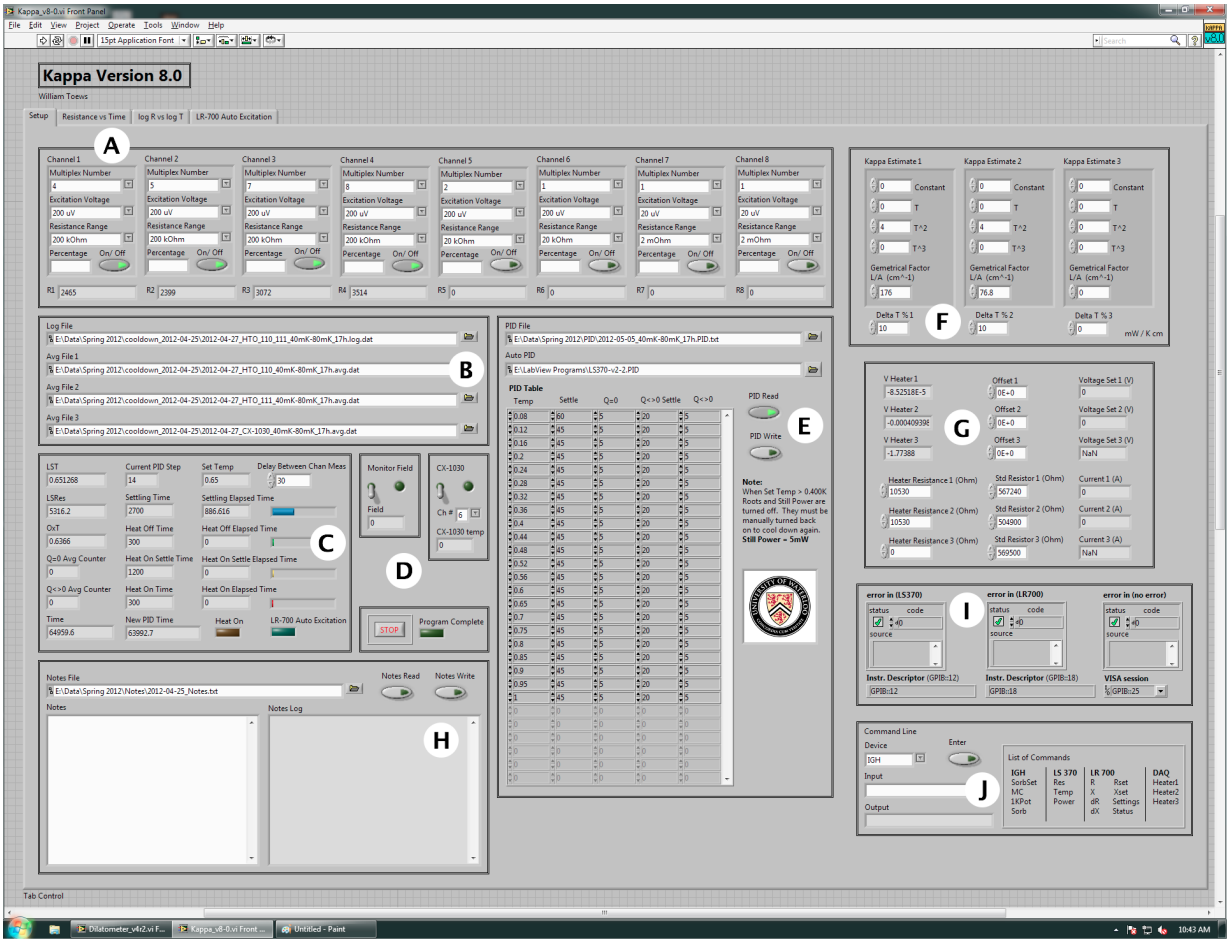
Kappa Version 8.0
William Toews
Setup
Resistance vs Time
log R vs log T
LR-700 Auto Excitation
A
B
C
D
E
F
G
H
I
J
Tab Control

A - Chose which signal from the multiplexer is assigned to each channel. Also sets the resistance range and excitation voltage for each channel. You can choose which channels to measure by turning them on using the toggle switch.

B - File save locations for log and averaged data.

C - Set the wait time between measurements for a channel change. Also monitor many items: the time remaining in each step, the total time, the set temperature, the current LakeShore and Oxford temperatures, the average counter and if the heat is on.

D - Toggles for whether you want to monitor the magnetic field strength, or the temperature on the mixing chamber from a calibrated Cernox thermometer. Also indicates if the program has completed all temperature steps.

E - Read (write) temperature step times from (to) a specified external file. Manual entry is also possible. The PID values for each temperature range is hidden but accessible in the other loaded text file. Current PID values have been found for temperatures between 40 mK and $\sim$ 1.5 K.

F - Enter the approximate value of the thermal conductivity by setting the coefficients of a third order polynomial. Also indicate the geometric factor of the sample in units of cm^{-1} (length/area). Finally enter the desired temperature gradient across the sample as a percentage of the fridge temperature (usually $\sim$10%).

G - Input the values of the standard resistors which are used to convert a voltage from the DAQ to a current. Also input the values of the heater resistors for each sample. There is also an option to indicate if the DAQ has a small voltage output offset.

H - This gives you the option to write notes about the current experiment. It logs a time stamp which may come in handy when troubleshooting log files.

I - GPIB address of the VISA sessions for the LS370, LR700 and the IPS120.

J - A small command line which can query any of the instruments. Useful when troubleshooting the system.

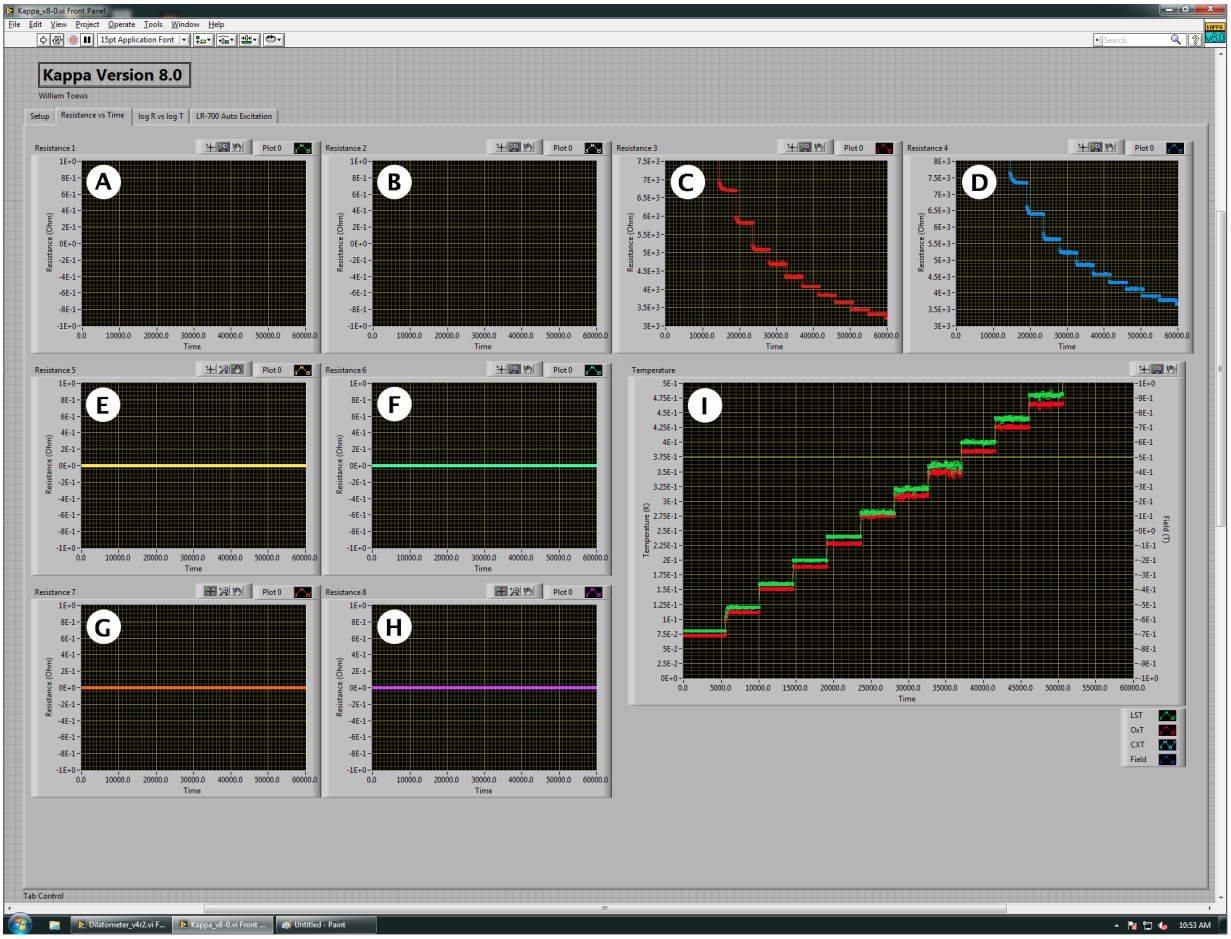

A - H - Resistance versus time plots for each of the 8 channels.

I - Multi-plot containing: LakeShore temperature versus time, Oxford temperature versus time, Cernox temperature versus time all on the left y-axis and the magnetic field versus time on the right y-axis.

References

[1] M. Sutherland, J. Dunn, W. H. Toews, E. O'Farrell, J. Analytis, I. Fisher, and R. W. Hill, Phys. Rev. B **85**, 014517 (2012).

[2] J. R. Gavaler, IEEE Transactions on Magnetics **MAG-11**, 192 (1975).

[3] M. K. Wu, J. R. Ashburn, C. J. Torng, P. H. Hor, R. L. Meng, L. Gao, Z. J. Huang, Y. Q. Wang, and C. W. Chu, Phys. Rev. Lett. **58**, 908 (1987).

[4] L. Boeri, O. V. Dolgov, and A. A. Golubov, Phys. Rev. Lett. **026403** (2008).

[5] N. W. Ashcroft and N. D. Mermin, *Solid State Physics* (Brooks Cole, 1976).

[6] C. Kittel, *Solid State Physics - 8th ed.* (Wiley, 2004).

[7] S. Y. Li, J.-B. Bonnemaison, A. Payeur, P. Fournier, C. . H. Wang, X. H. Chen, and L. Taillefer, Phys. Rev. B **77**, 134501 (2008).

[8] X. F. Sun and Y. Ando, Phys. Rev. B **79**, 176501 (2009).

[9] R. O. Pohl and B. Stritzer, Phys. Rev. B **25**, 6 (1982).

[10] H. Rosenberg, *Low Temperature Solid State Physics* (Oxford University Press, 1963).

[11] K. Onnes, KNAW Proceeding **11**, 168 (1908).

[12] K. Onnes, KNAW Proceeding **13 II**, 1274 (1911).

[13] K. Onnes and K. Hof, KNAW Proceeding **17**, 520 (1914).

[14] W. Meissner and H. Franz, Zeitschrift fur Physik **63**, 558 (1930).

[15] P. S. Swartz, Phys. Rev. Lett. **9**, 448 (1962).

[16] J. G. Bednorz and K. A. Müller, Z. Phys. B - Condensed Matter **64**, 189 (1986).

[17] H. Takahashi, K. Igawa, K. Arii, Y. Kamihara, M. Hirano, and H. Hosono, Nature **453**, 376 (2008).

[18] J. Bardeen, L. N. Cooper, and J. R. Schreiffer, Physical Review **108**, 1175 (1957).

[19] M. Takigawa, P. C. Hammel, R. H. Heffner, and Z. Fisk, Phys. Rev. B. Rapid **39**, 7371 (1989).

[20] S. E. Barrett, D. J. Durand, C. H. Pennington, C. P. Slichter, and T. A. Friedmann, Phys. Rev. B **41**, 6283 (1990).

[21] C. B. Satterthwaite, Physical Review **125**, 873 (1962).

[22] M. Tinkham, *Introduction to Superconductivity - 2nd ed.* (Dover Publications, 2004).

[23] Y. Sun and K. Maki, Phys. Rev. B **51**, 6059 (1995).

[24] M. J. Graf, S.-K. Yip, J. A. Sauls, and D. Rainer, Phys. Rev. B **53**, 15147 (1996).

[25] C. Kübert and P. J. Hirschfeld, Solid State Communications **105**, 459 (1998).

[26] A. C. Durst and P. A. Lee, Phys. Rev. B **62**, 2 (2000).

[27] L. Taillefer, Annu. Rev. Condens. Matter Phys. **1**, 51 (2010).

[28] H. F. Hess, R. B. Robinson, R. C. Dynes, J. J. M. Valles, and J. V. Waszczak, Phys. Rev. Lett. **62**, 214 (1989).

[29] R. W. Hill, C. Lupien, M. Sutherland, E. Boaknin, D. G. Hawthorn, C. Proust, F. Ronning, L. Taillefer, R. Liang, D. A. Bonn, and W. N. Hardy, Phys. Rev. Lett. **92**, 027001 (2004).

[30] M. Chiao, R. W. Hill, C. Lupien, B. Popic, R. Gagnon, and L. Taillefer, Phys. Rev. Lett. **82**, 2943 (1999).

[31] Y. Kamihara, T. Watanabe, M. Hirano, and H. Hosono, J. Am. Chem. Soc. **130**, 3296 (2008).

[32] J. Paglione and R. L. Greene, Nature Physics **6**, 645 (2010).

[33] D. J. Singh, Physica C **469**, 418 (2009).

[34] A. I. Coldea, J. D. Fletcher, A. Carrington, J. G. Analytis, A. F. Bangura, J.-H. Chu, A. S. Erickson, I. R. Fisher, N. E. Hussey, and R. D. McDonald, Phys. Rev. Lett. **101**, 216402 (2008).

[35] D. C. Johnson, Adv. Phys. **59**, 803 (2010).

[36] D. H. Lu, M. Yi, S.-K. Mo, A. S. Erickson, J. Analytis, J.-H. Chu, D. J. Singh, Z. Hussain, T. H. Geballe, I. R. Fisher3, and Z.-X. Shen, Nature **455**, 81 (2008).

[37] T. Kondo, A. F. Santander-Syro, O. Copie, C. Liu, M. E. Tillman, E. D. Mun, J. Schmalian, S. L. Bud'ko, M. A. Tanatar, P. C. Canfield, and A. Kaminski, Phys. Rev. Lett. **101**, 147003 (2008).

[38] H. Ding, P. Richard, K. Nakayama, K. Sugawara, T. Arakane, Y. Sekiba, A. Takayama, S. Souma, T. Sato, T. Takahashi, Z. Wang, X. Dai, Z. Fang, G. F. Chen, J. L. Luo, and N. L. Wang, Europhys. Lett. **83**, 47001 (2008).

[39] S. Graser, P. H. T. Maier, and D. Scalapino, New J. Phys. **11**, 025016 (2009).

[40] K. Hashimoto, T. Shibauchi, S. Kasahara, K. Ikada, S. Tonegawa, T. Kato, R. Okazaki, C. J. van der Beek, M. Konczykowski, H. Takeya, K. Hirata, T. Terashima, and Y. Matsuda, Phys. Rev. Lett. **102**, 207001 (2009).

[41] M. A. Tanatar, J.-P. Reid, H. Shakeripour, X. G. Luo, N. Doiron-Leyraud, N. Ni, S. L. Bud'ko, P. C. Canfield, R. Prozorov, and L. Taillefer, Phys. Rev. Lett. **104**, 067002 (2010).

[42] J. D. Fletcher, A. Serafin, L. Malone, J. G. Analytin, J.-H. Chu, A. S. Erickson, I. R. Fisher, and A. Carrington, Phys. Rev. Lett. **102**, 147001 (2009).

[43] K. Hashimoto, A. Serafin, S. Tonegawa, R. Katsumata, R. Okazaki, T. Saito, H. Fukazawa, Y. Kohori, K. Kihou, C. H. Lee, A. Iyo, H. Eisaki, H. Ikeda, Y. Matsuda, A. Carrington, and T. Shibauchi, Phys. Rev. B **81**, 220501(R) (2010).

[44] A. V. Chubukov, M. G. Vavilov, and A. B. Vorontsov, Phys. Rev. B **80**, 140515 (2009).

[45] A. F. Kemper, T. A. Maier, S. Graser, H.-P. Cheng, P. J. Hirschfeld, and D. Scalapino, New J. Phys. **12**, 073020 (2010).

[46] V. Mishra, A. Vorontsov, P. J. Hirshfeld, and I. Vekhter, Phys. Rev. B **80**, 224525 (2009).

[47] N. Terasaki, H. Mukuda, M. Yashima, Y. Kitaoka, K. Miyazawa, P. Shirage, H. Kito, H. Eisaki, and A. Iyo, J. Phys. Soc. Jpn. **78**, 013701 (2009).

[48] H.-J. Grafe, D. Paar, G. Lang, N. J. Curro, G. Behr, J. Werner, J. Hamann-Borrero, C. Hess, N. Leps, R. Klingeler, and B. Bchner, Phys. Rev. Lett. **101**, 047003 (2008).

[49] K. Matano, Z. A. Ren, X. L. Dong, L. L. Sun, Z. X. Zhao, and G. qing Zheng, Europhys. Lett. **83**, 57001 (2008).

[50] M. Yashima, H. Nishimura, H. Mukuda, Y. Kitaoka, K. Miyazawa, P. Shirage, K. Kihou, H. Kito, H. Eisaka, and A. Iyo, J. Phys. Soc. Jpn. **78**, 103702 (2009).

[51] G. H. Wannier, Physical Review **79**, 357 (1950).

[52] R. M. F. Houtappel, Physica **26**, 425 (1950).

[53] J. S. Gardner, M. J. P. Gingras, and J. E. Greedan, Physical Review **82**, 53 (2010).

[54] P. W. Anderson, Physical Review **102**, 4 (1956).

[55] J. D. Bernal and R. H. Fowler, J. Chem. Phys. **1**, 515 (1933).

[56] I. A. Ryzhkin, Journal of Experimental and Theoretical Physics **101**, 481 (2005).

[57] N. Majlis, *The Quantum Theory of Magnetism - 2nd ed.* (World Scientific Publishing Company, 2007).

[58] J. Mulak and Z. Gajek, *The Effective Crystal Field Potential* (Elsevier Science, 2000).

[59] S. T. Bramwell and M. Gingras, Science **294**, 1495 (2001).

[60] Y. M. Jana and D. Ghosh, Phys. Rev. B **61**, 9657 (2000).

[61] S. Rosenkranz, A. P. Ramirez, A. Hayashi, R. J. Cava, R. Siddharthan, and B. S. Shastry, Journal of Applied Physics **87**, 9 (2000).

[62] A. P. Ramirez, A. Hayashi, R. J. Cava, R. Siddharthan, and B. S. Shastry, Nature **399**, 333 (1999).

[63] R. Melko and M. Gingras, J. Phys. Cond. Mat. **16**, R1277 (2004).

[64] S. T. Bramwell, M. J. Harris, B. C. den Hertog, M. J. P. Gingras, J. S. Gardner, D. F. McMorrow, A. R. Wildes, A. L. Cornelius, J. D. M. Champion, R. G. Melko, and T. Fennell, Phys. Rev. Lett. **87**, 4 (2001).

[65] B. C. den Hertog and M. J. P. Gingras, Phys. Rev. Lett. **84**, 3430 (2000).

[66] R. Siddharthan, B. S. Shastry, A. P. Ramirez, A. Hayashi, R. J. Cava, and S. Rosenkranz, Phys. Rev. Lett. **83**, 1854 (1999).

[67] R. Siddharthan, B. S. Shastry, and A. P. Ramirez, Phys. Rev. B **63**, 184412 (2001).

[68] K. Matsuhira, Y. Hinatsu, K. Tenya, and T. Sakakibara, J. Phys.: Condens. Matter **12**, L649 (2000).

[69] K. Matsuhira, Y. Hinatsu, and T. Sakakibara, J. Phys.: Condens. Matter **13**, L737 (2001).

[70] J. Snyder, J. S. Slusky, R. J. Cava, and P. Schiffer, Nature **413**, 48 (2001).

[71] O. A. Petrenko, M. R. Lees, and G. Balakrishnan, Phys. Rev. B **68**, 012406 (2003).

[72] Z. Hiroi, K. Matsuhira, S. Takagi, T. Tayama, and T. Sakakibara, J. Phys. Soc. Japan **72**, 2 (2003).

[73] R. Higashinaka, H. Fukazawa, K. Deguchi, and Y. Maeno, J. Phys. Soc. Japan **73**, 10 (2004).

[74] C. P. Office, LHC to run at 4 TeV per beam in 2012, 2012, http://press.web.cern.ch/press/PressReleases/Releases2012/PR01.12E.html.

[75] C. Castelnovo, R. Moessner, and S. Sondhi, Nature **451**, 06433 (2008).

[76] L. D. C. Jaubert and P. C. W. Holdsworth, Nature Phys. **5**, 258 (2009).

[77] J. Snyder, B. G. Ueland, J. S. Slusky, H. Karunadasa, R. J. Cava, and P. Schiffer, Phys. Rev. B **69**, 064414 (2004).

[78] B. Klemke, M. Meissner, P. Strehlow, K. Kiefer, S. A. Grigera, and D. A. Tennant, J. Low Temp. Phys. **163**, 345 (2011).

[79] L. R. Yaraskavitch, H. M. Revell, S. Meng, K. A. Ross, H. M. L. Noad, H. A. Dabkowska, B. D. Gaulin, and J. B. Kycia, Phys. Rev. B **85**, 020410(R) (2012).

[80] M. Orendáč, J. Hanko, E. Čižmár, A. Orendáčová, M. Shirai, and S. T. Bramwell, Phys. Rev. B **75**, 104425 (2007).

[81] S. T. Bramwell, S. R. Giblin, S. Calder, R. Aldus, D. Prabhakaran, and T. Fennell, Nature **461**, 15 (2009).

[82] S. R. Dunsiger, A. A. Aczel, C. Arguello, H. A. Dabkowska, A. Dabkowski, M.-H. Du, T. Goko, B. Javanprast, T. Lin, F. L. Ning, H. M. L. Noad, D. J. Singh, T. J. Williams, Y. J. Uemura, M. J. P. Gingras, and G. M. Luke, Phys. Rev. Lett. **107**, 207207 (2011).

[83] F. Pobell, *Matter and Methods at Low Temperatures* (Springer, 1996).

[84] I. Mazin and J. Schmalian, Physica C **469**, 614 (2009).

[85] M. Yamashita, N. Nakata, Y. Senshu, S. Tonegawa, K. Ikada, K., H. Sugawara, T. Shibauchi, and Y. Matsuda, Phys. Rev. B **80**, 220509 (2009).

[86] A. Carrington, A. I. Coldea, J. D. Fletcher, N. E. Hussey, C. M. J. Andrew, A. F. Bangura, J. G. Analytis, J.-H. Chu, A. S. Erickson, I. R. Fisher, and R. D. McDonald, Physica C **469**, 459 (2008).

[87] M. F. Smith, J. Paglione, M. B. Walker, and L. Taillefer, Phys. Rev. B **71**, 014506 (2005).

[88] R. W. Hill, S. Li, M. B. Maple, and L. Taillefer, Phys. Rev. Lett. **101**, 237005 (2008).

[89] Y. Kohama, Y. Kamihara, H. Kawaji, T. Atake, M. Hirano, and H. Hosono, J. Phys. Soc. Jap. **77**, 094715 (2008).

[90] Y. Bang, Phys. Rev. Lett. **104**, 217001 (2010).

[91] J.-P. Reid, A. Juneau-Fecteau, R. T. Gordon, S. R. de Cotret, N. Doiron-Leyraud, X. G. Luo, H. Shakeripour, J. Chang, M. A. Tanatar, H. Kim, R. Prozorov, T. Saito, H. Fukazawa, Y. Kohori, K. Kihou, C. H. Lee, A. Iyo, H. Eisaki, B. Shen, H.-H. Wen, and L. Taillefer, Supercond. Sci. Technol. **25**, 084013 (2012).

[92] V. Mishra, G. Boyd, S. G. T. Maier, P. J. Hirschfeld, and D. j. Scalapino, Phys. Rev. B **79**, 094512 (2009).

[93] T. M. McQueen, M. Regulacio, A. J. Williams, Q. Huang, J. W. Lynn, Y. S. Hor, D. V. West, M. A. Green, and R. J. Cava, Phys. Rev. B **78**, 024521 (2008).

[94] M. A. Tanatar, J.-P. Reid, S. R. de Cotret, N. Doiron-Leyraud, F. Laliberté, E. Hassinger, J. Chang, H. Kim, K. Cho, Y. J. Song, Y. S. Kwon, R. Prozorov, and L. Taillefer, Phys. Rev. B **84**, 054507 (2011).

[95] X. G. Luo, M. A. Tanatar, J.-P. Reid, H. Shakeripour, N. Doiron-Leyraud, N. Ni, S. L. Bud'ko, P. C. Canfield, H. Luo, Z. Wang, H.-H. Wen, R. Prozorov, and L. Taillefer, Phys. Rev. B **80**, 140503(R) (2009).

[96] J. G. Analytis, J.-H. Chu, A. S. Erickson, C. Kucharczyk, A. Serfin, A. Carrington, C. Cox, S. M. Kauzlarich, H. Hope, and I. R. Fisher, arXiv:0810.5368 .

[97] P. J. Hirschfeld, W. O. Putikka, and D. J. Scalapino, Phys. Rev. Lett. **71**, 3705 (1993).

[98] U. Welp, W. K. Kwok, G. W. Crabtree, K. G. Vandervoort, and J. Z. Liu, Phys. Rev. Lett. **62**, 16 (1989).

[99] R. Higashinaka, H. Fukazawa, and Y. Maeno, Phys. Rev. Lett. **68**, 014415 (2003).

[100] R. Higashinaka, H. Fukazawa, K. Deguchi, and Y. Maeno, J. Phys. Cond. Mat. **16**, S679 (2004).

[101] S. R. Giblin, S. T. Bramwell, P. C. Holdsworth, D. Prabhakaran, and I. Terry, Nature Physics **7**, 252 (2011).

[102] G. Kolland, O. Breunig, M. Valldor, M. Hiertz, J. Frielingsdorf, and T. Lorenz, arXiv:1205.5700v1 (2012).

[103] J. P. Clancy, J. P. C. Ruff, S. R. Dunsiger, Y. Zhao, H. A. Dabowska, J. S. Gardner, Y. Qiu, J. R. D. Copley, T. Jenkins, and B. D. Gaulin, Phys. Rev. B **79**, 014408 (2009).

[104] C. Krey, S. Legl, S. R. Dunsiger, M. Meven, J. S. Gardner, J. M. Roper, and C. Pfleiderer, Phys. Rev. Lett. **108**, 257204 (2012).

[105] Z. Y. Zhou, X. M. Wang, C. Fan, W. Tao, X. G. Liu, W. P. Ke, F. B. Zhang, X. Zhao, and X. F. Sun, Phys. Rev. B **83**, 014414 (2011).

[106] O. A. Petrenko, M. R. Lees, and G. Balakrishnan, J. Phys. Cond. Mat. **23**, 164218 (2011).

[107] Y. Nakanishi, T. Kumagai, M. Yoshizawa, K. Matsuhira, S. Tagaki, and Z. Hiroi, Phys. Rev. B **83**, 184434 (2011).

[108] P. Klemens, *Solid State Physics Volume 7* (Academic Press Inc., 1958).

[109] P. D. Thacher, Physical Review **156**, 3 (1967).

[110] K. A. Ross, T. Proffen, H. A. Dabkowska, J. A. Quilliam, L. R. Yaraskavitch, J. B. Kycia, and B. D. Gaulin, arXiv:1208.2281v1 (2012).

[111] Y. Kohama, A. V. Sologubenko, N. R. Dilley, V. S. Zapf, M. Jaime, J. A. Mydosh, A. Paduan-Filho, K. A. Al-Hassanieh, P. Sengupta, S. Gangadharaiah, A. L. Chernyshev, and C. D. Batista, Phys. Rev. Lett. **106**, 037203 (2011).

[112] C. Castelnovo, R. Moessner, and S. L. Sondhi, Phys. Rev. B **84**, 144435 (2011).

[113] N. D. Mathur, F. M. Grosche, S. R. Julian, I. R. Walker, D. M. Freye, R. K. W. Haselwimmer, and G. G. Lonzarich, Nature **394**, 39 (1998).

[114] R. A. Borzi, S. A. Grigera, J. Farrell, R. S. Perry, S. J. S. Lister, S. L. Lee, D. A. Tennant, Y. Maeno, and A. P. Mackenzie, Science **315**, 214 (2007).

[115] H. Vonlohneysen, T. Pietrus, G. Portisch, H. G. Schlager, A. Schroder, M. Sieck, and T. Trappmann, Physical Review Letters **72**, 3262 (1994).

[116] T. Moriya and A. Kawabata, Journal of the Physical Society of Japan **34**, 639 (1973).

[117] J. A. Hertz, Phys. Rev. B **14**, 1165 (1976).

[118] A. J. Millis, Phys. Rev. B **48**, 7183 (1993).

[119] T. Moriya and A. Kawabata, Journal of the Physical Society of Japan **35**, 669 (1973).

[120] P. Gegenwart, Q. Si, and F. Steglich, Nature Physics **4**, 186 (2008).

[121] Q. M. Si, S. Rabello, K. Ingersent, and J. L. Smith, Nature **413**, 804 (2001).

[122] P. Sun and G. Kotliar, Phys. Rev. Lett. **91**, 037209 (2003).

[123] C. Pépin, Phys. Rev. Lett. **98**, 206401 (2007).

[124] I. Paul, C. Pépin, and M. Normal, Phys. Rev. Lett. **98**, 026402 (2007).

[125] K.-S. Kim and C. Pépin, Phys. Rev. Lett. **102**, 156404 (2009).

[126] S. Nakatsuji, K. Kuga, Y. Machida, T. Tayama, T. Sakakibara, Y. Karaki, H. Ishimoto, S. Yonezawa, Y. Maeno, E. Pearson, G. G. Lonzarich, L. Balicas, H. Lee, and Z. Fisk, Nature Physics **4**, 603 (2008).

[127] Y. Matsumoto, S. Nakatsuji, K. Kuga, Y. Karaki, N. Horie, Y. Shimura, T. Sakakibara, A. H. Nevidomskyy, and P. Coleman, Science **331**, 316 (2011).

[128] M. Okawa, M. Matsunami, K. Ishizaka, R. Eguchi, M. Taguchi, A. Chainani, Y. Takata, M. Yabashi, K. Tamasaku, Y. Nishino, T. Ishikawa, K. Kuga, N. Horie, S. Nakatsuji, and S. Shin, Phys. Rev. Lett. **104**, 4 (2010).

[129] R. T. Macaluso, S. Nakatsuji, K. Kuga, E. L. Thomas, Y. Machida, Y. Maeno, Z. Fisk, and J. Y. Chan, Chemistry of Materials **19**, 1918 (2007).

[130] H. Pfau, S. Hartmann, U. Stockert, P. Sun, S. Lausberg, M. Brando, S. Friedemann, C. Krellner, C. Geibel, S. Wirth, S. Kirchner, E. Abrahams, Q. Si, and F. Steglich, Nature **484**, 493 (2012).

[131] M. Tanatar, J. Paglione, C. Petrovic, and L. Taillefer, Science **316**, 1320 (2007).

[132] J. Paglione, M. A. Tanatar, D. G. Hawthorn, R. Hill, F. Ronning, M. Sutherland, L. Taillefer, C. Petrovic, and P. C. Canfield, Phys. Rev. Lett. **94**, 216602 (2005).

[133] R. P. Smith, M. Sutherland, G. G. Lonzarich, S. S. Saxena, N. Kimura, S. Takashima, M. Nohara, and H. Takagi, Nature **455**, 1220 (2008).

[134] A. Hackl and R. Thomale, Phys. Rev. B **83**, 235107 (2011).

[135] T. Senthil, S. Sachdev, and M. Vojta, Phys. Rev. Lett. **90**, 216403 (2003).

[136] T. Senthil, M. Vojta, and S. Sachdev, Phys. Rev. B **69**, 035111 (2004).

[137] M. Sutherland, R. Smith, N. Marcano, Y. Zou, F. M. Grosche, N. Kimura, S. M. Hayden, S. Takashima, M. Nohara, and H. Takagi, Phys. Rev. B **85**, 035118 (2012).

[138] M. Smith and R. McKenzie, Phys. Rev. Lett. **101**, 266403 (2008).

[139] J. M. Ziman, *Electrons and Phonons: The Theory of Transport Phenomena in Solids* (Oxford University Press, 1963).

[140] J. Paglione, M. A. Tanatar, D. G. Hawthorn, F. Ronning, R. Hill, M. Sutherland, L. Taillefer, and C. Petrovic, Phys. Rev. Lett. **97**, 106606 (2006).